TU Delft

Delft University of Technology

In situ TEM electrical measurements of semiconductor and metal nanowires

Neklyudova, Mariya

DOI
10.4233/uuid:b3696080-152a-4f00-9be7-4eb139c05ab4

Publication date
2016

Document Version
Final published version

Citation (APA)
Neklyudova, M. (2016). In situ TEM electrical measurements of semiconductor and metal nanowires DOI: 10.4233/uuid:b3696080-152a-4f00-9be7-4eb139c05ab4

Important note
To cite this publication, please use the final published version (if applicable).
Please check the document version above.

Copyright
Other than for strictly personal use, it is not permitted to download, forward or distribute the text or part of it, without the consent of the author(s) and/or copyright holder(s), unless the work is under an open content license such as Creative Commons.

Takedown policy
Please contact us and provide details if you believe this document breaches copyrights.
We will remove access to the work immediately and investigate your claim.

This work is downloaded from Delft University of Technology.
For technical reasons the number of authors shown on this cover page is limited to a maximum of 10.

In situ TEM electrical measurements of semiconductor and metal nanowires

Proefschrift

ter verkrijging van de graad van doctor
aan de Technische Universiteit Delft,
op gezag van de Rector Magnificus prof.ir. K.C.A.M. Luyben,
voorzitter van het College voor Promoties,
in het openbaar te verdedigen op
dinsdag 05 Juli 2016 om 15:00 uur

Door

Mariya NEKLYUDOVA
Mater of Science in Physics,
Novosibirsk State University, Rusland
geboren te Petropavlovsk-Kamchatsky, Sovjet-Unie

Dit proefschrift is goedgekeurd door de promotor(en):

Prof. dr. H.W. Zandbergen

Samenstelling promotiecommissie:

Rector Magnificus	voorzitter
Prof. dr. H.W. Zandbergen	Technische Universiteit Delft, promotor
Prof. dr. J.M. van Ruitenbeek	Universiteit Leiden
Independent members:	
Prof. dr. A. Kirkland	University of Oxford
Prof. M. Loncar	Harvard University
Prof. dr. B.J. Thijsse	Technische Universiteit Delft
Prof. dr. ir. H.S.J. van der Zant	Technische Universiteit Delft
Dr. ir. F.D. Tichelaar	Technische Universiteit Delft
Prof. dr. ir. J. Ruud van Ommen	Technische Universiteit Delft

Keywords: *In situ* Transmission electron microscopy, nanowires, electromigration

Copyright © 2016 by Mariya Neklyudova
Author e-mail: mariya.a.neklyudova@gmail.com

ISBN 978-90-8593-256-7
Casimir PhD series, Delft-Leiden 2016-14

Printed by Gildeprint

An electronic version of this dissertation is available at
http://reposiory.tudelft.nl/

Посвящается

моей маме

Contents

Chapter 1 Introduction to electrical failures at the nanoscale.....1

1.1. Introduction.....2
1.2. Electromigration.....4
1.2.1. Fundamentals of electromigration.....4
1.2.2. Electromigration-induced mechanical stress.....7
1.2.3. Current-induced Joule heating in a nanowire.....8
1.2.4. Median time to failure and accelerated electromigration experiments.....9
References.....10

Thesis Outline.....15

Chapter 2 Experimental techniques.....17

2.1. Experimental methods.....18
2.1.1. Transmission Electron Microscopy (TEM).....18
- Brief historical overview.....18
- Basics of transmission electron microscopy.....19
- Diffraction and Image formation in TEM.....20

2.1.2. Scanning Transmission Electron Microscopy (STEM).....27
2.1.3. Elemental Analysis: Energy Dispersive X-ray Spectroscopy.....28
2.2. Sample fabrication.....30
2.3. Measurement setup.....35
2.3.1. *In situ* TEM.....35
2.3.2. Holders for *in situ* TEM measurements.....36
- Electrical measurements.....36
- Heating experiments.....36

2.3.3. Setup for electrical measurements.....37
References.....38

Chapter 3 Back side lithography technique for transmission electron microscopy research.....43

3.1. Introduction....44
3.2. Experimental....46
3.3. Applications....47
3.4. Discussions and conclusions....51
References....52

Chapter 4 *In situ* electrical characterization of tapered InAs nanowires in a transmission electron microscope with ohmic contacts....55

4.1. Introduction....56
4.2. Method....56
4.3. Results....58
4.4. Discussion....67
4.5. Conclusions....69
References....69
Supplementary material....72

Chapter 5 *In situ* TEM investigations of controlled electrical breakdowns in InAs nanowires....75

5.1. Introduction....76
5.2. Experimental....78
5.3. Results and discussions....82
5.3.1. TEM visualization of electrical breakdown....82
5.3.2. STEM visualization of electrical breakdown....86
5.3.3. *In situ* TEM holography visualization of an electrical breakdown....91
5.4. Conclusions....99
References....100

Chapter 6 *In situ* TEM visualization of electromigration-induced nanogap formation in AuPd nanowires....103

6.1. Introduction....104
6.2. Experimental....105
6.3. Results and Discussions....107
6.4. Conclusions....118

References.....118

Chapter 7 *In situ* TEM formation of a single-crystalline bismuth film on an amorphous substrate.....121

7.1. Introduction.....122
7.2. Experimental.....123
7.3. Results.....124
7.3.1. *Experiment 1*. Modification of a polycrystalline to a monocrystalline Bi film by *in situ* TEM heating with a focused electron beam.....124
7.3.2. *Experiment 2*. Modification of small areas (60-200 nm in diameter) of a polycrystalline to a monocrystalline Bi film by *in situ* TEM heating and electron beam heating.....128
7.3.3. *Experiment 3*. Diffraction pattern changes during *in situ* heating and electron-beam bombardment.....131
7.3.4. *Experiment 4*. Dependence on film orientation with respect to the electron beam.....133
7.3.5. *Experiment 5*. "Shape memory" effect.....134
- Bismuth film.....134
- Bismuth film covered with Al2O3.....137

7.3.6. *Experiment 6*. Bismuth oxide reduction treatment.....139
7.4. Discussions.....140
7.5. Conclusions.....144
References.....144

Summary.....151

Samenvatting.....152

Curriculum Vitae.....153

Publications.....155

Acknowledgements.....157

CHAPTER 1

Introduction to electrical failures at the nanoscale

In this Chapter a brief introduction is given to the phenomenon of electromigration. Special attention is paid to electromigration in thin conductors, i.e. nanowires that are used in modern-day integrated circuit industry. A description of main physical principles and causes of electromigration is given.

1.1. Introduction

In advanced semiconductor electronic industry a modern chip contains a dense array of thin metallic wires that provide with the current transport between the different components of the chip [1]. These metallic wires are called interconnects. Due to continuous requirement of miniaturization for higher performance of modern integrated circuits, the density of on-chip interconnects increases and it requires a decrease in both interconnect width and thickness. However, when interconnects are reduced to nanoscale dimensions, the significant problem for the process and development of various nanoelectronic devices is the thinning down or failure of interconnects due to high current stress conditions and joule heating [2-4]. The underlying physical phenomenon is a gradual displacement of atoms, that eventually leads to thinning down or breakdown of conducting line due to applied electric field, which is called electromigration [5-7]. Electromigration leads to failures in nanoelectronic devices by inducing voids or hillocks, which are formed by the depletion and accumulation of metal atoms, respectively. A typical example of voids and

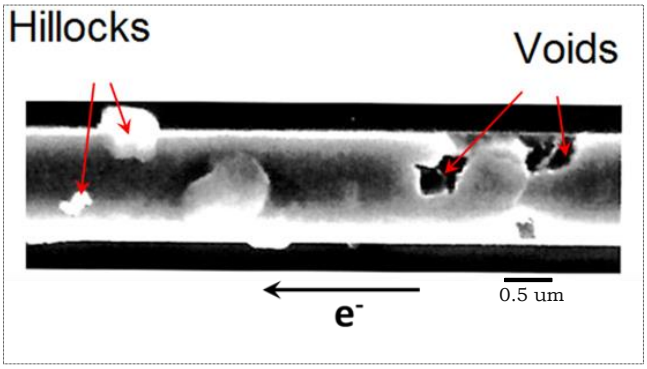

Figure 1.1. SEM image of electromigration features in Al interconnect line section [8].

hillock formation in integrated circuit is presented in figure 1.1 [8]. The formation of voids in metallic line results in significant resistance increase leading to circuit parametric failure or open circuits. The hillock formation in interconnects can cause short circuits between adjacent interconnects depending on geometry and proximity of metal lines to each other. If the

operating temperature of integrated circuit is increased, the electromigration-induced mass transport in interconnects will be accelerated.

In contrast to destructive influence of electromigration on nanoelectronics due to causing of irreversible changes in wire's geometry and microstructure which subsequently result in breakdown, it can be applied for controlled nanoscale modification of the wires. In a research field of nanofabrication, electromigration is utilized to produce nanogap electrodes – a pair of metallic electrodes with several nanometers (1-10nm) of separation [9-13]. A typical image of electromigrated nanogaps is shown in figure 1.2 [14]. Such nanogap devices are widely used in single molecule electronics for characterization of electronic properties of individual nanoparticles or single molecules.

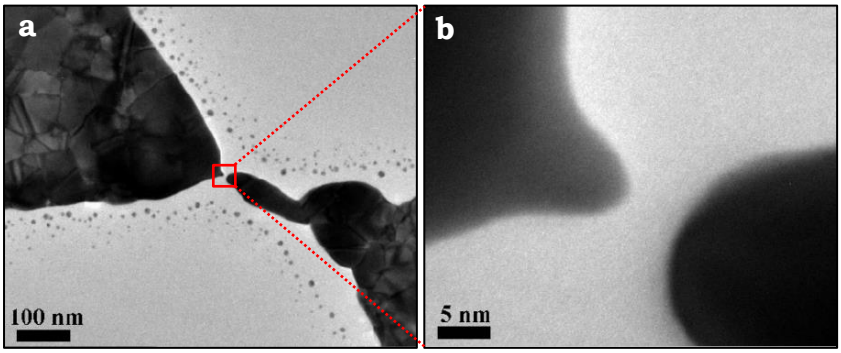

Figure 1.2. TEM images of a typical electromigrated nanogap in Au on SiN membranes, obtained at lower (a) and higher magnification (b) [14].

Many parameters should be taken into account to characterize and explain the mechanisms of electrical failures under an applied electric field: the material of the wire, wire dimensions, microstructure, temperature and stress distribution. The variation of these parameters over the wire can result in a non-uniform distribution of atomic flow and, consequently, it can lead to degradation of the wire. Thus, in order to understand the mechanisms of electrical breakdowns in various types of nanowires and correlate it with the structural properties of material, methods of precise observation and characterization of electrical transport properties of ten-nanometre-scale wires are required. Hence, the possibility to perform *in-situ*

electrical measurements combined with microscopy imaging techniques is of benefit for further development of micro-, nano- and molecular electronics.

In this thesis the main focus is on *in situ* study of electromigration-assisted breakdowns in various types of nanowires; therefore, a brief overview of fundamentals of this phenomenon is given below.

1.2. Electromigration

Originally, the first report on electromigration phenomenon was introduced over 100 years ago by a French scientist named Gerardin, who observed electromigration in molten alloys of lead-tin and mercury-sodium [15]. However, the interest to this phenomenon increased only in 1960s when electromigration was first identified as a reliability problem in integrated circuits. In 1961, Huntington *et al* reported on current-induced motion of surface scratches on bulk material [16, 17]. They concluded that the transport of thermally activated metal ions is governed by two opposing forces called "electron wind" force and direct force. The first observation of electromigration in thin films was made by Blech [18]. One of the most important engineering studies was undertaken by Jim Black at Motorola in 1969 [19]. Investigations in this field were pioneered by a number of researchers throughout the semiconductor industry [20, 23]. At that time, the metal interconnects in integrates circuits were still about 10 micrometres wide. Currently, the interconnects are tens of nanometers in width, which makes studies of electromigration incredibly important.

1.2.1. Fundamentals of electromigration

Electromigration is a process of material transport caused by the gradual displacement of ions in a conducting wire under the influence of an electric field.

The net electromigration force (F_{net}) exerted on a single metal ion consists of two opposing contributions: a direct force (F_{direct}) and a wind

force (F_{wind}). The direct force is an electrostatic force on a metal ion core under the influence of applied electric field. The direction and magnitude of this force is dependent on the charge of the ion core. The electron wind force is corresponded to the force on the ions due to electron scattering is in the direction of the electron flow. Thus, the total electromigration force (F_{direct}) can be written as [23-26]:

$$F_{net} = F_{direct} + F_{wind} = (Z_{direct} + Z_{wind})eE = Z^*eE \tag{1.1}$$

where Z_{wind} is the valence number which arises from the electron wind force, Z_{direct} is the nominal valence of an ion, $Z^* = Z_{direct} + Z_{wind}$ is called effective valence (or effective charge), e is elementary charge and E is the applied electric field. If the electron wind force prevails over the direct force, the effective charge is negative, which implies that atoms move in the direction of electron flow (figure 1.3). The rate at which atoms migrate depends on the local diffusion coefficient and is given by the Nernst-Einstein equation [26]:

$$v = \frac{DF_{net}}{k_BT} = \frac{DZ^*eE}{k_BT}, \tag{1.2}$$

where $D = D_0 \exp\left(\frac{-E_a}{k_BT}\right)$ is the atomic diffusion coefficient, D_0 is diffusion constant, E_a is the activation energy for diffusion, k_B is the Boltzmann's constant and T is the temperature.

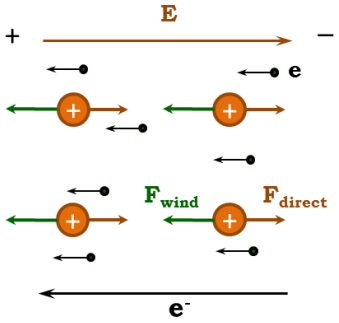

Figure 1.3. A schematic illustration of the electron wind and direct forces acting on atoms during electromigration.

The atomic flux due to electromigration is expressed by:

$$J = vn = \frac{DF_{net}}{k_B T} n = \frac{DZ^* eE}{k_B T} n = \frac{DZ^* e\rho j}{k_B T} n \,, \tag{1.3}$$

where n is the atomic concentration, ρ is the resistivity, j is the current density. Electromigration is an activated diffusion process, so the rate and the flux of electromigration increases with increasing temperature. From (1.2) and (1.3) one can see that the sign of the effective valence determines the direction of atomic migration. Also, the atomic flux is directly proportional to the current density, resistivity and to the atomic diffusion coefficient. It means that the electromigration-induced material transport is a function of the atomic diffusivity paths (see figure 1.4).

Mass transport in metal lines due to an applied electric field can occur through several possible diffusion paths (lattice diffusion, grain boundary diffusion, surface diffusion, pipe diffusion), so the total material transport is determined by the sum of the mass transport taking place along each of these paths [27, 28]. Typically, the material transport through these paths is considered by setting an effective diffusion coefficient. The effective diffusion coefficient is determined by the dominant diffusion mechanism (by the fastest diffusion path). The dominant diffusion mechanism depends on several factors, like the temperature, the microstructure and the quality of the interface between the metal and adjacent layers. Thus, lattice diffusion has the highest activation energy, being the slowest path for mass transport, while the activation energy for diffusion along grain boundaries and interfaces is lower. In general, surfaces have the lowest activation energy values, being the fastest

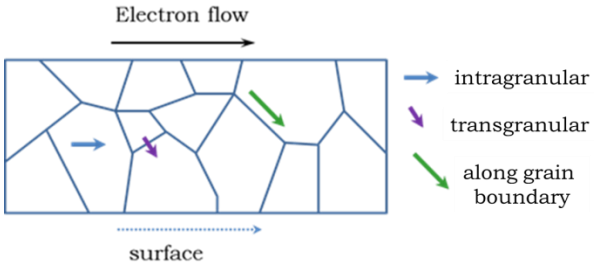

Figure 1.4. A schematic illustration of different diffusion paths for atoms moving during electromigration. The length of the arrows which indicate the possible diffusion paths shows the relative diffusion rate in each case.

diffusivity paths. As an example, in table 1.1. the typical temperature-dependent values for diffusivity through different paths are shown for Cu and Al [29].

Material	Diffusivities at 100°C (cm^2/s)	Diffusivities at 350°C (cm^2/s)
Cu	$D_{Lattice} = 7 \cdot 10^{-28}$ $D_{Grain\ boundary} = 3 \cdot 10^{-15}$ $D_{Surface} = 3 \cdot 10^{-12}$	$D_{Lattice} = 5 \cdot 10^{-17}$ $D_{Grain\ boundary} = 1.2 \cdot 10^{-9}$ $D_{Surface} = 10^{-8}$
Al	$D_{Lattice} = 1.5 \cdot 10^{-19}$ $D_{Grain\ boundary} = 6 \cdot 10^{-11}$	$D_{Lattice} = 10^{-11}$ $D_{Grain\ boundary} = 5 \cdot 10^{-7}$

Table 1.1. Diffusivity values for different diffusion paths in Cu and Al at 100 and 350°C [29].

1.2.2. Electromigration-induced mechanical stress

The depletion and accumulation of material at the sites of non-zero atomic flux divergence lead to a mechanical stress gradient in the metal wires. At the sites where material accumulates the stress is compressive, while at the sites of material depletion the stress is tensile. The atomic flux due to the stress gradient is opposite in direction to the electromigration atomic flux, counteracting the electromigration mass transport. This flux is therefore often referred to as an atomic backflow. It should be mentioned that the mechanical stress can also have components unrelated to electromigration atomic flux, such as difference in the thermal expansion rates of materials [30-33].

Under certain conditions, the atomic flux due to the mechanical stress can fully compensate the atomic flux due to electromigration, preventing further breakage. The net atomic flux J_{net} due to electromigration and mechanical stress can be expressed as:

$$J_{net} = n\frac{D}{k_B T}\left(\Omega\frac{\partial\sigma}{\partial x} - Z^* e\rho j\right), \tag{1.4}$$

where σ is the mechanical stress, Ω is the atomic volume, and x is the distance along the wire. The steady state condition or "Blech Condition" is established when the net atomic flux becomes zero:

$$\Omega \frac{\partial \sigma}{\partial x} = Z^* e \rho j. \quad (1.5)$$

From equation (1.5) one can see that when the atomic backflow flux equals to the flux due to electromigration, the stress varies linearly along the line. Thus, if $\sigma_{threshold}$ is the maximum stress that the metallic line can withstand, a critical product ("Blech Product") for electromigration failure can be written as:

$$(jL)_{threshold} = \frac{\Omega(\sigma_{threshold} - \sigma_0)}{Z^* e \rho}, \quad (1.6)$$

where L is the wire length. If this product is less than a certain critical value electromigration will not be observed [34]. Thus, from equation (1.6) we see that for a given current density, a critical length of the wire ("Blech Length") can be derived, so that if the wire is shorter than this "Blech length", electromigration cannot be considered as a failure mechanism.

1.2.3. Current-induced Joule heating in a nanowire

When an electrical current passes through a conductor, the interaction of the electrons with lattice produces a thermal energy equal to the product of the square of the current and the resistance ($Q = j^2 \rho$, where j is the current density, ρ is the resistivity). This is called Joule heating. If the current is low, the heat is effectively conducted away, but there must be some temperature increase even if it is not detectable. If the current density approaches 10^6A/cm^2, Joule heating can produce enough energy to make the nanowires heat up considerably.

The rate of the nanowire failure due to electromigration depends on the temperature. The temperature, in turn, depends on the balance between net energy input from current flowing through the wire and the energy loss rate to surroundings. For our samples we can consider a model with a nanowire connected to two electrodes representing heatsinks. The temperature distribution can be obtained by solving Poisson's equation [35]:

$$k \frac{d^2 T}{dx^2} - \beta T + j^2 \rho = 0, \quad (1.7)$$

where the first term in this equation is Fourier heat conduction due to the temperature gradient, k is the thermal conductivity of a wire, the second term represent the heat conduction between the nanowire and the substrate, where $\beta = \frac{k_s}{t_w t_s}$, k_s is the thermal conductivity of the substrate, t_w and t_s are the thickness of the wire and the substrate, respectively, the last term is the Joule heat. It should be mentioned that in this simple model of heat dissipation in a nanowire we made several assumptions: the heat flow is one-dimensional and along the "x" axis; the dimensions of contacts are much larger than of the nanowire, which means that the current density in the contacts is several orders of magnitude smaller in comparison with the nanowire, so the heat generation term within the contacts is neglected; there are no localised points of higher resistance within the wire than the surroundings; the resistance of the wire does not change with the temperature; the current density is described by a step function. From equation (1.7) it can be concluded that: the temperature profile has a maximum at the centre of the nanowire. Since the hotter parts of the nanowire experience greater thermomechanical compressive stress, the thermal stress is the greatest at the centre. If the electrical current flows in a material with a temperature gradient, a thermoelectrical effect (Thomson effect) can take place [36]. It can lead to a shift of the temperature peak in the nanowire depending on the direction of electric current. This effect is more significant in semiconductors [37, 38].

1.2.4. Median time to failure and accelerated electromigration experiments

J. R. Black was the first to derive an empirical expression for calculating the median time to failure (MTF) for a wire due to electromigration [19]:

$$MTF = \frac{A}{j^2}\exp(\frac{E_a}{k_B T}), \tag{1.8}$$

where A is a constant depending on the material properties (geometry, diffusion constant, etc.), j is the current density, T is the temperature, E_a is the electromigration activation energy, k_B is Boltzmann constant. As can be seen from Black's equation (1.8), the lifetime of wires is inversely

proportional to the current density squared and scales inverse exponentially with the temperature. Electromigration experiments on material degradation are often conducted in a way to obtain the necessary information about failure mechanism in a reasonable time frame [39]. In this thesis *in situ* TEM experiments on electromigration studies were performed in accelerated regime, where the current density was intentionally increased to minimize the experiment time to several minutes.

References

1. P. R. Justinson. *Analysis of Electromigration in Single- and Dual-Inlaid Cu Interconnects*. Dissertation, The University of Texas at Austin, 2003.

2. C.-K. Hu, L. Gignac, R. Rosenberg. *Electromigration of Cu/low dielectric constant interconnects.* Microelectronics and Reliability, 2006, 46, 213 – 231.

3. International Technology Roadmap for Semiconductors (ITRS), 2011, Edition, Online: www.itrs.net/reports.html, 2012.

4. J. Lienig. *Electromigration and Its Impact on Physical Design in Future Technologies.* Proc. of the Int. Symposium on Physical Design (ISPD) 2013, 33–44.

5. I. A. Blech, E. Kinsbron. *Electromigration in Thin Gold-Films on Molybdenum Surfaces.* Thin Solid Films, 1975, 25, 327-334

6. A. Christou. *Electromigration and Electronic Device Degradation.* John Wiley & Sons Ltd, 1994.

7. C. M. Tan, A. Roy. *Electromigration in ULSI interconnects*. Materials Science and Engineering, 2007, 58, 1-75.

8. L. E. Murr. Handbook of materials structures, properties, processing and performance. Springer, 2015.

9. F. O. Hadeed and C. Durkan. *Controlled fabrication of 1–2nm nanogaps by electromigration in gold and gold-palladium nanowires*. Appl. Phys. Lett., 2007, 91, 123120.

10. G. Esen and M. S. Fuhrer. *Temperature control of electromigration to form gold nanogap junctions.* Appl. Phys. Lett., 2005, 87, 263101.

11. A. K. Mahapatro, S. Ghosh, D. B. Janes. *Nanometer Scale Electrode Separation (Nanogap) Using Electromigration at Room Temperature.* IEEE Transactions om nanotechnology, 2006, 5.

12. D. R. Strachan, D. E. Smith, D. E. Johnston, T.-H. Park, M. J. Therien, D. A. Bonnell, A. T. Johnson. *Controlled fabrication of nanogaps in ambient environment for molecular electronics*. Appl. Phys. Lett., 2005, 86, 043109.

13. H. Park, A. K. L. Lim, A. P. Alivisatos, J. Park, P. L. McEuen. *Fabrication of metallic electrodes with nanometer separation by electromigration.* Appl. Phys. Lett., 1999, 75, 301- 303.

13. B. Gao, E. A. Osorio, K. Babaei Gaven and H. S. J. van der Zant. *Three-terminal electric transport measurements on gold nano-particles combined with ex situ TEM inspection.* Nanotechnology, 2009, 20, 415207.

14. D. R. Strachan, D. E. Smith, M. D. Fischbein, D. E. Johnston, B. S. Guiton, M. Drndic, D. A. Bonnell, A. T. Johnson. *Clean electromigrated nanogaps imaged by transmission electron microscopy*. Nanolett., 2006, 6, 441-444.

15. M. Gerardin. Compt. Rend., 1861, 53.

16. H. B. Huntington, A. R. Grone. *Current-induced marker motion in gold wires.* J. Phys. Chem. Solids, 1961, 20, 76–87.

17. A. R. Grone. *Current-induced marker motion in copper.* Journal of Physics and Chemistry of Solids, 1961, 20, 88-93.

18. I. Blech. *Electromigration in Thin Aluminum Films on Titanium Nitride*. Journal of Applied Physics, 1976, 47, 1203-1208.

19. J. R. Black. *Electromigration - A Brief Survey and Some Recent Results*. IEEE Trans. on Electron Devices, 1969, 16, 338-347.

20. W. Seith, H. Z. Wever. *New Results on the Electrolysis of Solid Metallic Phases.* Elektrochem., 1955, 59, 942.

21. W. Seith, H. Z. Wever. *Uber einen neuen effekt bei der electrolytischen uberfuhrung in festen legierungen.* Elektrochem., 1953, 57, 891.

22. P. Ho, T. Kwok. *Electromigration in Metals*. Rep. Prog. Phys., 1989, 52, 301-348.

23. W. B. Fiks. *On the mechanism of the mobility of ions in metals*. Sov. Phys. Solid State, 1, 14-28 (1959).

24. R. Landauer, J. W. F. Woo. *Driving Force in Electromigration*. Physical Review B, 1974, 10, 1266-1271.

25. A. Lodder. *The Driving Force in Electromigration*. Physica A, 1989, 158, 723-739.

26. L. J. Sham. *Microscopic Theory of Driving Force in electromigration*. Physical Review B, 1975. 12, 3142-3149.

27. J. J. Clement. *Electromigration Modeling for Integrated Circuit Interconnect Reliability Analysis*. IEEE Trans. Dev. Mat. Rel., 2001, 1, 33-42.

28. A. S. Budiman, C. S. Hau-Riege, P. R. Besser, A. Marathe, Y.-C. Joo, N. Tamura, J. R. Patel, and W. D. Nix. *Plasticity-Amplified Diffusivity: Dislocation Cores as Fast Diffusion Paths in Cu Interconnects*. Proc. Intl. Reliability Physics Symp., 2007, 122-127.

29. K.N. Tu. *Recent advances on electromigration in very-large-scale-integration of interconnects*. J. Appl. Phys., 2003, 94, 5451-5473.

30. S. Pramanick et al. *Effect of mechanical stress on electromigration failure mode during accelerated electromigration tests*. Thin Films: Stresses and Mechanical Properties V, 1995, 356, 507-512.

31. I. A. Blech, C. Herring. *Stress Generation by Electromigration*. Appl. Phys. Lett., 1976, 29, 131-133.

32. C. Durkan. *Current at nanoscale. An introduction to Nanoelectronics*. Ed. I.C. Press 2007.

33. I. A. Blech and K. L. Tai. *Measurement of Stress Gradients Generated by Electromigration*. Appl. Phys. Lett, 1977, 30, 387-389.

34. J. R. Lloyd. *Electromigration and Mechanical Stress*. Microelectron. Eng., 1999, 49, 51-64.

35. M. Jakob. *Heat transfer*. Willey, 1949, 11.

36. W. Thomson. *On a mechanical theory of thermoelectric currents*. Proc. Roy. Soc. Edinburgh, 1851, 91–98.

37. T. D. Sands. *Designing Nanocomposite Thermoelectric Materials*. 2005.

38. P. J. Price. *Theory of Transport Effects in Semiconductors: Thermoelectricity*. Phys. Rev., 1956, 104, 1223.

39. S. Foley, et al. *A comparison between normally and highly accelerated electromigration tests*. Microelectronics and Reliability, 1998, 38, 1021-1027.

Thesis Outline

This thesis consists of seven Chapters. **Chapter 1** gives a brief introduction to electromigration phenomenon in thin conductors that are used in modern-day integrated circuit industry. A description of main physical principles and causes of electromigration is given. **Chapter 2** presents an overview of the experimental techniques used in this thesis. It gives a short introduction to a method of transmission electron microscopy (TEM), an overview of clean room sample fabrication for *in situ* TEM studies and a description of experimental setup for *in situ* experiments. In **Chapter 3** we present a new clean room fabrication technique (called back side lithography technique) that provides smooth and uniform electron viewing transparent windows at certain locations on a SiN membrane which is usually used in MEMS-based chips for *in situ* TEM experiments. Also, one of the possible applications of back side lithography technique is shown. In **Chapter 4** the electrical properties of segments of tapered InAs nanowires (NWs) are investigated by *in situ* TEM with simultaneous I–V measurements using good ohmic contacts. Also, the electrical breakdowns *in situ* TEM of individual InAs NWs are studied. It is showed that when the current is strongly increased, a breakdown of the NW occurs close to the cathode side, whereby the main changes are an electromigration of In and a sublimation of As. The possible mechanism for the breakdown process is proposed. In **Chapter 5** we present *in situ* TEM, scanning TEM (STEM) and TEM holography experiments on controlled electrical breakdowns of InAs NWs while simultaneously recording the I–V properties. We show that, by selecting the voltage and the rate of voltage ramp in breakdown experiments, it is possible to modify the geometry of the nanowire by forming a thin bridge at a curtain segment of the nanowire. Moreover, the location of this bridge in the nanowire can be changed under a change of electrode polarity. We show that the formed bridge can be placed at a specific location by an accurate choice of voltage value and voltage polarity in the experiments. Using EDX technique it is concluded that the composition of the bridge and the adjoined parts of the NW are similar.

From TEM holography data the local variations of the resistance in the nanowire are analyzed. A possible mechanism of electrical breakdown in InAs NWs is given. **Chapter 6** presents an *in situ* TEM visualization of electromigration-induced nanogap formation in AuPd nanowires. The electromigration is performed in two modes: a bias ramping (BRE) mode and feedback control mode (FCE). We show that the mechanism of nanogap formation differs between these two modes due to the different program algorithms of voltage applying. Also, the time stability of electromigrated nanogaps obtained by both techniques and the changes in the shapes of electrodes and the sizes of the nanogaps are analyzed. In **Chapter 7** we present *in situ* TEM formation of a single-crystalline bismuth film on an amorphous substrate. We show that thin polycrystalline Bi films can be modified into [111]-oriented monocrystalline films by *in situ* TEM heating and electron-beam bombardment with the energy of electrons 300 keV, whereby a unique feature is that the original thickness of the film is maintained. The single-crystalline area is created by heating the film close to the melting temperature and using an electron beam to achieve local melting. The film thickness is maintained by confining it with SiN on one side and with bismuth oxide or Al_2O_3 on the other side. Also, we show that bismuth films behave differently if no capping Bi-oxide layer is present, a configuration in which dewetting takes place and the film collapses when heated under similar conditions.

CHAPTER 2

Experimental techniques

The experimental techniques used in this thesis are briefly described in this Chapter. In the first section an introduction is given to a method of transmission electron microscopy (TEM). In the second section an overview of clean room processing of chip/sample fabrication for in situ TEM studies is presented. In the third section an experimental setup for in situ experiments is described.

2.1. Experimental methods

Throughout the studies presented in this thesis, methods of transmission electron microscopy and spectroscopy techniques were used. This chapter gives a brief overview of these techniques.

2.1.1. Transmission Electron Microscopy (TEM)[i]

Brief historical overview

In 1925 Louis de Broglie theorized the wave-like behaviour of electrons [5]. Later, in 1927 two independent research groups performed electron-diffraction experiments, which confirmed the wave nature of electrons. Then, in 1932 Max Knoll and Ernst Ruska brought the idea of electron lenses into a practical reality and introduced their first electron microscope [6]. For this invention Ernst Ruska was awarded the Nobel Prize in Physics in 1986 [7]. Later, in 1939, Siemens and Halske started the production of commercial TEMs in Germany. Also TEMs became available from other well-known today companies as JEOL, Hitachi and Philips. For material scientists a most important development took place in the late 1940s when Heidenreich [8, 9] and later Bollman [10] and Hirsh developed the techniques for thinning metal foils to electron transparency. Also, the development of theory of electron-diffraction contrast in Cambridge allowed to material scientists to identify all known line and planar defects from TEM images.

Today TEM is one of the most efficient and versatile tool for material characterization on atomic scale. The achievement in correction of spherical aberration has pushed the resolution of modern TEMs to well below 1 Å barrier [11]. With such an advanced TEMs it is possible to investigate nanoscale sized samples and easily visualise the arrangements of atomic column in crystalline materials. A technique allowing an atomic visualization is called high resolution TEM (HRTEM) technique. Another well

[i] Most of the text in this section has been adapted from references [1-4]

used sophisticated TEM techniques are scanning transmission electron microscopy (STEM), high-resolution STEM and analytical electron microscopy (AEM). Combination of these TEM techniques allows to characterize the materials entirely, providing with information on modulations in chemical identity on atomic level, crystal orientation, electronic structure and sample induced electron phase shift as well as the absorption based imaging.

Basics of transmission electron microscopy

Transmission electron microscopy is a technique in which a high-energy electron beam is transmitted through an ultra-thin specimen, interacting with the specimen resulting in an image. The image is magnified and focused onto an imaging device, such as a fluorescent screen or detected by a sensor such as a CCD camera.

The main components of a transmission electron microscope are the illumination system, the objective lens/holder stage and the imaging system. A main part of the illumination system is an electron gun, which produces and accelerates a beam of electrons to an energy in the range 20-1000 keV due to high tension. Modern TEMs are equipped with a field emission gun since this type of source produces an electron beam that is smaller in diameter and more coherent, provides with a greater current density or electron-optical brightness and stability of the beam in comparison with W- and LaB_6-filament sources. Table 2.1 shows the comparison of operating parameters for different types of electron sources [12]. Then, the electron beam passes through a system of condenser lenses before it reaches the sample: the first strong magnetic lens (condenser lens C1) that forms a virtual source of the gun, the second and the third magnetic lenses (condenser lenses C2 and C3) serve to allow the diameter of illumination at the specimen to be varied continuously over a wide range and to make a parallel or converged electron beam. The first mode is used primarily for TEM imaging and selected area diffraction (SAD), while the second is used mainly for scanning (STEM) imaging, analysis via X-ray and electron spectrometry, and convergent beam electron diffraction (CBED). Further, the electron beam passes through a thin foil of material (specimen)

Type of source	Tungsten thermionic	LaB_6 thermionic	Schottky emission	Cold field emission
Material	W	LaB_6	ZrO/W	W
φ (eV)	4.5	2.7	2.8	4.5
T (K)	2700	1800	1800	300
E (V/m)	low	low	$\approx 10^8$	$> 10^9$
J_e (A/m^2)	$\approx 10^4$	$\approx 10^6$	$\approx 10^7$	$\approx 10^9$
β (Am^{-2}/sr^{-1})	$\approx 10^9$	$\approx 10^{10}$	$\approx 10^{11}$	$\approx 10^{12}$
d_s (μm)	≈ 40	≈ 10	≈ 0.02	≈ 0.01
Vacuum (Pa)	$< 10^{-2}$	$< 10^{-4}$	$< 10^{-7}$	$\approx 10^{-8}$
Lifetime (hours)	≈ 100	≈ 1000	$\approx 10^4$	$\approx 10^4$
ΔE (eV)	1.5	1.0	0.5	0.3

Table 2.1. Operating parameters of different types of electron source: φ is the work function, T is the temperature, E is the electric field, J_e is the current density and β is the electron-optical brightness; d_s is the effective (or virtual) source diameter, and ΔE is the energy spread of the emitted electrons [12].

which results in the electron wave at the back exit-face of the specimen containing information about crystal potential. The objective lens takes the electrons emerging from the exit surface of the specimen, disperses them to create a DP in the back-focal plane, and recombines them to form an image in the image plane. The imaging system (the intermediate and projector lenses) serves to magnify the image or the DP produced by the objective lens and to focus these on the viewing screen or computer display via a detector, CCD, or TV camera. A schematic diagram showing the main parts of the microscope can be seen in figure 2.1. Below we will discuss the main operational modes of TEM used in this thesis.

Diffraction and Image formation in TEM

The TEM specimen (thin foils, small nanoparticles and etc.) transparent for the electron beam is placed in the objective lens, which forms an image of the electron density distribution at the exit surface of the specimen based on the electron optical principles. A diffraction pattern is formed in the back focal plane of the objective lens and the

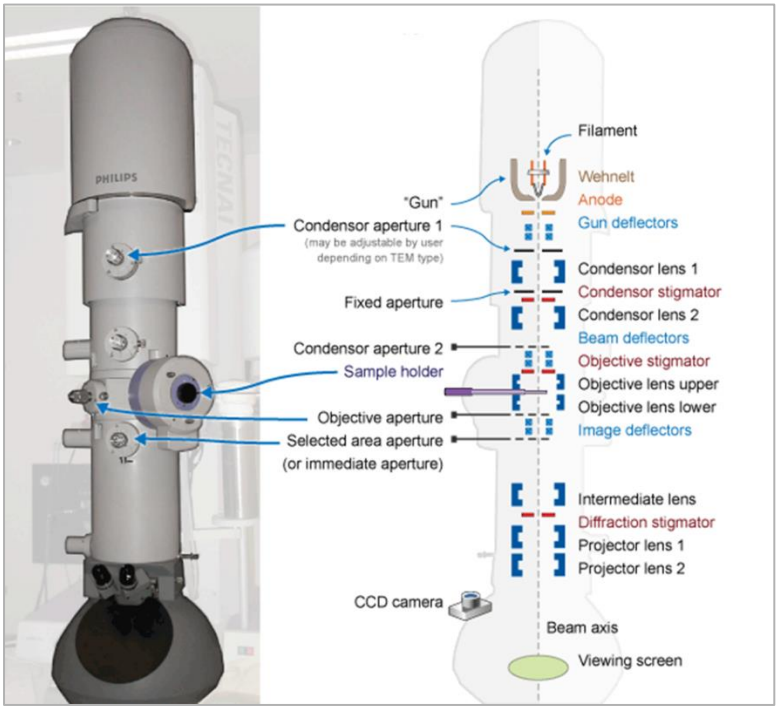

Figure 2.1. A typical TEM (on the left) and a schematic diagram (on the right) showing the main parts of TEM [13].

recombination of the diffracted beams forms an image in the image plane of the objective lens. The diffraction, intermediate and projection lenses which are placed below the objective lens are used to focus and magnify either the diffraction pattern or the image onto a fluorescent screen, which converts the electrons into visible light signal or CCD camera. The scheme of diffraction and imaging operation modes are illustrated in figure 2.2 (a) and (b) respectively.

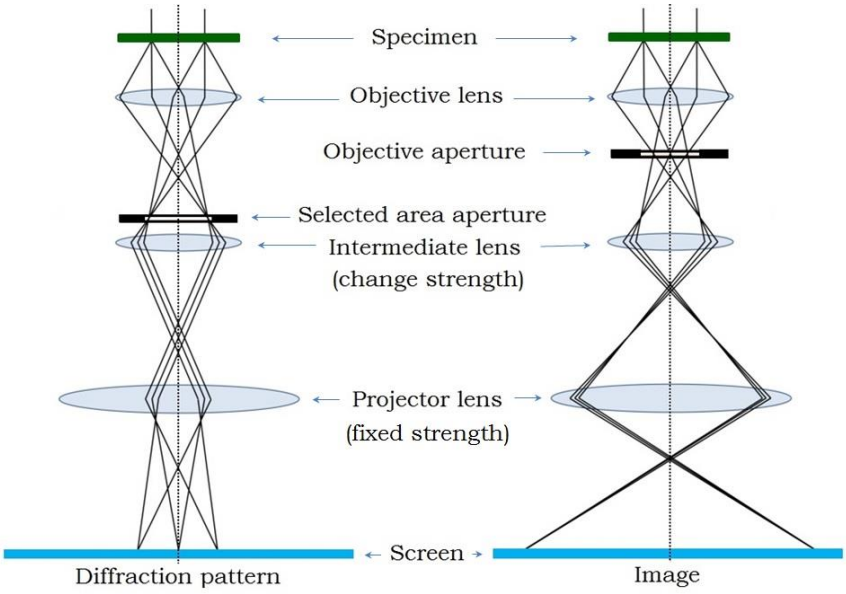

Figure 2.2. Schematic illustration of diffraction and imaging modes in TEM.

In diffraction mode a selected area aperture serves to select an specimen area of interest in order to obtain a diffraction pattern from a local region. Depending on the size of the aperture, the area of the sample from which the diffraction pattern is obtained can be controlled. The diffraction mode allows to reveal whether a material is amorphous, polycrystalline or single-crystal. For a single crystal diffraction pattern consists of spots distanced away from the central (nondiffracted) spot by $\frac{1}{d_{hkl}}$, where d_{hkl} is the interplanar spacing between *hkl* planes. If the sample is polycrystalline with randomly oriented individual crystals, the diffraction pattern represents rings of constant radius. For nanocrystalline materials with a small crystal size, the diffraction pattern will consist of more continuous rings. Amorphous materials do not contain long-range order in the atomic lattice and produce diffuse ring diffraction patterns with no discrete reflections. As an example, diffraction patterns of single crystalline, polycrystalline and amorphous materials are shown in figure 2.3. Therefore, selected area diffraction can be used to identify the crystallographic structure, symmetry, and orientation of selected area in the specimen;

measure the lattice parameter or identify if more than one phase is present [14-16].

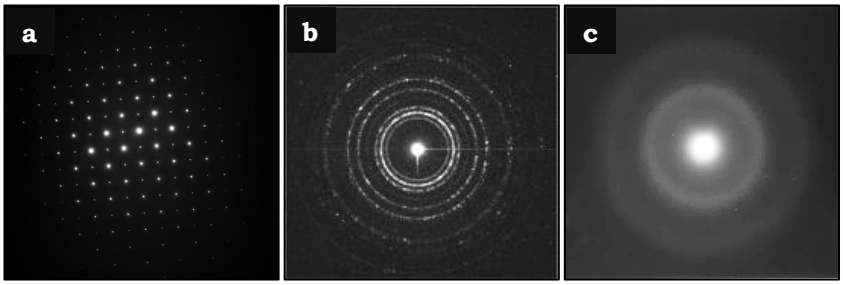

Figure 2.3. Typical electron diffraction patterns of (a) a single crystal, (b) polycrystalline sample [17] and (c) amorphous materials [18].

In image mode, when diffraction pattern is produced, by insertion of objective aperture (5-70 μm in diameter) in the back focal plane of objective lens (where the diffraction pattern is formed), the diffraction spots can be selected and different types of images can be obtained depending on which diffraction spot contributes to the image. When the objective aperture is positioned to intercept all diffracted beams and only allow the central beam (or primary beam) to form an image. A bright-field image (BF-image) is produced. Alternatively, when the objective aperture is displaced from the optic axis to intercept the central beam and allow a certain diffracted beam to contribute to the image, the displaced aperture dark field image is formed. This type of image is of a poor quality because the additional spherical aberration and astigmatism present when the electron path is not close to the optic axis. To retain the resolution of the BF mode, the electron beam incident on the specimen can be tilted so that the diffracted electrons travel along the optical axis. This technique is called centred dark field imaging and the image obtained by this technique is called dark-field image (DF-image). Using these techniques the detailed information about various structural defects in the specimen can be obtained [19, 21]. A schematic illustration of the formation of BF- and DF-images is presented in figure 2.4 [21].

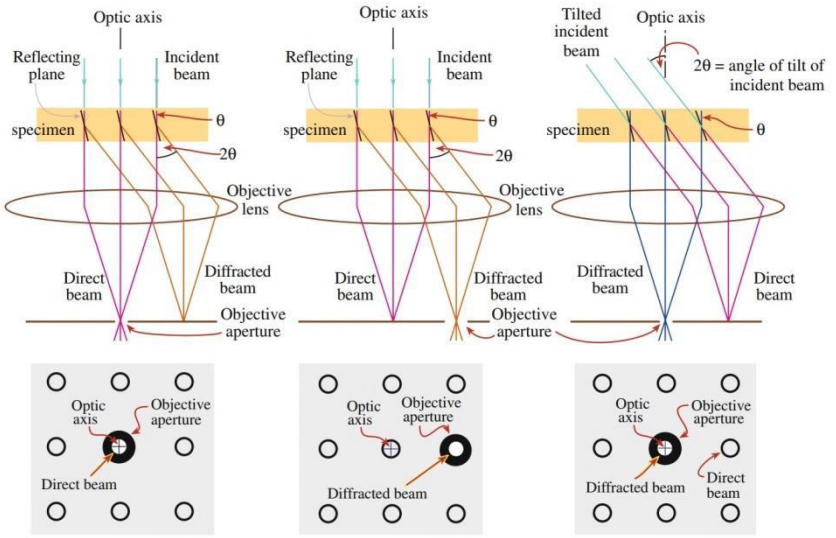

Figure 2.4. Ray diagrams showing how the objective lens and objective aperture are used in combination to produce a BF image (left image) formed from the direct electron beam, a displaced-aperture DF image (middle image) formed with a specific off-axis scattered beam, and a centred DF image (right image) where the incident beam is tilted so that the scattered beam emerges on the optic axis. The area of the DP selected by the objective aperture, as seen on the viewing screen, is shown below each ray diagram [21].

In image mode, TEM can be operated under a variety of contrast mechanisms. The term “contrast” is defined as a difference in intensity between two adjacent areas. TEM image contrast arises because of the scattering of the incident beam by the specimen. As the electron wave traverses the specimen, it can change both its amplitude and its phase, which results in phase contrast and amplitude contrast (mass-thickness contrast and diffraction contrast) [22, 23].

Mass-thickness contrast arises from incoherent elastic scattering of electrons. The electrons passing through the specimen will be scattered off axis by elastic nuclear interaction, also called Rutherford scattering. Because elastic scattering is a strong function of the atomic number as well as the thickness of the specimen, regions of a specimen with high mass will scatter more electrons than regions with low mass of the same thickness.

Similarly, thicker regions will scatter more electrons than thinner regions. In the TEM the mass-thickness contrast is affected by the size of the objective aperture and the accelerating voltage. Smaller apertures will increase the difference in the ratio of scattered and transmitted electrons and as a consequence will increase the contrast between regions of different thickness or mass. Lowering the accelerating voltage will lead to similar effect since the scattering angle and the cross section increase which also will cause increase in the relative contrast between higher mass and lower mass regions. Mass-thickness contrast is present in all kinds of specimens – crystalline or amorphous, but is most important for non-crystalline, amorphous materials as glasses. Also, it is the primary imaging mechanism in biological TEM applications. Schematic illustration of the mechanism of mass contrast formation is presented in figure 2.5 (a) [24]. Figure 2.5 (b) shows BF-TEM image of a silica particle supported on a carbon foil as an example for pure thickness contrast [25].

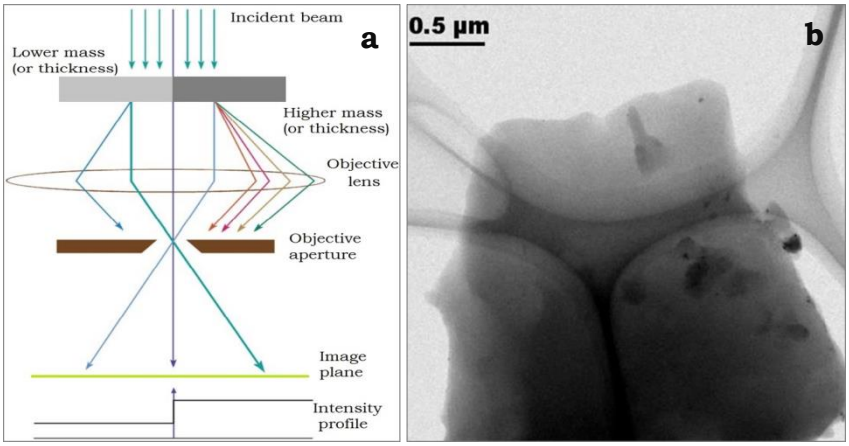

Figure 2.5. (a) Mechanism of mass-thickness contrast in a BF image [24]. (b) BF-TEM image of a SiO_2 particle on a holey carbon foil [25].

If the specimen is crystalline, another type of amplitude contrast plays a role – diffraction contrast. It arises from coherent elastic scattering of electrons, where the scattering occurs at Bragg angles (Bragg scattering) from certain crystallographic planes that are oriented closely parallel to the electron beam. As described above, the insertion of objective aperture into the back focal plane of the objective lens can result in two BF or DF imaging

mode depending on selected diffraction spot. In BF images the dark contrast regions is produced from areas that are aligned for Bragg diffraction. If the electrons have been diffracted by a specific set of *hkl* planes, in DF imaging the area that appears bright is the area where this *hkl* planes are at the Bragg condition. In case of single crystalline material, for a good diffraction contrast, the sample can be tilted such that only one diffracted beam is excited in addition to the central transmitted beam. This is referred to as a two-beam condition. This type of contrast allows observation of various linear and planar defects (dislocations, stacking faults, grain boundaries, etc.) in the crystals, analysis of their nature and type. Several examples of diffraction contrast are shown in figure 2.6.

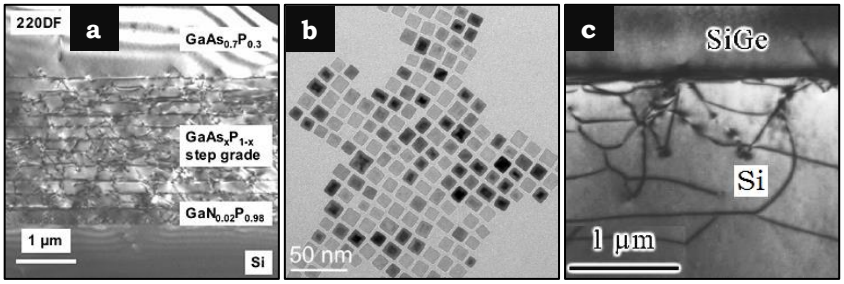

Figure 2.6. Several examples of diffraction contrast: (a) cross-sectional TEM DF-image image reveals misfit dislocations generated in $GaAs_xP_{1-x}$ compositionally step graded layers grown by metal organic chemical vapor deposition on Si [26]; (b) BF TEM image of 2D square arrays consisting of cubic $Fe_xO/CoFe_2O_4$ core/shell nanoparticles [27]; Cross-sectional DF TEM image (g=220) of SiGe/Si(001) interface [28].

Another type of contrast which can be well produced in TEM is phase contrast. The difference between phase contrast and diffraction contrast is the number of electron beams collected by the objective aperture. Phase contrast is formed due to the interference of multiple beams at the exit of the specimen resulting in a series of sinusoidal oscillations in intensity, normal to the diffracting vector g and of periodicity 1/g. Under these conditions, atomic-resolution lattice images can be obtained. This technique of obtaining atomic-resolution images is called high-resolution transmission electron microscopy (HRTEM). Currently, with

the introduction of spherical-aberration correctors, point-to-point resolutions of 0.5 Å is possible.

2.1.2. Scanning Transmission Electron Microscopy (STEM)

Another type of TEM operation is scanning TEM (STEM) [29-33]. In STEM mode, a fine, convergent electron beam (electron probe) produced by a FEG and two condenser lenses is focused on the specimen and using double deflection scan coils it is scanned over a thin specimen (typical probe size is 0.05 to 0.2 nm). In STEM mode the role of objective aperture is performed by electron detectors to select transmitted or diffracted electrons. There are two principal types of electron detectors - bright-field (BF) and dark-field (DF) STEM detectors. The BF detector is located on the optical axis, where it captures the directed electrons. The DF detector represents a disk with a hole, also located on the optical axis, and detects scattered electrons. Among the dark-field detectors, the most commonly used is the high-angle annular dark-field (HAADF) detector that captures electrons that are incoherently elastically scattered (Rutherford scattering) inelastically scattered (thermal diffusive scattering) to higher angles (figure 2.7). Therefore, using HAADF detector while imaging in STEM mode, it is possible to visualise the lattice with Z-contrast (atomic number contrast). It is understood that the images collected from beams elastically scattered at higher angles (50 – 150 mrad) show a dependency on the atomic number approximately as $Z^{1.7}$. Since there is no coherency between the high angle scattered beams which are collected on an annular detector, in a high resolution STEM (HRSTEM) image obtained with a HAADF detector, the intensities from individual scattering centres (atoms) along the beam path can be added enabling a direct interpretation of atom types and positions. Also, it is possible to visualize either diffraction contrast or thickness contrast of the sample (which is not influenced by elastically scattered electrons that contribute to diffraction contrast) by means of changing the camera length. Combination of all these imaging techniques can provide with complete morphological and structural information of a specimen at the atomic scale. Particularly with an aberration-corrected STEM, this technique is capable of identifying atomic resolution changes in

composition. This capability is of great interest to study surface and interfacial segregation of elements as well as atomic variations in composition in nanostructures.

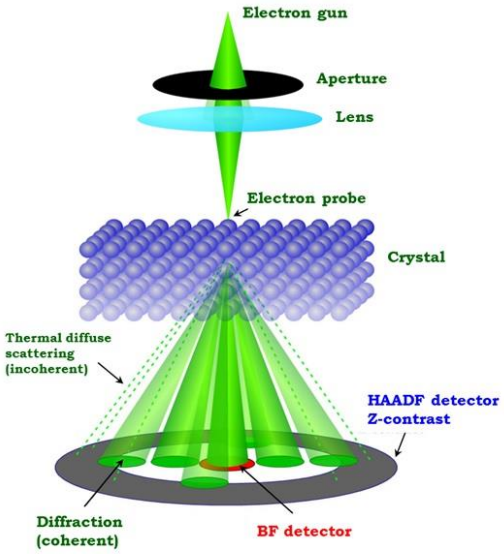

Figure 2.7. Schematic illustration of STEM mode [32].

2.1.3. Elemental Analysis: Energy Dispersive X-ray Spectroscopy

A significant advantage of TEM studies is the combination of the imaging techniques with the other generated signals to analyse the chemistry of the specimens. This type of TEM is called analytical TEM and the study is called microanalysis in TEM. Most of the modern TEMs are equipped to perform STEM along with energy dispersive X-ray spectroscopy (EDX) as well as electron energy loss spectroscopy (EELS) and energy filtered transmission electron microscopy (EFTEM). Part of the studies in this thesis was done using EDX spectroscopy and a brief overview of this technique is given below.

EDX spectroscopy method is a powerful technique of qualitative and quantitative chemical characterization of material in TEM. This

technique is based on the fact that in atom electrons occupy different energy levels (binding energies) represented with K, L, M and etc. shells (figure 2.8). The difference in energy between these electron shells is characteristic for each element. In TEM a highly accelerated beam of electrons can interact with the electrons of atoms in TEM sample by exciting and kicking out them from their inner atomic shells, an electron from outer shell falls to the inner shell releasing an energy as an X-ray photon. Several characteristic X-rays can be generated from a single element depending on which inner shell an electron is kicked out and from which outer shell an electron falls to the inner shell (labelled with Kα, Lα and Kβ in Figure 2.8). The emitted X-ray photons are collected using special detectors and plots of X-ray counts versus X-ray energy are generated. From the intensities of the peaks corresponding to specific elements, it is possible to quantify and estimate the elemental composition of a specimen [33].

The quantitative information of elements present in the sample is estimated from the relation between the weight fraction and generated intensities (ionisation cross-section), given by the Cliff-Lorimer method: for two elements (A and B) the intensities of these elements in the EDX spectrum (I_A and I_B) are proportional to the weight fraction of these elements (W_A and W_B) with the Cliff-Lorimer factor (K_{AB}):

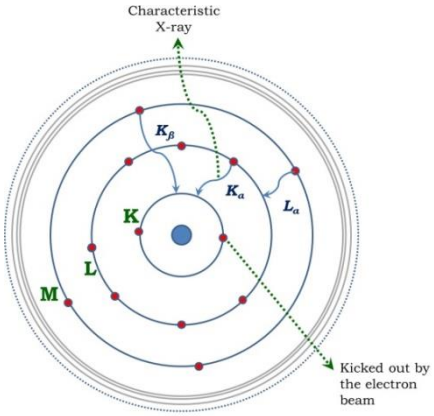

Figure 2.8. Schematic illustration showing X-ray generation by an atom in TEM sample due to interaction with an electron beam.

$$\frac{W_A}{W_B} = K_{AB}\frac{I_A}{I_B}\,. \tag{2.1}$$

Note that the effects of fluorescence and absorption can be neglected since a TEM specimen is quite thin.

2.2. Sample fabrication

In this section we present the description of fabrication process of the chips which we produced in Kavli Nanolab Delft and used for in-situ TEM studies presented in this thesis. According to the process flow the chip fabrication can be divided into two main parts:

- fabrication of silicon chips with thin, free-standing silicon nitride membranes (windows and markers);
- fabrication of either electrical contacts or nanobridges together with electrical contacts on top of free-standing silicon nitride windows.

We start with a 400 μm-thick silicon wafer polished from both sides. Using low-pressure chemical vapour deposition (LPCVD) 100-nm thick low-stress silicon nitride (SiN_x) layers are grown on both sides of the silicon wafer. Then, in order to protect the wafer before dicing into 14x14 mm^2 squares it is coated with AZ5214 resit by spin coater with the rotation speed of 1000 rotation per minute (rpm) on both sides and for each side the resist is baked for 20 minutes at 110°C. After dicing each square substrate 14x14 mm^2 (further substrate) is cleaned in fuming nitric acid for 10-15 minutes, rinsed with water to remove acid residues and dried. We start the fabrication of free-standing SiN_x-windows and markers onto these substrate. The detailed procedure of this fabrication part is shown in the following steps in figure 2.9. First, the prepared substrate (figure 2.9 (a)) is spin coated with a 500 nm-thick positive resist and baked (see figure 2.9 (b) and table 2.1 for additional information on type of resist and baking conditions). At this step we use just one resist layer because structures are coarse, high accuracy and consideration of proximity effects are not required. Then, an electron beam lithography (EBL) process step is performed: the substrate is exposed to a scanning electron beam (EB) generated by a 5000+ Leica pattern generator (figure 2.9 (c)). The layout file of the patterns for electron beam lithography is created with Layout

BEAMER software. E-beam exposure results in changes of physico-chemical structure of the positive resist so that the exposed areas become high developer-soluble. Next, to open the e-beam written structures the resist development process is done in solution of methyl isobutyl ketone(MIBK) and isopropyl alcohol (IPA) with the ratio MIBK:IPA=1:3 during 70 seconds and to stop the development process the substrate is kept in IPA for 50 seconds, then nitrogen gun is applied to dry the substrate (figure 2.9 (d)). The opened SiN_x layers are removed by an anisotropic low-pressure reactive ion etching (RIE) in a Leybold RIE etcher system using CHF_3/Ar gases with

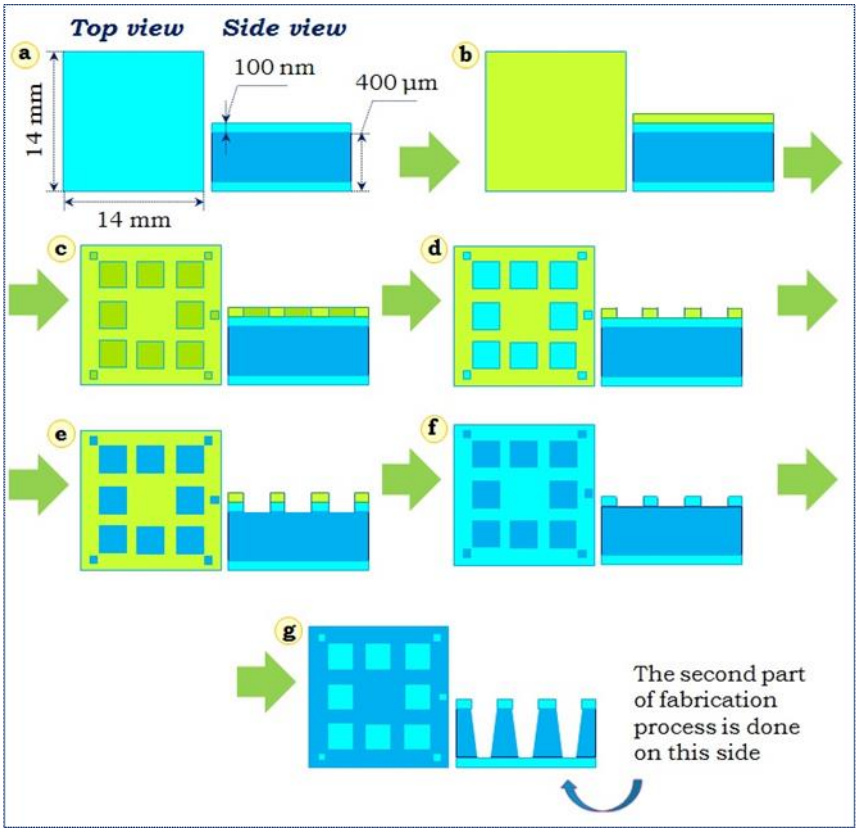

Figure 2.9. Schematic illustration of fabrication process of silicon substrates with thin, free-standing silicon nitride membranes (windows and markers) (see the description in the text).

gas flow 25/25 standard cubic centimetres per minute (sccm), chamber pressure 8 μbar and forward power 50 W. For this conditions the etching rate is 20 nm/min and this process takes 5 minutes (figure 2.9 (e)). The remaining resist is removed by washing in hot acetone at 52°C for 30 minutes. Then, to remove any residue it is rinsed in IPA and dried (figure 2.9 (f)). Finally, KOH wet etching is done to remove silicon from the areas which are not SiN_x-covered. For KOH etching we use 33%-KOH solution heated to 85°C (for these parameters the etch rate is 100μm/hour approximately). After KOH-etching the substrates are cleaned first with water, washed by acetone, IPA and dried (figure 2.9 (g)). Thus, substrates with markers and thin, free-standing SiN_x-windows are ready for the second part of fabrication process.

Schematic illustration of the second fabrication part is presented in figure 2.10. The second part of chip preparation can include fabrication of:

1. only electrical contacts on top of transparent SiN_x-windows (to be used for electrical measurements of semiconductor nanowires as described in Chapter 4 of this thesis);
2. metallic nanobridges together with electrical contacts on top of SiN_x-windows (corresponding experiments are described in Chapter 6).

For fabrication of electrical contacts the substrate (figure 2.10 (a)) is coated with two types of positive resist; each layer of resist is baked (see figure 2.10 (b) and Table 2.1). Using mixed layers improves the sensitivity and thermal stability of the resist. Using one EBL process the pattern of electrical contacts is generated with 20 nm- and 100 nm-resolution for fine and coarse areas of contact pads respectively (figure 2.10 (c)). After resist development (see figure 2.10 (d)) the structures are open and subsrate is ready for deposition of metal film (Au or Pt) for electrical contacts. The deposition is performed using Temescal FC-2000 electron beam evaporator. For electrical contacts we usually deposit 5 nm-thick Cr as an adhesion layer with the rate 0.5 Å/sec and 95 nm-thick Au (or Pt) layer with the rate 1.5 Å/sec (figure 2.10 (e)). The deposition is directly followed by a lift off procedure in hot acetone (52°C) for 30 minutes (figure 2.10 (f)). After rinsing with IPA and drying, the substrate is cleaved into eight 3x3 mm^2 chips with diamond pen for further out-of-clean room manipulations.

In principle, the fabrication of metallic nanobridges with contacts is the same as fabrication of only electrical contacts described above, the only difference is an additional step of spin coating, EBL, metal deposition and lift off procedure. The additional step is required because the material of nanobridges is usually different than of electrical contacts; the thickness of nanobridges used in our studies is 15-20 nm; the total thickness of the resist layers is less; for nanobridges EBL process is performed with 5-10 nm resolution.

The EBL patterns for fabrication of electrical contacts and metallic nanobridges with contacts are shown in figure 2.11.

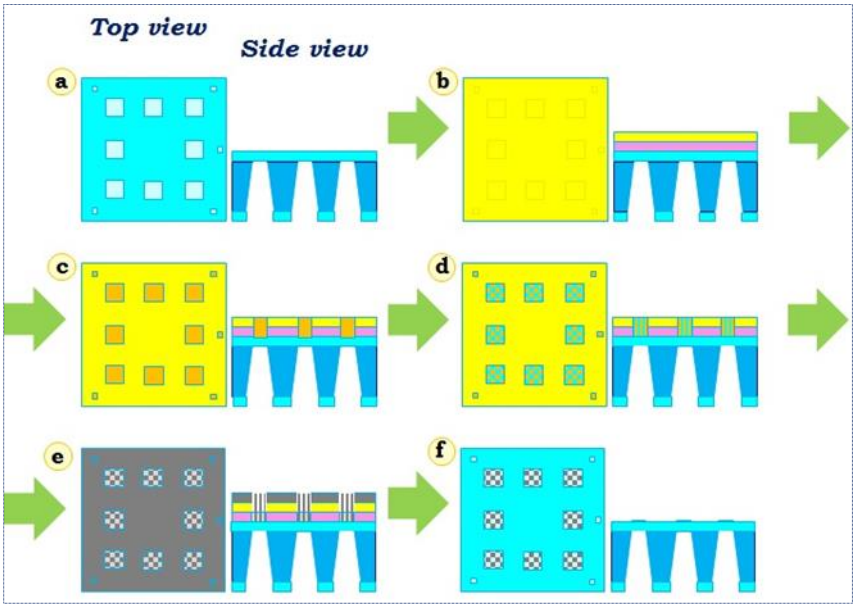

Figure 2.10. Schematic illustration showing fabrication process of structures on top of SiN_x-windows – electrical contacts or metallic nanobridges together with electrical contacts. For fabrication of metallic bridges with contacts the additional steps (b)-(f) are required (see the description in the text).

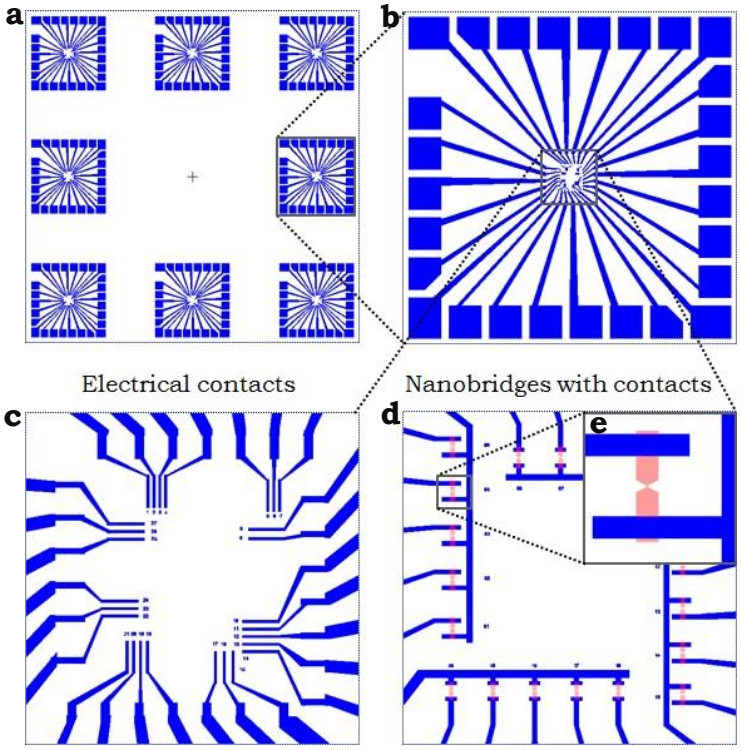

Figure 2.11. EBL-patterns designed in L-Edit software. (a) A design for 14x14 mm^2 substrate. One substrate contains eight 3x3 mm^2 chips. (b) 3x3 mm^2 chip which can be designed for fabrication of either electrical contacts (c) or nanobridges with contacts (d). (e) Enlarged area of (d) showing nanobridges (presented in red colour) and Au (Pt) contacts (blue colour).

Fabrication step	Resist type and spinning parameters	Baking parameters
SiN_x-windows and markers	Resist type: PMMA 950k[1], 7% in anisole[2]; Thickness: 500 nm; Spinning parameters: 5000 rpm, 55 sec	Temperature: 175°C; Time: 60 minutes
Electrical contacts	PMMA/MMA[3] (17.5%), 8% in Ethyl-L-Lactate; 300 nm; 3000 rpm, 55 sec. PMMA 950k, 4% in anisole; 250 nm; 3000 rpm, 55 sec.	175°C, 20 minutes; 175°C, 30 minutes.

Nanobridges	PMMA/MMA (17.5%), 8% in Ethyl-L-Lactate; 300 nm; 3000 rpm, 55 sec. PMMA 950k, 3% in anisole; 130 nm; 3000 rpm, 55 sec.	175°C, 15 minutes; 175°C, 30 minutes.

Table 2.1. Overview of resist types, spin coating parameters and baking conditions.

[1] PMMA (polymethyl methacrylate) is most commonly used positive e-beam resist containing long polymer chains of carbon atoms and comes in different molecular weights. The two standard PMMA resists are 495k and 950k. PMMA provides high contrast and high resolution structures.

[2] Anisol is a solvent for PMMA. (Usually, PMMA come in a form of powder. This powder is dissolved in anisol to obtain the desired concentration).

[3] MMA is methyl methacrylate; the use for MMA/PMMA bilayers is for good lift-off of metallic structures.

2.3. Measurement setup

2.3.1. *In situ* TEM

In situ TEM is a powerful technique for the field of material science since it allows direct observation of the dynamic response of a material to applied external conditions such as electrical bias [34, 35], heating [36, 37], reactive environment interaction [38], etc. in the real time. Moreover, i*n situ* TEM experiments can provide new knowledge and deep understanding of physico-chemical mechanisms occurring in material at the nanoscale. Unique capabilities of *in situ* TEM experiments are the result of combination of both state-of-art TEM microscopes and advanced TEM-holders developed for various external stimuli. In this thesis *in situ* TEM experiments were performed using a FEI Titan microscope operating at 300 keV.

2.3.2. Holders for *in situ* TEM measurements

Electrical measurements

A built-in-house holder used for *in situ* TEM electrical measurements in this thesis allows voltage/current stressing to modify a sample in a controlled, desired way *in situ* TEM. To apply bias this holder contains eight separate electrical lines passing from the tip through the holder to an electrical connector. The lines are air tight and allow the electrical measurements to be performed inside the microscope. The holder is presented in figure 2.12. Al_2O_3 chip carriers are used to connect a chip containing the sample to TEM-holder. To fix a chip onto an Al_2O_3 chip carrier conductive tape is used and to provide the electrical connection between chip and holder, the standard wire-bonding technique is applied.

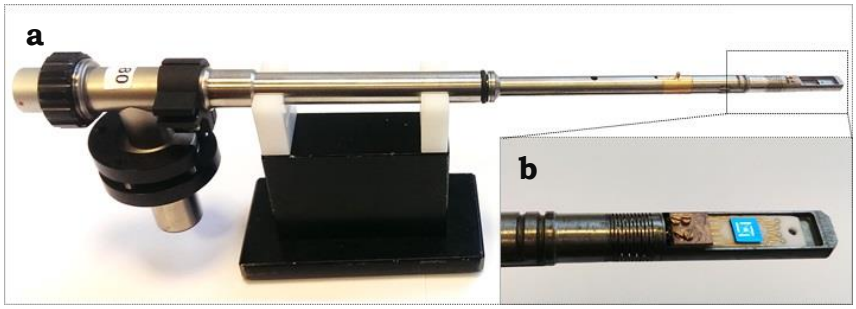

Figure 2.12. (a) TEM-holder for in situ electrical measurements. (b) Enlarged area of (a) showing the tip of the holder with loaded chip-like sample connected to Al_2O_3 carrier.

Heating experiments

Heating experiments in this thesis were carried out using built-in-house heating holder and MEMS-based heating chips. The tip of the holder contains four fixed electrical wires (pins), which are placed on four contact pads of MEMS based heater (figure 2.13). (see the details of preparation of MEMS-based heating chips in [40]). The electrical wires pass through the holder to the connector which is plugged in to the heating controller box. The heating control software allows to set a desired temperature.

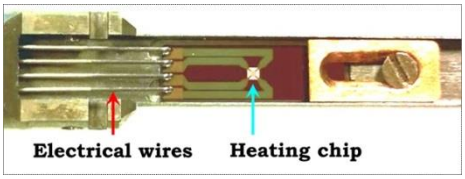

Figure 2.13. The tip of the heating holder and MEMS-based heating chip.

Also, it is possible to conduct the combined *in situ* TEM electrical and heating experiments. It can be done using either heating holder with additional two wires for voltage applying and corresponding MEMS-based heating chips (six contact pads, two of them are for electrical measurements) or holder for electrical measurements where the MEMS-based heating chip with six contact pads is wire-bonded to Al_2O_3 chip carrier (see figure 2.14). The application of this type of experiments is discussed in Chapter 3.

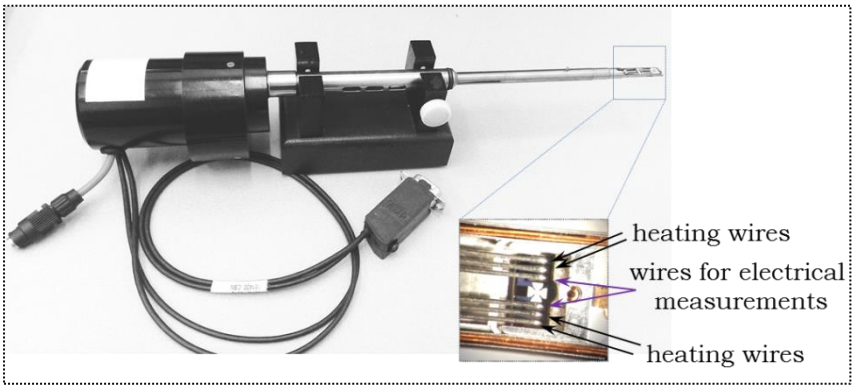

Figure 2.14. The tip of the combined heating and biasing double tilt TEM holder.

2.3.3. Setup for electrical measurements

The setup that enables electrical measurements is shown in figure 2.15 and includes several main parts – IVVI rack, Matrix module, ADwin-GOLD module connected to computer. The built-in-house measurement electronics setup IVVI rack (designed by R. Schouten, TU Delft [41]) contains several modules: voltage sources, current sources,

current-voltage converters, and voltage amplifiers. All these modules are set in a shielded rack. The system allows to send/receive electrical signals to/from the chip containing a sample and engineered to reduce external influences such as noise and interference signals. The holder is connected via cable to a matrix box. ADwin-GOLD [42] serves to connect IVVI rack with computer to operate the experiment All circuits connected to the measurement setup are battery-operated and isolated.

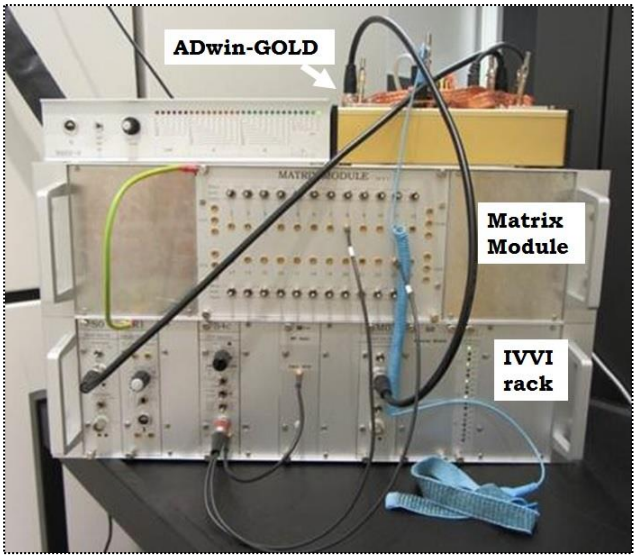

Figure 2.15. Setup for electrical measurements.

References

1. D. B. Williams, C. B. Carter. *Transmission Electron Microscopy*. Springer, 2009.

2. R. F. Ergerton. *Physical Principles of Electron Microscopy.* Springer, 2005.

3. L. Reimer, H. Kohl. *Transmission Electron Microscopy. Physics of image formation.* Springer, 2008.

4. P. B. Hirsch, A. Howie, R. B. Nicholson, D. W. Pashley, M. J. Whelan. *Electron Microscopy of Thin Crystals*. R. E. Krieger Publishing Company, 1977.

5. L. de Broglie. *Researches on the quantum theory*. Ann. Phys., 1925, 3, 22-128.

6. M. Knoll, E. Ruska. *Electron Microscope*. Z. Phys., 1932, 78, 318-339.

7. E. Ruska. *The development of the electron microscope and of electron microscopy*. Reviews of Modern Physics, 1987, 59, 627-638.

8. R. D. Heidenreich, J. Appl. Phys., 1949, 20, 993.

9. R. D. Heidenreich, Bell. Syst. Techn., 1951, 30, 867.

10. W. Bollmann, Phys. Rev., 1956, 103, 1588.

11. C. Kisielowski. *Detection of single atoms and buried defects in three dimentions by aberration-corrected electron microscope with 0.5-A information limit*. Microscopy and Microanalysis, 2008, 14, 469-477.

12. R. F. Ergerton. Physical Principles of Electron Microscopy. Springer, 2005, 65.

13. http://www.ammrf.org.au/myscope/tem/introduction/

14. J. M. Cowley, *Diffraction Physics*. Elsevier, 1995.

15. T. E. Weirich, J. L. Lábár, X. Zou. *Electron Crystallography*. Springer, 2006

16. D. B. Williams, C. B. Carter. *Transmission Electron Microscopy*. Springer, 2009, v.1, ch. 1, 152.

17. https://str.llnl.gov/str/June05/Aufderheide.html

18. M. Ylönen, A. Torkkeli, H. Kattelus. *In situ boron-doped LPCVD polysilicon with low tensile stress for MEMS applications*. Sensors and Actuators A, 2003, 109, 79–87.

19. B. Fultz, J. Howe. *Transmission Electron Microscopy and Diffractometry of Materials*. Springer, 2013.

20. B. Williams, C. B. Carter. *Transmission Electron Microscopy*. Springer, 2009, v.1, ch. 1, 155.

21. B. Williams, C. B. Carter. *Transmission Electron Microscopy*. Springer, 2009, v.1, ch. 1, 156.

22. B. Williams, C. B. Carter. *Transmission Electron Microscopy.* Springer, 2009, v.3, ch. 22, 371-388.

23. B. Williams, C. B. Carter. *Transmission Electron Microscopy*. Springer, 2009, v.3, ch. 23, 389-403.

24. B. Williams, C. B. Carter. Transmission Electron Microscopy. Springer, 2009, v.3, ch. 23, 374.

25. F. Krumeich. *Properties of Electrons, their Interactions with Matter and Applications in Electron Microscopy*.

26. http://www.nrel.gov/pv/measurements/transmission_microscopy.html

27. A. O. Yalcin, B. de Nijs, Z. Fan, F. D. Tichelaar, et al. *Core-shell reconfiguration through thermal annealing in $Fe_xO/CoFe_2O_4$ ordered 2D nanocrystal arrays.* Nanotechnology, 2014, 25(5), 055601.

28. E. A. Steinman, V. I. Vdovin, T. G. Yugova, V. S. Avrutin, N. F. Izyumskaya. *Dislocation structure and photoluminescence of partially relaxed SiGe layers on Si(001) substrates*. Semicond. Sci. Technol., 1999, 14, 582.

29. S. J. Pennycook, P. D. Nellist. *Scanning Transmission Electron Microscopy.* Springer, 2011.

30. J. Thomas, T. Gemming. *Analytical Transmission Electron Microscopy*. Springer, 2014, 115-137.

31. J. Orloff's. *Handbook of Charged Particle Optics*. CRC Press, 2008.

32. https://microscopy.empa.ch/bin/view/Main/STEM

33. B. Williams, C. B. Carter. Transmission Electron Microscopy. Springer, 2009, v.4, ch. 32-34, 581.

34. B. Gao, M. Rudneva, K. McGarrity, Q. Xu, F. Prins, J. M. Thijssen, H. W. Zandbergen, H. S. J. van der Zant. *In situ transmission electron microscopy imaging of grain growth in a platinum nanobridge induced by electric current annealing*. Nanotechnology, 2011, 22(20).

35. C. Zhang, M. Neklyudova, L. Fang, Q. Xu, H. Wang, F. D. Tichelaar, H. W. Zandbergen. *In situ electrical characterization of tapered InAs nanowires in a transmission electron microscope with ohmic contacts.* Nanotechnology, 2015, 26(15), 155703.

36. A.O. Yalcin, et al. *Heat-induced transformation of CdSe–CdS–ZnS core–multishell quantum dots by Zn diffusion into inner layers.* Chem. Commun., 2015, 51, 3320-3323.

37. A.O. Yalcin, et al. *Atomic Resolution Monitoring of Cation Exchange in CdSe-PbSe Heteronanocrystals during Epitaxial Solid–Solid–Vapor Growth.* Nano Lett., 2014, 14, 3661-3667.

38. S. R. K. Malladi. *In-situ TEM Studies: Heat-treatment and Corrosion.* Dissertation, TU Delft, 2014.

40. M. A. van Huis, et al. *Atomic Imaging of Phase Transitions and Morphology Transformations in Nanocrystals*. Advanced Materials, 2009, 21, 4992.

41. C. A. Martin, et al. *A versatile low-temperature setup for the electrical characterization of single-molecule junctions*. Review of Scientific Instruments, 2011, 82(5).

42. ADwin. Available from: http://www.adwin.de.

CHAPTER 3

Back side lithography technique for transmission electron microscopy research

The developments in microfabrication techniques and applications into the specific fields such as in situ TEM studies enables new type of experiments that leads to better quality of high-resolution images of metals, semiconductors or biomaterials. In this Chapter we presented new developed fabrication technique that provide smooth and uniform electron viewing transparent windows at certain locations on a SiN-membrane. This technique is especially applied to MEMS-based heating chips that enable to observe real time changes on materials with respective to temperature effect with an accuracy of less than 1°C degree.

3.1. Introduction

Micro-electro-mechanical system (MEMS) is a technology where mechanical and electronic systems are miniaturized by the techniques of microfabrication. MEMS devices can be simple with stable elements, or can be very complex electromechanical systems with moving elements under the control of integrated microelectronic components. MEMS devices such as micro-sensors and micro-actuators have possible applications in communication [1], medicine and biology [2].

MEMS-based devices are also used in transmission electron microscopy (TEM) studies. In MEMS-based heating holders, the heater is connected to four electrical connections that allow measurement of the resistance for temperature determination and heating. The big advantage of these heaters is that the heat produced is much lower than with the conventional heating holders (about 100 times less) [3]. MEMS-based heaters are presently used for *in situ* TEM studies, such as morphological transformations of gold nanoparticles [4], sculpting of graphene [5], gas nanoreactors [6], thermal stability of nanoparticles [7].

Our MEMS-based heaters and biasing devices are fabricated on a silicon (Si) substrate. In order to obtain an electron transparency we need to realise less than 20 nm-thick amorphous "windows". Mostly we use silicon nitride (SiN) for this purpose, but other materials such as SiO_2, SiC, Al_2O_3 can be also used. The requirement to the SiN windows is that they have to be amorphous, have a uniform thickness and the target thickness of a few nanometres. In our process it is done by etching of thick SiN membranes up to silicon followed by a deposition of thin SiN layer. SiN growth can be controlled with more accuracy than SiN etching. However, this procedure has one big disadvantage: the thin windows are located on the bottom side of the thick SiN membrane (see figure 3.1), meaning that the SiN window is in a deep hole compare to the top surface of the membrane. For example, such deep-hole shaped windows cannot be used for liquid *in situ* experiments. Thus, a local removal of SiN material from the backside is needed. A similar requirement for backside material removal is occurred for biasing *in situ* TEM experiments, in which the thin SiN membrane is only needed at certain locations, for example, where a metal nanobridge is

fabricated and where we would like to remove the SiN locally from underneath the part of nanobridge. In this geometry, the membrane is still strong enough to withstand mechanical forces, such as deformation due to Joule heating of the bridge, whereas the SiN is completely or partially removed below the nanobridge.

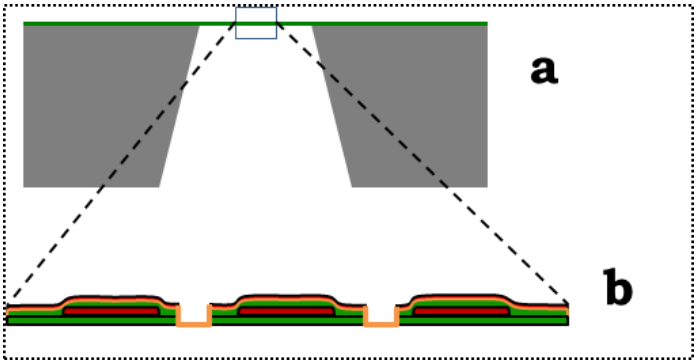

Figure 3.1. (a) Full size of heater chips including the thick and thin SiN membranes and also platinum coils as a heater material, (b) magnified area of the membrane with thin electron transparent viewing windows (orange line, ~20 nm) that are located on the bottom side of the thick SiN membrane.

Performing a backside lithography is impossible with the conventional set-up of lithography system using a mask, since the backside of the membrane is at the bottom of a KOH-etched silicon wafer and 300-500 μm deep hole, whereas the mask should be in the contact with the surface to be patterned and the lens of the electron beam lithography requires at most 100 μm distance to the sample, and can be considered as the focus problem.

In this Chapter we show that one can expose an electron beam resist, which is spray coated on the backside of the SiN window, with an electron beam from the topside of the SiN membrane and, thus, through the SiN membrane and the structure on top of this membrane. In this geometry the focus problem is solved, since both a mask as well as the lens of the EBPG can be brought in close enough distance. Also, we show a possible application of backside lithography in *in situ* TEM experiments.

3.2. Experimental

Fabrication of the MEMS-based heaters consists of different main steps such as deposition, lithography, and dry etching. We start with 300-500 μm thick silicon wafer and deposit 200 nm-thick SiN with low pressure chemical vapour deposition (LPCVD) technique as an isolation layer between the metal and Si substrate. Heaters are made of Tantalum (Ta)/Platinum (Pt) metal layers with thicknesses of ~ 20/180 nm respectively, deposited by electron beam evaporation technique and etched by ion etcher. The second step of LPCVD of SiN is performed and the heater is embedded in a 400 nm-thick SiN. The SiN membrane structures are obtained with KOH-etching of Si. Later, the wafer is diced and cleaned in order to obtain single chips and each of them is cleaned.

Next, electron beam resist (PMMA:PGMEA:MEK) is sprayed on the backside of the chips with an EVG101 spray coater. The main challenge of this spray coating technique is to obtain the uniform resist layer on the backside of SiN membranes due to the depth 300-500 μm of the KOH-etched "hole" in the Si substrate (see figure 3.2). After several spray coating tests, the best uniformity is occurred for 7 layers of spray coated resist with a spin rate of 500 rpm and cured on hot plate at 175°C after each layer of resist coating. This recipe results in a resist with a thickness of approximately 12 μm-PMMA layer .

The pattern is written in a resist from the top site of the chip by exposure of electron beam through the 400 nm-thick SiN membrane with a Leica 5000+ e-beam system. To thin down a SiN membrane at certain locations with high precision, Pt markers are used for alignment with an accuracy of 20 nm. To expose the backside resist from the top of the chip, the dose of electron beam has to be sufficient to write a pattern with designed dimensions through 400 nm-thick SiN layer. To write a pattern we used the dose of 2500 $\mu C/cm^2$ and the beam step size of 100 nm. After resist development the pattern is transferred to the SiN layer using reactive ion etching (RIE) technique in Argon (Ar) and CHF_3-based plasma with anisotropic etching from the backside of the chip. The etching rate and time are critical to obtain a required thickness of the SiN in the thinning down process. During etching process step the SiN thickness is controlled by

color inspection of SiN membrane in optical microscope and comparison with LPCVD SiN color chart. After etching the resist is removed by PRS-3000 (positive resist removal) and oxygen plasma. Described above fabrication steps are a part of the main removal of SiN from the back side. According to application purpose of backside lithography technique, additional fabrication steps might be required. One of the possible *in situ* TEM application is discussed in Application part of this Chapter.

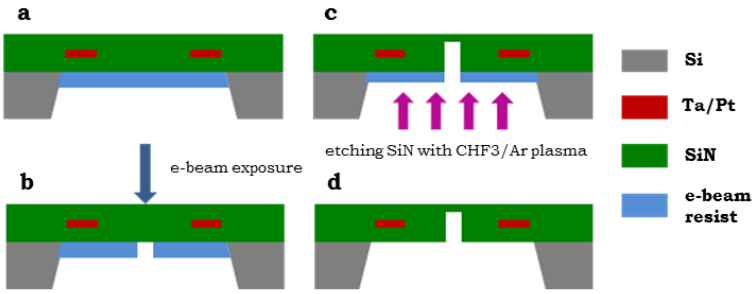

Figure 3.2. Schematic illustration showing the fabrication process of the hole opening from the backside. (a) Spray coating of e-beam resist (PMMA:PGMEA:MEK) from the backside of the chip, (b) e-beam lithography and development, (c) etching of the SiN from the backside by RIE technique to thin it down to requires thickness, (d) after removal of the resist by PRS-3000 (positive resist stripper).

3.3. Applications

In this application example we use the back side lithography technique to fabricate metallic nanobridges with a configuration close to free standing on top of heating chips in order to subsequently shape them into metallic nanoelectrodes separated with a nanogap of several nanometers (1-10 nm) by *in situ* electrical measurements in TEM. The interest to fabrication of these nanogap electrodes on top of heaters is based on the feasibility of performing TEM characterization of nanospecies trapped in between the nanoelectrodes such as low-dimensional nanocrystals, phase change nanoparticles or individual molecules, while applying heating, voltage or both voltage and heating simultaneously. Nanoelectrodes can be fabricated by different techniques, such as mechanical break junction [8],

electron-beam lithography [9], electromigration [10] and shadow mask evaporation technique [11]. In most cases the metal structure is on top of a SiN substrate, and the electrical measurements are not hindered by the substrate. However, for structural characterization of nanogap formation or nanocrystal transformation while applying electrical or heating conditions, TEM is the best technique, but it requires preferably a free-standing metal nanobridge or at most a very thin SiN-substrate that is not thicker than a few nanometers, because a thick support leads to a too noisy background, which does not allow atomic resolution imaging of the gap and species (like molecules or small particles) in the gap. An additional advantage to use heating chips as a base for other following fabrication processes is that it allows to prevent the e-beam-induced carbon contamination while imaging with TEM by heating up to 120-140°C during the *in situ* visualization. Here we present a formation of nanogap electrode using a feedback controlled electromigration (FCE) technique *in situ* TEM in gold nanobridges fabricated onto MEMS-based heaters.

A schematic illustration of MEMS-based heater with a flat 400-nm thick SiN centre is shown in figure 3.3 (a). In order to fabricate thin SiN windows the backside lithography technique was applied as described in Section 3.2 of this Chapter and a pattern of SiN windows with a diameter of 5 μm was produced in the centre of Pt heating coil using e-beam writing through the membrane. After development of e-beam resist the pattern was transferred to SiN layer and RIE was applied from the backside of MEMS-based heaters to thin down this patterned areas of SiN membrane to 50 nm. Schematically it is shown in figure 3.3 (b). Gold bridges with a length of 700 nm, width of 250 nm and 20 nm-thick were produced on top of 50 nm-thick SiN area using e-beam lithography followed by electron beam evaporation from the gold source. Contact pads to bridges were placed by the second step of e-beam lithography followed by the metal evaporation of a 250 nm-thick layer of Au on a 5 nm-thick adhesion layer of Cr. The configuration of fabricated device is schematically presented in figure 3.3 (c). In order to reduce the thickness of SiN in the location of Au nanobridge, SiN was etched from the backside of MEMS-based heater using RIE technique. Since the thickness of SiN under the nanobridge is 50 nm, we used a RIE recipe

with CHF_3 and O_2 gases with a flow ratio of 50 sscm and 2.5 sscm respectively.

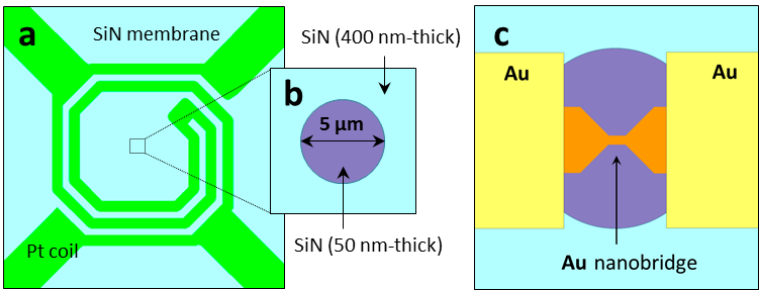

Figure 3.3. (a) Schematic illustration of MEMS-based heater with a flat 400-nm thick SiN centre. Pt heating coil is drawn by green colour and 400 nm-thick SiN is illustrated by blue colour. (b) Central part of the heating coil showing a 50-nm-thick SiN window with 5 µm in diameter illustrated by purple color. (c) The configuration of fabricated device onto 50-nm-thick SiN window containing 20-nm-thick Au nanobridge (orange colour) and 200-nm-thick gold contact pads (yellow color).

The MEMS-based heater with Au nanobridge was placed into built-in-house holder containing six contacts, which allows to combine heating experiments and electrical measurements. Four contacts are usually used to heat the spiral through the heating controller box. Electrical measurements are done by applying voltage to another two contacts. The holder was connected to electrical measurement setup as described in section 2.3.3 of Chapter 2. The heater spiral was calibrated with a pyrometer before heating. The FCE process in Au nanobridges was investigated by *in situ* TEM using a FEI Titan microscope operating at 300 keV. In FCE mode the bridge conductance is constantly monitored while the voltage is ramping up. If there is a sudden decrease in conductance, the FCE mechanism reduces the voltage to zero or to a lower value. The process starts again after a new reference conductance is defined. The program stops when a pre-defined conductance value is reached. To avoid the influence of carbon contamination on bridge resistance forming during illumination by electron beam the

electromigration experiments were performed at T=120°C. It results in zero conductivity value after the bridge breaks.

Figure 3.4 shows snapshots of a typical *in situ* TEM movie recorded during the experiment on the nanogap formation in gold nanobridges by electromigration. The initial view of the bridge before the electrical measurements is shown in figure 3.4 (a). When the current is passed through the bridge, we observe a slight grain growth prior to electromigration. The grain growth is occurring due to the temperature rise in the bridge caused by current-induced Joule-heating. In figure 3.4 (b) the bridge starts to thin close to the cathode side forming a bottleneck. When the electromigration is observed, the current density is about 7×10^7 A/cm^2. To indicate the direction of electrons and, thus, the electrode polarity, the blue arrows are drawn in the images (cathode side (–) and anode side (+)). In the last stage of electromigration a tiny constriction forms as shown in figure 3.4 (c) and the following narrowing is continued at low voltage values which is around 200 mV. As a result, a nanogap electrode is produced (Figure 3.4 (d)). The initial size of the formed nanogap is about 2-3 nm and it increases to 5-6 nm during continuous illumination by the electron beam within several seconds. Figure 3.4 (e) is TEM image acquired at higher magnification and shows the final configuration of the nanogap with the size of 5.26 nm which does not change at least after several minutes of electron beam irradiation. At the moment when the nanogap electrode is initially formed, the tips of the electrodes are sharp. However, after several seconds when the gap size increases, the shape of the tips of electrodes become more smooth which is likely due to surface tension of Au. This observation is in agreement with the previous reports of Zandbergen [12] on continued relaxation of Au nanogaps formed by electron beam bombardment even after the intense irradiation is completed, also with the report of Strachan *et al.* [13] on the evolution of Au nanogap electrodes. A typical I–V curve of FCE process in Au nanobridges is shown in figure 3.4 (f).

As can be seen in figure 3.4 (d), just a very thin layer of SiN remains around the nanogap. According to standard fabrication methods of nanogaps on top of SiN membranes with the thicknesses of 100 nm [14], our technique allows to fabricate nanogap electrodes with very thin SiN

layer beneath it (1-3 nm). These devices can be used for further experiments as synchronous electrical, heating and structural characterization of low-dimensional systems such as nanocrystals and individual molecules.

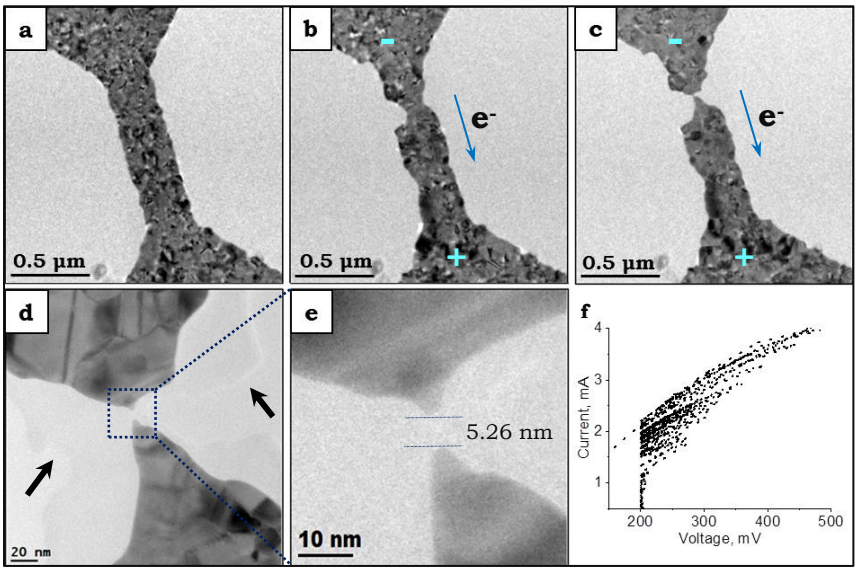

Figure 3.4. Snapshots taken from *in situ* TEM movie recorded during FBC electromigration process in gold nanobridge. (a) The original gold bridge. (b)-(c) TEM images showing formation of nanogap in gold bridge during FBC electromigration. (d) TEM image acquired after bridge breakdown; arrows indicate the areas with a very thin (1-3 nm) SiN layer. (e) Enlarged area of (d) showing gold electrodes separated with 5.26 nm nanogap. (f) A current-voltage curve of FCE electromigration process.

3.4. Discussions and Conclusions

We have shown that it is possible to expose the electron beam resist through a thick membrane in MEMS-base heaters. This opens the manufacturing for a new type of geometry in which one can control the flatness of the top side of the thin film membrane at certain locations. This is important for applications such as electromigration in metals and semiconductors, reducing the noise for DNA translocation experiments

where the SiN windows have to be on top side of the membrane. Therefore, a new fabrication technique is used which is so called back side lithography with exposure from top that enables to obtain thin SiN viewing windows on the top of the membrane and which is presented in the fabrication part of this Chapter. The presented application in this Chapter is one of several frontier projects where we have applied this new fabrication technique. Moreover, having thin SiN electron transparent window on the top of the membrane has advantages for in situ liquid cell studies, environmental studies, battery studies of some materials and etc., since it offers flat surface on the top that enables smooth liquid flow for liquid cell studies and controllable lift off materials after deposition. Compared to light optical lithography, electron beam lithography allows one to obtain smaller structures with a high accuracy of the required dimensions. The back side lithography fabrication and its application in the nanogap electrode formation in gold by FCE electromigration technique are promising evidence for the future possible applications.

References

1. M. C. Wu, A. Solgaard and J. E. Ford. *Optical MEMS for lightwave communication*. Journal of Lightwave Technology, 2006, 24(12), 4433-4454.

2. J. Voldman, M. L. Gray, and M. A. Schmidt. *Microfabrication in biology and medicine*. Annual Review of Biomedical Engineering, 1999, 1, 401-425.

3. F. D. Tichelaar, M. A. van Huis and H. W. Zandbergen. *Transmission Electron Microscopy as Nanolab*, in Handbook of Nanoscopy. 2012, Wiley-VCH Verlag GmbH & Co. KGaA, 345-374.

4. N. P. Young, et al. *Transformations of gold nanoparticles investigated using variable temperature high-resolution transmission electron microscopy*. Ultramicroscopy, 2010, 110(5), 506-516.

5. B. Song, et al. *Atomic-Scale Electron-Beam Sculpting of Near-Defect-Free Graphene Nanostructures*. Nano Letters, 2011, 11(6), 2247-2250.

6. S. Malladi, et al. *Localised corrosion in aluminium alloy 2024-T3 using in situ TEM.* Chemical Communications, 2013, 49(92), 10859-10861.

7. A. O. Yalcin, et al. *Core-shell reconfiguration through thermal annealing in $Fe_xO/CoFe_2O_4$ ordered 2D nanocrystal arrays.* Nanotechnology, 2014, 25(5).

8. M. A. Reed, C. Zhou, C. J. Muller, T. P. Burgin, J. M. Tour. *Conductance of a Molecular Junction.* Science 1997, 278, 252.

9. W. Chen, H. Ahmed, K. Nakazoto. *Coulomb blockade at 77 K in nanoscale metallic islands in a lateral nanostructure.* Appl. Phys. Lett., 1995, 66, 3383.

10. J. Park, A. N. Pasupathy, J. I. Goldsmith, C. Chang, Y. Yaish, J. R. Petta, M. Rinkoski, J. P. Sethna, H. D. Abru na, P. L. McEuen, D. C. Ralph. *Coulomb blockade and the Kondo effect in single-atom transistors*. Nature, 2002, 417, 722.

11. S. Kubatkin, A. Danilov, M. Hjort, J. Cornil, J. L. Bredas, N. Stuhr-Hansen,P. Hedegard, T. Bjornholm. *Single-electron transistor of a single organic molecule with access to several redox states*. Nature, 2003, 425, 698.

12. H. W. Zandbergen, R. J. H. A. van Duuren, P. F. A. Alkemade, G. Lientschnig, O. Vasquez, C. Dekker, F. D. Tichelaar. *Sculpting Nanoelectrodes with a Transmission Electron Beam for Electrical and Geometrical Characterization of Nanoparticles.* Nano Lett., 2005, 5 (3), 549–553.

13. D. R. Strachan, D. E. Smith, M. D. Fischbein, D. E. Johnston, B. S. Guiton, M. Drndic´, D. A. Bonnell, A. T. Johnson. *Clean Electromigrated Nanogaps Imaged by Transmission Electron Microscopy*. Nano Lett., 2006, 6 (3), 441–444.

14. M. Rudneva, B. Gao, F. Prins, Q. Xu, H. S. J. van der Zant, H. W. Zandbergen. *In Situ Transmission Electron Microscopy Imaging of Electromigration in Platinum Nanowires.* Microscopy and Microanalysis, 2013, 19, 43-48.

Chapter 4

In situ electrical characterization of tapered InAs nanowires in a transmission electron microscope with ohmic contacts

4.1. Introduction

Semiconductor nanowires (NWs) have attracted much interest due to their outstanding properties as building blocks in nanoelectronic devices [1–3]. InAs NWs with a relatively small band gap and a high electron mobility are considered very interesting for high performance electronic devices. Obviously, high stability of these NWs is required if they are to be used. Electrical characterizations of NWs have been made mostly by making metallic contacts in a top-down approach [4–6] and sometimes by in situ TEM making contact on one side of the NWs with an STM tip [4, 7–12]. Several mechanisms are reported for the onset of the breakdown due to a high current: compositional changes or decomposition due to heating, and electromigration. A limitation of the electrical measurements using an STM tip to make contact to one side of the NW is that the quality of the electrical contact with the NW is not known and often not ohmic. This can lead to wrong values for the I–V properties [13] and strong heating of the NW close to this contact.

In this chapter we present an *in situ* TEM investigation of the electrical properties as well as breakdown of tapered InAs NWs using a homemade *in situ* TEM holder and samples with good ohmic contacts between the NW and the electrodes. The electrical resistivity is constant $\sim 10^{-2}$ Ω·cm for NWs with diameters larger than 120 nm. The breakdown was found to arise from the combined effect of electric field and Joule heating.

4.2. Method

Tapered InAs NWs were fabricated on an InP substrate using a metalorganic vapour phase epitaxy method. Details are given in [5] and [14]. These NWs were mounted on a special MEMS device used for the *in situ* TEM measurements combining TEM with electrical measurements, see figures 4.1 (a) and (b). The MEMS device contains electrodes deposited on a silicon nitride membrane with a 5 nm Cr layer for adhesion. The 95 nm thick Au electrodes have a width of 1 μm and spacings of 4 μm. For unobstructed TEM

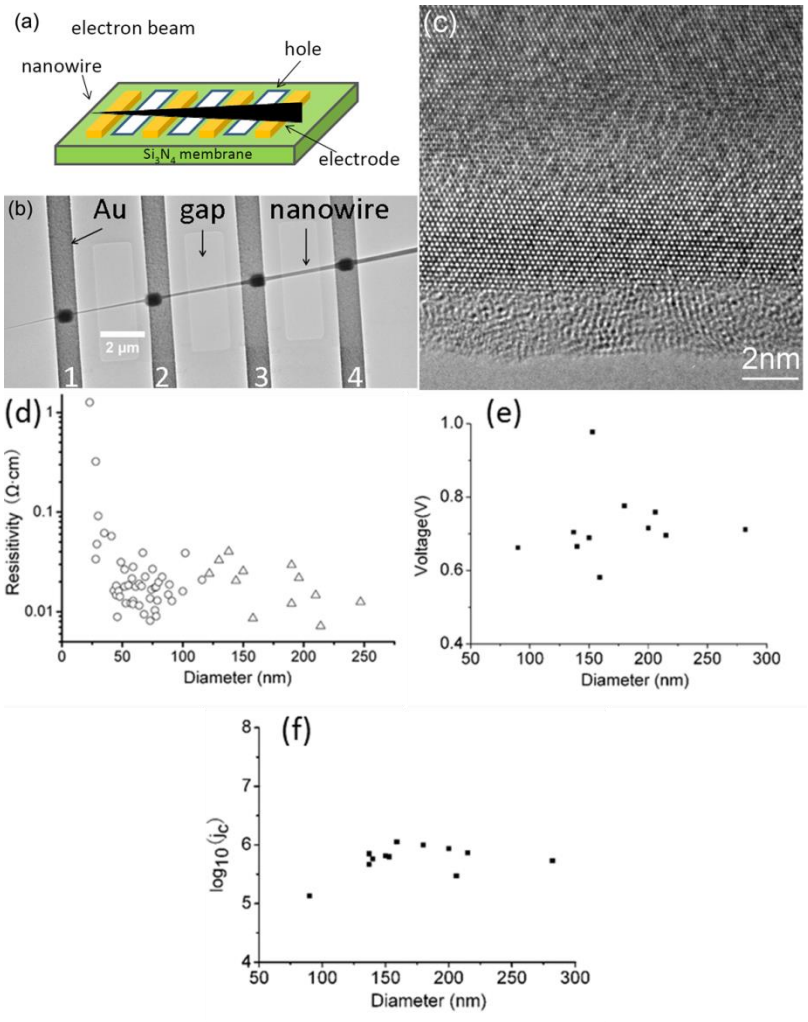

Figure 4.1. (a) Scheme of chip for *in situ* electrical measurements. A tapered NW is connected to four electrodes on a SiN membrane. Slits are made in the membrane, allowing unobstructed TEM imaging of the NWs suspended over these slits. (b) Bright field TEM image of NW with Pt contacts as black areas. (c) HRTEM image showing the ~2 nm oxidation layer. (d) Electrical resistivity data with different diameters (Δ-this paper, o-literature [5]). (e) Plot of the critical voltage for the start of breakdown versus diameter. (f) Plot of $\log_{10}(j_c)$ versus diameter, where j_c is the critical current density for breakdown in the scale of $A \cdot cm^{-2}$.

imaging, 1.5 µm ×5µm gaps were created in the SiN between the Au electrodes using a FIB (FEI DualBeam Strata DB235). A relatively large gap length was applied to ensure that no stray currents can flow through e-beam induced contamination on the SiN. Next, a single tapered NW was selected and transferred onto the silicon nitride membrane using an ex situ nano-manipulator. Finally, platinum was deposited with a FIB on top of the joint of the NW and the electrodes for a good electrical contact quality. Most NW segments contacted in this manner were thicker than 120 nm. In cases where they were smaller we noticed significant degradation of the InAs NW by the focussed ion beam. Therefore, only NWs with a diameter larger than 120 nm were investigated. The *in situ* electrical measurements were carried out in an aberration corrected FEI Titan TEM operated at 300 kV. Figure 1(c) shows a high-resolution image of InAs NW, which is consistent with the zinc blende structure. One can see that a 2 nm thick mainly amorphous phase of uniform thickness is present on the surface. EDX analysis on this phase showed it is an indium oxide.

4.3. Results

A two-terminal measurement was used to characterize the contacts between the NW and the electrodes. The resistance of the contacts have to be known because the current-voltage measurements depend strongly on the contact quality between the NWs and electrodes [13, 15, 16]. For the contact characterization we applied a small voltage with a maximum of 100 mV in order to prevent significant Joule heating. Some typical I–V curves between different terminals are shown in figure 4.2 (a). All I–V plots are linear at low voltages. This indicates that the contacts between the electrodes and the NWs are ohmic. Electrical measurements have been done while switching on and off the electron beam at an accelerating voltage of 300 kV and 80 kV; no significant changes were observed in the resistivity, indicating that an electron beam effect can be ignored. The slope of I–V curve decreases with decreasing diameter of the NW, i.e., the resistance increases with decreasing diameter.

The contact resistances can be calculated using the I–V measurements over the sections between, for instance, the contacts 1–2, 2–3 and 1–3 and, thus, the net resistances of the sections between the contacts can be determined (see supplementary material (SM)). Note that for the measurement between the contacts 1–3 the current at the contact 2 will flow mainly though the Pt–C dot since it has a much higher conductivity than InAs (see SM). The as-measured and contact resistance-corrected resistances for several NWs differ only slightly (see figure 4.2 (b)) showing that the contact resistances are at most 6% of the net resistances and, therefore, we use in this paper the non-corrected resistances to discuss the trends. The electrical resistivity of the NWs is almost constant around 10^{-2} Ω·cm (see triangles in figure 4.1 (d)), in agreement with top-down measurements [5] (indicated by circles in figure 4.1 (d)). It should be noted that under different growth conditions the resistivity may change quite a lot. However, the NWs used in our experiments are taken from the batch of tapered InAs NWs as used for [5].

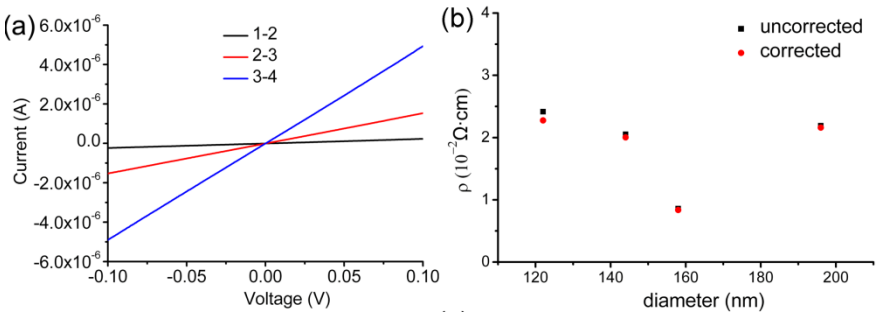

Figure 4.2. (a) Two terminal I–V curves between each neighbouring electrode pairs as shown in figure 4.1 (b), showing good ohmic contacts with the electrodes; (b) corrected and uncorrected resistivity, the contact resistivity is within 6% of the measured resistance.

For voltages higher than 100 mV the I–V plot is no longer linear and if further increased the NW will eventually break. A typical NW section after breakdown (out of 8 breakdowns observed, see figure 4.4) is shown in figure 4.3 (a). Whereas the NW breaks down, the oxide surface layer remains. The breakdown area was always observed to be close to the cathode side.

Furthermore, round particles are formed near the anode side. EDX mapping (see figures 4.3 (b)–(d)) shows that these particles are very indium rich, while the nanocrystals existing in the broken part (figure 4.3 (e)) are rich in arsenic (see figures 4.3 (f)-(h)). The indium balls are located near the surface of the NW (see figure S1 in supplemental materials). The EDX measurements of the In-balls show the presence of oxygen in and/or on these balls, which we attribute to a reaction of indium with air during transport between TEMs.

To follow the breakdown process in detail, *in situ* TEM videos were recorded while making in parallel electrical measurements. We started the breakdown study by using a gradual voltage increase with a ramp rate of 1 $mV \cdot s^{-1}$ and when the breakdown was observed to start, in most cases the voltage was kept constant to slow down the breakdown process allowing detailed recording of the microstructural evolution.

The breakdown mechanism is likely to be the following. Current induced Joule heating leads to local decomposition of InAs at the surface (the NW becomes thinner), whereby As sublimates and In-atoms move away from the hot area by the electric field. At the final part of the breakdown there is also a quick drop in the temperature resulting in local patches of In and InAs.

Figures 4.4 (a)–(c) shows I, V and the conductance G versus time and I–V curves of one NW breaking experiment. In general, there are three stages in the breaking process. In the first stage (CD, from 0 to 0.3−0.5 V), G increases linearly; in the second stage (DEF, from 0.3−0.5 V to ~0.7 V) G starts to increase more rapidly but no visual change occurs in the NW (except for some changes in bending contours) and in the third stage at ~0.7 V (FGH) the breakdown of the NW occurs. The start of this breakdown is visible first by the formation of sphere-like In-particles near the anode side. These particles grow and at the same time at another location which closer to the cathode side a small section of the NW starts to thin down. Once this thinning

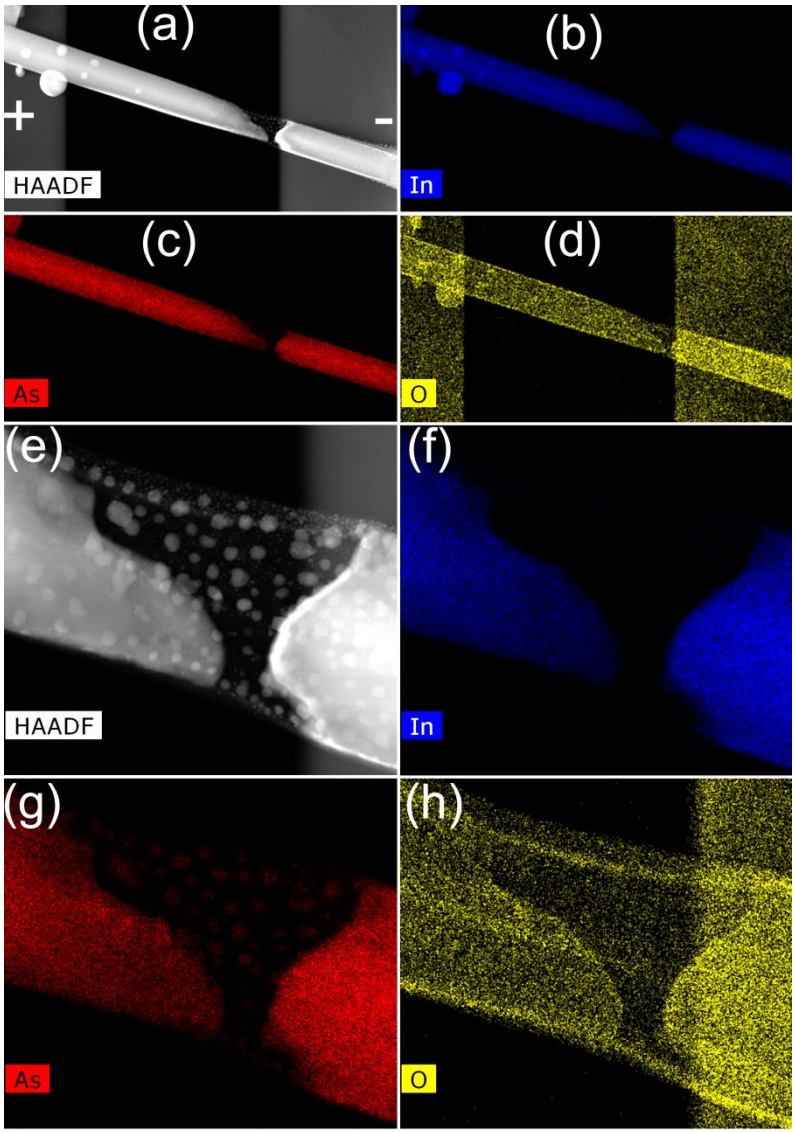

Figure 4.3. (a) HAADF image of one InAs NW after breakdown, particles were found close to the anode, while the breakdown happened in a position close to the cathode. (b)–(d) EDX maps of the NW, which shows clearly the particles close to the anode are rich in indium and oxygen. (e) HAADF image of InAs NW in the place of breakdown. (f)-(h) EDX maps showing that nanocrystals existing in the broken part are rich in arsenic.

down is quite obvious in the images G decreases rapidly. During the thinning down of the section of the NW, the spherical shaped particles grow in size and sometimes in number. From point C to point E (figures 4(d)–(f)) no changes can be observed. From point E, G starts to deviate significantly from a linear increase, but still no changes are visible in the movie from points E–F. At point F we observed the first change in the image: a small sphere was formed (indicated by a red arrow in figure 4.4 (g)) on the anode side. Because of this observation the voltage was kept constant. During the breakdown process that followed, the spherical particle grows in size and another one is formed, and a slight thinning down of a section of the NW on the cathode side can be observed. Also a slight decrease in the conductance is measured between point F and G (see figure 4.4 (b)). Based on the formation time and volume of indium balls from recorded movie and taking as time scale 0.1 s, which is the minimum exposure time to image an atom with sufficient contrast, about 105 indium atoms move from the broken part to the anode in one image. This movement cannot be imaged with HREM. In the next stage, which starts roughly at point G (figure 4.4 (h)) the thinner part of the wire is rapidly decreasing in width (from point G to point H in figure 4.4). The rapid decrease in diameter is associated with a rapid decrease of the electrical conductance. At point H the NW is almost broken. At this point the surface oxide layer is still present as is shown in figure 4.4. In the next stage there is still a finite conductance and the current only dropped to zero if the applied voltage was increased to 1.13 V. We assume that this last finite conductance is due to conductance through the oxide skin of the NW. We did not see a significant carbon contamination built up on the shell of the NW in our experiments. Moreover, if there would be a significant carbon contamination on the InAs NW there should be a relatively low resistance after the InAs NW is broken since the shell of the NW does not break. We observe in our experiments that the resistance increases sharply to MΩ range as soon as the NW breaks.

Apart from the typical NW breaking process demonstrated in figure 4.4 sometimes a deviating behaviour of conductance was observed (see figure S2 in SM). A detailed analysis of this movie is given in the SM. The breaking process is similar, occurring also at a voltage of ~0.70 V. The non-typical behaviour is in the response in G upon the change in the voltage: in this

experiment the voltage was kept constant at 0.64 V for a while, whereby G was increasing quite rapidly. In order to track the starting position of the breakdown, low-magnification videos were recorded. After breakdown HREM images of the broken part were acquired and shown in figure 4.5. Figure 4.5 (a) shows a low-resolution image as used to follow the breakdown process. Figure 4.5 (b) shows an image of the whole breakdown area, while figures 4.5 (c) and (d) are HREM images of the squared areas in (b). Figures 4.5 (e)–(h) are Fast Fourier transforms (FFT) of the areas labelled 1–4 in figures 4.5 (c) and (d). The FFT patterns (figures 4.5 (e) and (f)) taken from the areas 1 and 2 are similar and present the same zinc blende structure. FFT pattern 4.5 (g) can be indexed as ⟨110⟩ oriented InAs and 4.5 (h) as ⟨110⟩ oriented tetragonal indium.

Figure 4.6 shows eight TEM images of broken NWs, illustrating the reproducibility and the variation in deposition of the In-balls and the breakdown area. In all cases In-balls occur close to the anode side, although the distance to the anode varies. For figures 4.6 (a)–(c) the SiN was not removed as was done for figures 4.6 (d)–(g). The breakdowns happen near the cathode side except in only the one case shown in figure 4.6 (h) where the breakdown is in the middle and which is clearly an exception. The critical breakdown voltage for InAs NWs is around 0.6–1.0 V and there is no obvious dependence between the critical breakdown voltage and the NW diameter in the range 100–300 nm (see figure 4.1 (e)).

The origin of the In-balls must be the breakdown area because almost simultaneous narrowing of this area is observed. There are two options for the driving forces to form the In-balls (here we assume that the skin of the NW is not conductive, since after breaking of the InAs the resistance becomes very high). In case the In-atoms move out to the surface close to their origin the force acting on them must be the electric field (the so-called direct force in electromigration). In case the In-atoms travel near the surface between the oxide shell and the NW, the force is the wind force (the impulse transfer from the charge carrier). More research is needed to determine this.

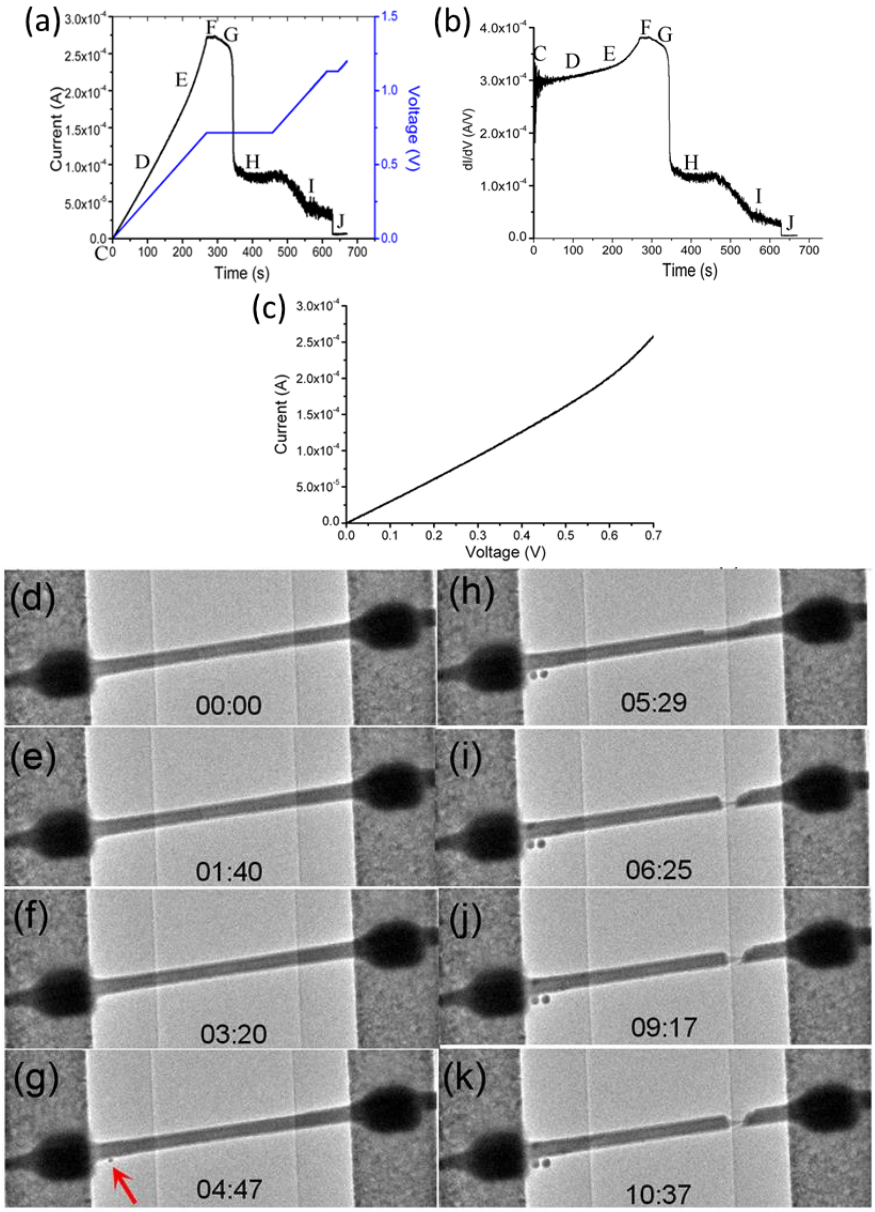

Figure 4.4. (a)–(c) I–V curves versus time of InAs nanowires during the whole process, (d)–(k) shows the corresponding TEM images at some typical points indicated in (a) and (b) by capitals corresponding to the figure numbering. The distance between the Au electrodes is 4 μm.

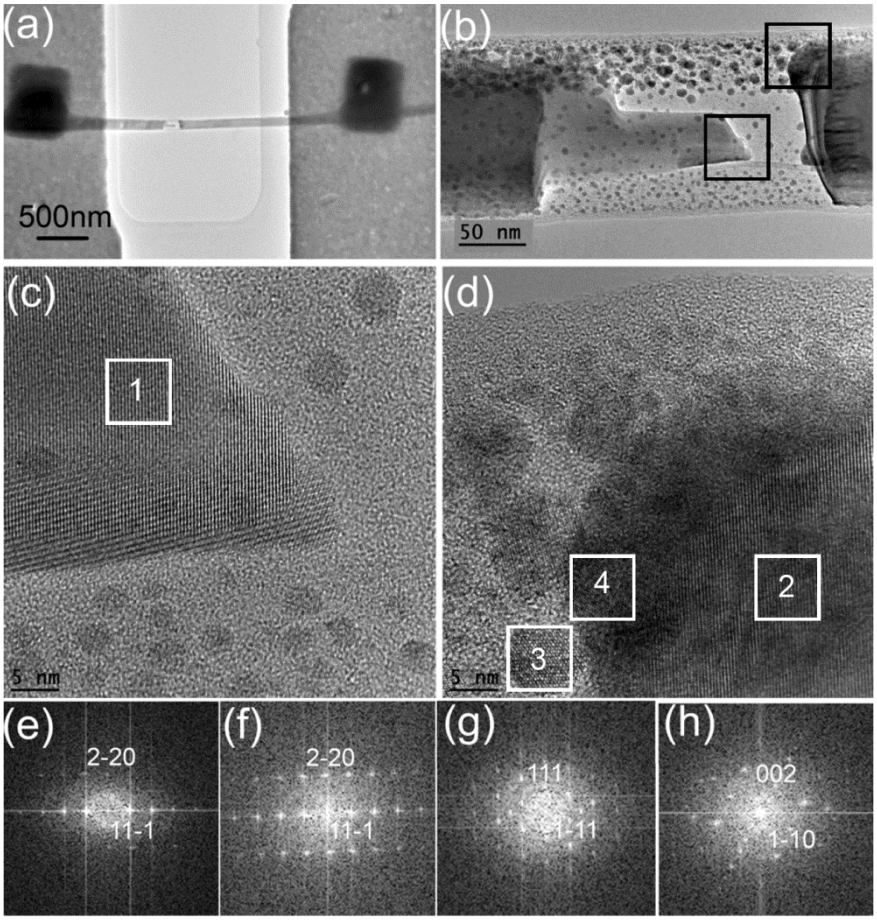

Figure 4.5. (a) Low magnification image of tapered InAs nanowire after breakdown; (b) magnified image of the broken area; (c) and (d) correspond to HREM images of the left and right squared area in (b); (e)-(h) corresponds to the FFT patterns of areas 1–4 indicated in (c) and (d).

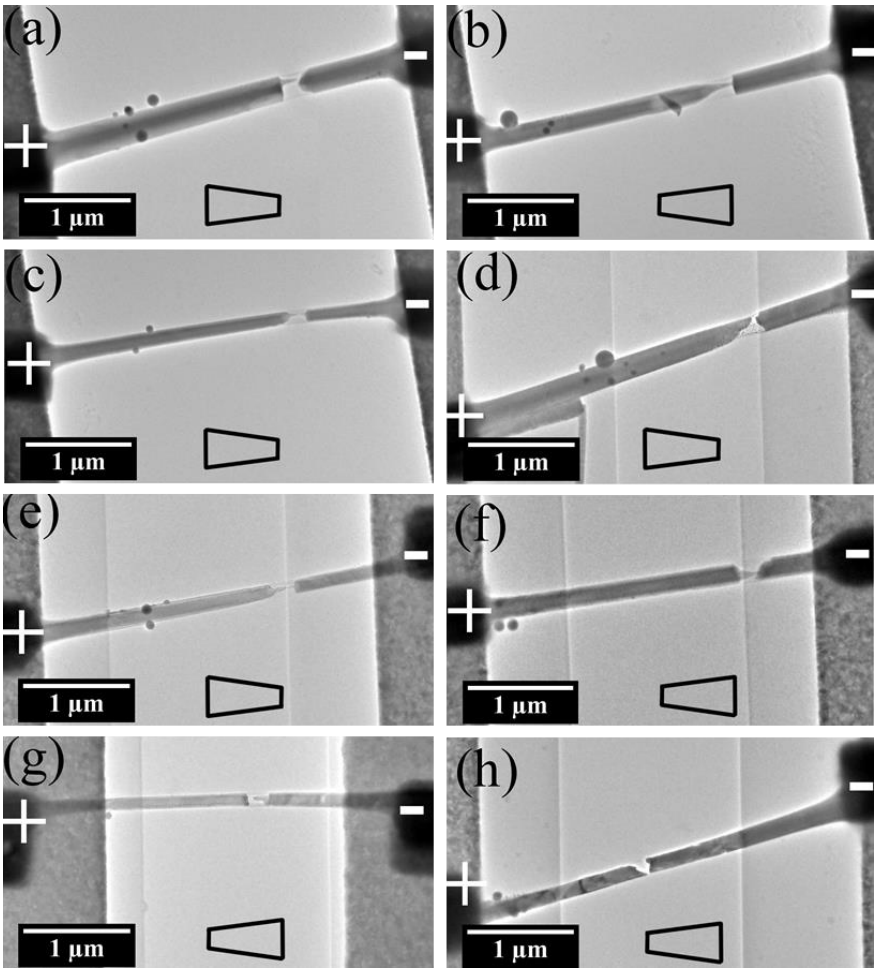

Figure 4.6. Bright field TEM images of InAs NWs after breakdown showing the similar behaviour. The +/– represents anode/cathode, while trapezoid indicates the tapering direction of each nanowire. For (a)–(c) the SiN membrane is continuous under the nanowires while for (d)–(h) part of SiN membrane is removed by FIB. For (a)–(h) indium balls are present. For (a)–(f) the breakdown occurs relatively close to the cathode, (h) the breakdown occurs almost in the middle.

4.4. Discussion

When an electrical current is applied to a NW, Joule heating is unavoidable. With the increase in temperature, the carrier concentration in an intrinsic semiconductor also increases and thus the conductance will increase. Indeed we see an increase in the conductance, for instance in figure 4.4 (b). The observed increase can—however—not be fitted with a simple picture of the increase in the carrier concentration, since it is not exponential. The conductance increase can result in a self-acceleration of the heating, since the increase in charge carriers results in more scattering, which results in a further temperature increase, which generates more charge carriers and so on. This 'reaction chain' could be the reason for the large increase in G even when the voltage was kept constant. To check this last possibility we used the focus of the TEM to determine bending of the SiN membrane for one case, and measured a height difference of the SiN near the Au electrode and at the edge of 60 nm. Thus, a contact of the edge of the SiN near a hole created by FIB with the InAs NW cannot be excluded (see also SM).

The breakdown of the NW does not occur in the middle of the wire as can be seen from figure 4.4. Intuitively one would expect that the NW is hottest in the centre, given the two equal heat sinks of the Au electrodes (the tapered shape might lead to some deviation). Still we do not see the breakdown in the centre of the NW but much closer to the cathode. There is some variation in the exact position but the trend is always the same, irrespective of the tapering direction. In electromigration experiments of Pt and Pd NWs it was observed [17] a similar behaviour and also documented that the temperature is not the hottest in the centre, based on the local start of a recrystallization. We assume that such an asymmetrical location of the breakdown area is due to Thompson effect [18]. Similar asymmetrical breakdown is observed by Kang et al [19] for In_2Se_3 NWs and explained to be due to Thompson effect.

We have carried out in situ TEM heating experiment of InAs NWs and observed that decomposition starts at about 500°C, which is in agreement with a report of Hertenberger *et al* [20]. In the presence of a current the local

temperature needed for the breakdown can be substantially less because electromigration can remove atoms well below the sublimation temperature. The formation of In-balls far away from the decomposition area accompanied with a thinning of a section of the NW indicates that electromigration indeed occurs. The partial removal of In will result in a chemically less stable composition which will trigger easier electromigration and sublimation of As. Alternatively, sublimation of As will make the InAs more In rich facilitating the electromigration of In.

The critical current density j_c for the breakdown of the NWs with different diameters was calculated based on the formula: $j_c = I_p/S$, where I_p is the peak value of the I–V curve where breakdown starts, and S is the cross section area of the NW. The critical current densities for the NWs with diameters from 120 nm to 280 nm are ranged from $10^{5.5}$–$10^{6.5}$ A·cm^{-2}, (see figure 4.1 (f)) whereby mostly the critical current density is close to 10^6 A·cm^{-2}, which is within the range of electrical migration of dislocations (~10^5 A·cm^{-2}), surface (~10^6 A·cm^{-2}) and point defects (~10^7 A·cm^{-2}) [21], which is similar to results of Dayeh *et al* on ex situ I–V measurements, showing that an InAs NW with a diameter of 33 nm breaks at a current density of 10^7 A·cm^{-2}. From post-mortem TEM analysis they concluded that the breakdown arises from the arsenic out-diffusion [6].

Several *in situ* TEM studies with a TEM-STM setup are reported for NWs of InAs, GaN, BN and ZnTe, whereby the critical breakdown voltage ranged from 2–100 V, while the critical current ranged from 10^4–10^6 A·cm^{-2}. The applied voltage is much higher than that in our case (~1 V), which we contribute to the high contact resistance between the NW and STM tip, which for instance can result in a breakdown at a position very close to the STM tip due to extreme Joule heating at the STM-NW contact (such as in [4]). Although the voltages, positions of breakdown and electromigration effects can be very different for *in situ* TEM studies with a TEM-STM setup compared to those of our set-up or conventional (non-*in situ*) measurements, the breakdown mechanism is likely to be similar. Indeed several authors report the formation of balls (Ga, B, Zn and Te) [4, 6, 8, 9].

4.5. Conclusions

In conclusion, we succeeded in fabricating low ohmic contacts to the InAs NWs, thereby excluding an experimental setup artefact (Joule heating as a result of high resistance contacts). We could record changes with TEM observation while simultaneously recording the I–V properties. Furthermore, we also observed the growth of often reported material balls on top of the NW during the breakage process, and we suggested a mechanism based on electromigration of In leading the In ball growth on the anode side and the NW breakage near the cathode side.

References

1. W. Lu and C.M. Lieber. *Semiconductor nanowires*. J. Phys. D: Appl. Phys., 2006, 39(21), R387.

2. S. Meister, D. T. Schoen, M. A. Topinka, A. M. Minor and Y. Cui. *Void Formation Induced Electrical Switching in Phase-Change Nanowires*. Nano Lett., 2008, 8 (12), 4562.

3. S. W. Nam, H. S. Chung, Y. C. Lo, L. Qi, J. Li, Y. Lu, A. C. Johnson, Y. Jung, P. Nukala, R. Agarwal. *Electrical wind force-driven and dislocation-templated amorphization in phase-change nanowires*. Science, 2012, 336, 1561–1666.

4. T. Westover, R. Jones, J. Huang, G. Wang, E. Lai, A. A. Talin. *Photoluminescence, Thermal Transport, and Breakdown in Joule-Heated GaN Nanowires*. Nano Lett., 2008, 9(1), 257–263.

5. M. Scheffler, S. Nadj-Perge, L. P. Kouwenhoven, M. T. Borgstrom, E. P. Bakkers. *Diameter-dependent conductance of InAs nanowires*. J. Appl. Phys., 2009, 106, 124303.

6. S. A. Dayeh, D. Susac, K. L. Kavanagh, E. T. Yu, D. Wang. *Field Dependent Transport Properties in InAs Nanowire Field Effect Transistors*. Nano Lett., 2008, 8(10), 3114-3119.

7. J. Zhao, H. Sun, S. Dai, Y. Wang, J. Zhu. *Electrical breakdown of nanowires*. Nano Lett., 2011, 11(11), 4647–4651.

8. Z. Xu, D. Golberg, Y. Bando. *In Situ TEM-STM Recorded Kinetics of Boron Nitride Nanotube Failure under Current Flow*. Nano Lett., 2009, 9(6), 2251–2254.

9. K. Davami, H. M. Ghassemi, R. S. Yassar, J. S. Lee, M. Meyyappan. *Thermal Breakdown of ZnTe Nanowires*. ChemPhysChem, 2012, 13, 347–352.

10. K. Davami, H. M. Ghassemi, R. S. Yassar, J. S. Lee, M. Meyyappan. *In-Situ TEM Monitoring of Thermal Decomposition in CdTe and ZnTe Nanowires*. Microsc. Microanal., 2011, 17, 1874-1875.

11. Q. Zhang, J. Qi, Y. Yang, Y. Huang, X. Li, Y. Zhang. *Electrical breakdown of ZnO nanowires in metal-semiconductor-metal structure*. Appl. Phys. Lett., 2010, 96, 253112.

12. T. T. Xu, X. Wei, J. Shu, Q. Chen. *Transmission electron microscopy assisted in situ joule heat dissipation study of individual InAs nanowires.* Appl. Phys. Lett., 2013, 103, 193112.

13. Z. Y. Zhang, K. Yao, Y. Liu, C. H. Jin, X. L. Liang, Q. Chen, L. M. Peng. *Quantitative analysis of current-voltage characteristics of semiconducting nanowires: decoupling of contact effects.* Adv. Funct. Mater., 2007, 17, 2478–2489.

14. J. A. van Dam, Y. V. Nazarov, E. P. A. M. Bakkers, S. De Franceschi, L. P. Kouwenhoven. *Supercurrent reversal in quantum dots*. Nature, 2006, 442, 667.

15. Z. Y. Zhang, C. H. Jin, X. L. Liang, Q. Chen, L. M. Peng. *Current-voltage characteristics and parameter retrieval of semiconducting nanowires*. Appl. Phys. Lett., 2006, 88, 073102.

16. F. Leonard, A. Talin. *Electrical contacts to one- and two-dimensional nanomaterials*. Nat. Nanotechnology, 2011, 6, 773–783.

17. T. Kozlova, M. Rudneva, H. W. Zandbergen. *In situ TEM and STEM studies of reversible electromigration in thin palladium–platinum bridges*. Nanotechnology, 2013, 24, 505708.

18. D. T. Castro, L. Goux, G. A. M. Hurkx, et al. *Evidence of the thermo-electric Thomson effect and influence on the program conditions and cell optimization in phase-change memory cells.* Electron devices meeting IEDM, IEEE International, 2007, 315–318.

19. D. Kang, T. Rim, C.-K. Baek, M. Meyyappan, J.-S. Lee. *Investigation of electromigration in In2Se3 nanowire for phase change memory devices*. Appl. Phys. Lett., 2013, 103, 233504.

20. S. Hertenberger, D. Rudolph, J. Becker, et al. *Rate-limiting mechanisms in high-temperature growth of catalyst-free InAs nanowires with large thermal stability*. Nanotechnology, 2012, 23, 235602.

21. J. Zhao, PhD Thesis Tsinghua University, Beijing, 2012.

Supplementary material

1. Calculation of contact resistances and correction for the resistances of the nanowires.

For the nanowire with four electrodes, the measured resistance between electrodes i and j R_{i-j} is the sum of the contact resistance with i, j (R_i, R_j) and the corrected resistance R_{ij} of the nanowire between electrodes i and j. The equations are shown as following:

$$R_{1-2}=R_1+R_2+R_{12} \quad (1)$$

$$R_{2-3}=R_2+R_3+R_{23} \quad (2)$$

$$R_{3-4}=R_3+R_4+R_{34} \quad (3)$$

$$R_{1-3}=R_1+R_3+R_{12}+R_{23} \quad (4)$$

$$R_{2-4}=R_2+R_4+R_{23}+R_{34} \quad (5)$$

Therefore, the contact resistance with the electrodes and the corrected resistance are determined by the following equation:

$$R_2=1/2*(R_{1-2}+R_{2-3}-R_{1-3}) \quad (6)$$

$$R_3=1/2*(R_{2-3}+R_{3-4}-R_{2-4}) \quad (7)$$

$$R_{23}=1/2*(R_{1-3}+R_{2-4}-R_{1-2}-R_{3-4}) \quad (8)$$

Thus, the resistance of the middle part R_{23} can be corrected by subtracting the contact resistances R_2 and R_3.

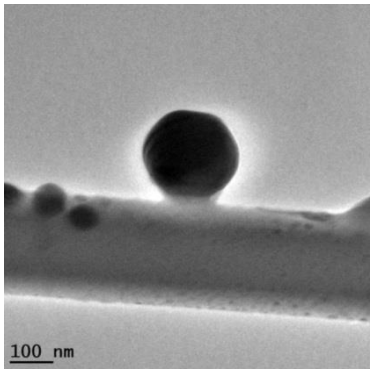

Figure S1. A In particle on top of the InAs nanowire.

2. Deviating conductance behaviour during the breaking process in some InAs nanowire

Figure S2 shows a deviating behaviour during current passage. In figure S2 is can be seen that when the voltage was kept constant (0.6 V) for the first time *G* showed a slow increase (DE). However, when after a voltage increase to 0.64 V the voltage was kept constant (F), the conductance increases strongly at first and next remains almost constant (GH). With a further linear increase of the voltage to 0.71 V, *G* increases again (HI). Up to this stage no obvious changes of the nanowire are observed. Then at 0.71 V an In ball is formed close to the anode, which indicates the start of the breakdown. Keeping the voltage at 0.71 V, *G* decreases rapidly, associated with a rapid decrease in width of the breakdown area of the nanowire. The current dropped to zero when the voltage was increased to 1 V.

Remarkable in the experiment shown in figure S2 is that after the fast increase in *G* with constant V, *G* suddenly remains more or less constant, which suggests that the temperature and the carrier concentration have reached stable values. We do observe contrast changes in the nanowire due to bending. The location of the sudden contrast change is close to the position of the edge of the SiN_x, suggesting that the change in G is might to a contact between the SiN_x and the NW, resulting in a new heat conducting path. The time at which the sudden change in bending contrast occurs is close to point G in the conductance plot, indicating that the change in bending and/or the contact with the SiN_x changes the conductance behaviour of the nanowire. Further research is needed to confirm this. Since the InAs nanowire is on both sides on top of 100 nm thick electrodes and is suspended over a distance of about 3 μm, it cannot bend so much that it touches the SiN_x, but the edge of the SiN_x could bend towards the InAs wire. To check this last possibility we used the focus of the TEM to determine bending of the SiN_x membrane for one case, and measured a height difference of the SiN_x near the Au electrode and at the edge of 60 nm. Thus a contact of the edge of the SiN_x near a hole created by FIB with the InAs nanowire cannot be excluded.

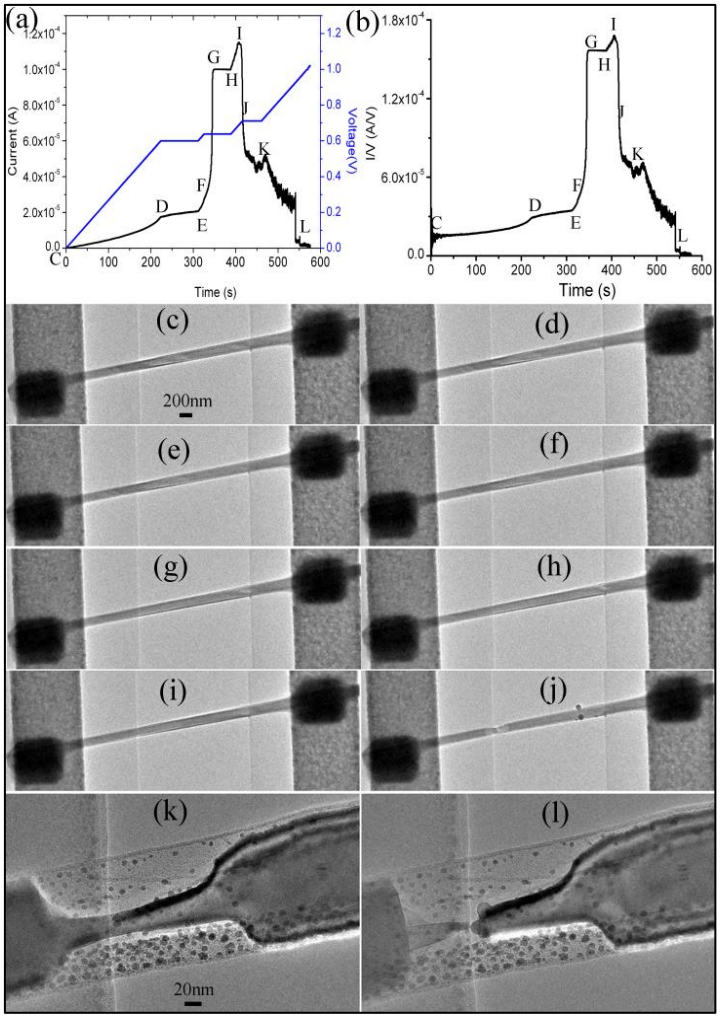

Figure S2. (a)-(b) I-V and I/V curves of InAs nanowires during the whole process, (c)-(l) show the corresponding TEM images at some typical points indicated in (a) and (b). (For more information, please refer to the video.)

CHAPTER 5

In situ TEM investigations of controlled electrical breakdowns in InAs nanowires

5.1. Introduction

Much research attention has been paid to semiconductor nanowires (NWs) over the past decade due to their promising applications in nanoelectronic devices including nanoscale circuits, sensors, interconnections, memory, transistors [1, 2]. Certainly, the stability of such NWs under an electrical load is a key issue when the NWs serve as the most important components of electronic devices. The high current density can lead to an electrical breakdown of semiconductor NWs. The main reasons breakdown are considered to be electromigration-induced damage and decomposition due to Joule heating.

In the case of electromigration processes, the high-density electric current flowing through a solid can lead to an atomic flow due to the high-speed electrons transfer a portion of their momentum to the atoms (or ions) by collision. As a result, this phenomenon can lead to morphological and structural instabilities due to the mass diffusion. At the same time, high currents sent through semiconductor NWs raise their temperature due to Joule heating. As the thermal conductivity of semiconductor NWs is much lower than that of metal NWs, the increase of temperature in semiconductor NWs is higher, which can lead to a thermal decomposition or breakdown.

Experimental investigations of breakdowns of GaN, $TiSi_2$, InAs, ZnO, TiO_2, SnO_2 NWs and of BN and C nanotubes have been performed to understand the nature of electrical breakdowns. Nie *et al.* [3] studied the electrical failures of semiconductor oxide nanowires (NWs) *in situ* inside a transmission electron microscope (TEM). They performed electrical measurements *in situ* using a tungsten tip positioned by a piezo-actuator and used as a manipulator and the first electrode. For the second electrode they adhered the NW samples to the flat end of the counter Au electrode. They observed different electrical failure behaviors of SnO_2 and TiO_2 semiconductor oxide NWs. They found that high currents (25×10^{-6} A) led to a sudden fracture of the SnO_2 NW (50 nm in diameter and 2.2 μm in length) and to the creation of ultrasharp tips at the broken ends, whereas the TiO_2 NWs (200 nm in diameter, 1.3 μm in length) failed due to Joule-heating-induced melting, after which they retracted into a nanosphere. They

correlated these distinct behaviors with the different bonding natures of the NWs.

Zhao *et al.* [4] performed electrical breakdown measurements of GaN NWs using an *in situ* TEM method with a scanning tunnelling microscopy (STM) holder to apply dc bias. In their experiment, the voltage was applied from 0 to 35 V with a ramp time of 100 ms and a ramp step of 1 V. They found that all the breakdown points are located at the middle of GaN NWs where the melting or decomposition temperature is reached. They also observed that some liquid Ga balls remained on the NWs. This revealed that CaN NWs break due to Joule heating.

Westover *et al.* [5] investigated electrical breakdown in Joule-heated GaN NWs using an *in situ* TEM characterization method with an STM holder. They applied a voltage to the STM tip to cause an electric current to flow through the NW, and then increased the applied voltage until decomposition started as the formation of Ga balls became evident, which occurred at approximately 30 V (18 μA). They also observed that the Ga balls evaporated with increasing voltage and that subsequent voltage increases resulted in nanowire failure. They therefore concluded that NW failure under high currents is primarily caused by thermal decomposition, which is confirmed by TEM images of individual NWs showing the formation and growth of Ga balls before NW failure.

Zhang *et al.* [6] investigated the electrical breakdown of ZnO NWs by applying a longitudinal electric field inside a scanning electron microscope (SEM) equipped with W manipulators. To enable the electrical measurements, they used W tips to press a ZnO NW at the ends to act as electrodes. They then observed the electrical breakdown of individual ZnO NWs due to joint effects of high electric fields and Joule heat. These devices exhibited stable behavior before the applied electric field reached the breaking point at $\approx 10^6$ V/m.

Zou *et al.* [7] studied the electrical failure in $TiSi_2$ NWs using an *in situ* SEM technique and TEM for compositional characterization. For electrical measurements the electrodes were done by an electron beam lithography technique and focused ion beam (FIB)-induced Pt deposition. They increased the current with applied bias until the devices failed. They

found that the dominant breakdown process that induced mass migration and caused irreversible decomposition of $TiSi_2$ NWs was electromigration.

Xu *et al.* [8] performed a TEM-assisted *in situ* joule heat dissipation study of individual InAs NWs. They described two-point electrical measurements performed with *in situ* TEM using a contact with an STM tip. The NW breakdown showed no dependence on the electric current direction; rather, it was broken in the middle, which Xu *et al.* attributed to Joule heating.

Clearly, these explanations of breakdown mechanisms in semiconductor NWs differ, which is related primarily to the fundamentally different physico-chemical nature of NWs. Of course, when analyzing the data reported by different groups, all experimental details should be considered in order to obtain a reliable description of the failure mechanism: how the bias was applied in the breakdown experiments; the material, composition and geometry of the NWs; and the quality of the contacts. Thus, in order to ascertain the driving force of electrical breakdown in individual NWs and improve the semiconductor NW-based electronic device technology, it is extremely important to correlate the experimental conditions with the NW damage behavior. We conclude that there is still a lack of systematic experimental data in the literature that would directly relate experimental conditions, i.e. how the voltage was applied, the quality of the contacts, to electrical breakdown behavior.

In this chapter we present *in situ* (S)TEM and TEM holography studies of the electrical breakdown mechanism in individual InAs NWs. Moreover, we show the results of a controlled modification of InAs NWs by electric field during continuous *in situ* (S)TEM imaging.

5.2. Experimental

The InAs NWs were grown on an InP substrate by the metalorganic vapor-phase epitaxy method. The tapered shape of InAs NWs was obtained by controlling the gas flow rate; further fabrication details have been reported elsewhere [9].

To perform *in situ* electrical measurements *in* TEM, we prepared chips with gold electrodes (contacts) by means of e-beam evaporation from an Au source onto a 100-nm-thick freestanding silicon nitride (SiN) membrane. The electrodes were a 97-nm-thick layer of Au and the adhesion layer between the SiN and the Au was a 3-nm-thick layer of Cr. We wrote the patterns for the Au contacts using e-beam lithography. The detailed fabrication process of transparent SiN membrane and Au electrodes is described in Section 2.2 of Chapter 2.

A focused ion beam technique (FIB) was used to cut the SiN membrane between the electrode pair in order to obtain a SiN-free local area. Then, single nanowires were transferred onto the Au electrodes and positioned at the FIB cut. The InAs NWs were transported manually using sharp glass needles and a precision mechanical micromanipulator. Thus, a part of the nanowire was suspended. To enhance the electrical contact, we deposited Pt on the joints of the InAs NW and Au electrodes by means of FIB with a 10-pA current of Ga+ ions. The schematic illustration of the chip with the nanowire placed on Au electrodes separated by a gap is shown in Figure 5.1.

The InAs NWs were tapered and their lengths ranged from 10 to 15 μm. The distances between two Au electrodes ranged from 2 to 5 μm. Moreover, the lengths of the suspended parts of the NWs varied even when the distance between the electrodes was the same, which was due to a slightly different placement of the NWs during the manual transfer. The diameter range of the suspended parts of the NWs was between 130 and 250 nm. The total resistance of the device, including the Au electrodes, the Pt contacts and the InAs NWs prior to the electrical experiments was 3–20 kOhm.

The chip with InAs NWs was fixed with conductive tape onto an Al_2O_3 chip carrier. The connection between the chip and the Al_2O_3 was made with the standard wire bonding technique. The chip carrier was placed into a custom built-in-house TEM holder connected to an electrical setup (see Section 2.3.2 of Chapter 2). The electrical breakdown process of InAs NWs was investigated by *in situ* TEM and STEM/EDX techniques using a FEI Titan microscope operating at 300 keV. Both the state-of-the-

art TEM with the custom holder and the electrical setup enabled us to record real-time movies of structural and morphological transformations at the nanoscale with the corresponding *I–V* curves. TEM movies were recorded directly from the Titan FLUcam display using Camtasia screen recorder software with a frame rate of 10–15 fps.

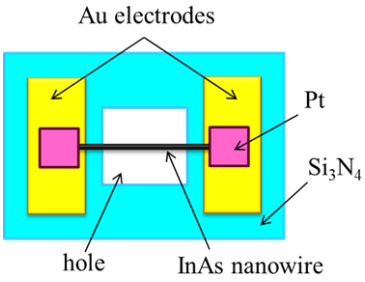

Figure 5.1. Schematic illustration of the MEMS device for *in situ* TEM electrical measurements. The device comprises a chip with a single free-standing nanowire placed on Au electrodes deposited on a SiN membrane.

The electrical breakdown experiments were performed in bias-ramping mode, which allowed us to conduct accelerated experiments for failure process visualization *in situ (S)*TEM. The typical *I–V* curve represents a loop that starts at 0 V and gradually increases to a predefined value of 600–1000 mV, then decreases back to 0 V, and again increases in the negative *I–V* quadrant to the same set value, after which it returns to the initial starting point of 0 V. If a NW does not break and no changes in morphology and structure are detected, a new cycle is performed with a higher voltage. When changes appear, subsequent cycles are applied with the same voltage as in the previous cycle. To observe the morphological and structural changes with *in situ* TEM without prolonging the experiments unnecessarily, we set the voltage ramp to 20–40 mV/s.

An electron holography was applied to study the local variations of the resistance of a nanowire by reconstructing the electrical potential from the holograms of the nanowires when an electric current is flowing through them. The hologram was obtained when part of the electron wave passing through the sample interfered with another part passing through a hole (vacuum). This interference was realized by a charge wire positioned in the selected area aperture plane. Electron waves passing through the InAs NW

and vacuum regions were deflected by the electrostatic potential, which was applied to a biprism wire so that an interference pattern was formed on the image plane. This interference pattern is called an electron hologram and contains the phase information of the electron wave passing through the InAs NW. The only difference to conventional off-axis electron holography is that an electric current passes through the InAs NW.

The built-in-house TEM holder described in Section 2.3.2 of Chapter 2 was used for electrical measurements. The holographic experiment [10, 11] was performed in an FEI Titan G2 60-300 HOLO TEM operated at 300 kV in Lorentz mode for a larger field of view [12]. A Möllenstedt-type electrostatic biprism [13] situated above the selected area aperture plane was used to form an interference pattern. To improve spatial coherence, the elliptical illumination was used [14]. The biprism voltage was set to approximately 110 V, resulting in a fringe spacing of about 3.5 nm. The biprism was rotated to be perpendicular to the Pt contacts (i.e. almost parallel to the nanowire). Such geometry results in perturbation of the reference wave (PRW) [15] by the parallel-plate-capacitor-like field of the electrodes. The effects of PRW together with the results will be discussed in more detail below. The holograms were recorded using a Gatan K2-IS direct electron detection camera operating at 400 fps with approximately 2k×2k resolution. This allowed us to have a temporal resolution of 2.5 msec.

The individual holograms were reconstructed using the Fourier method [11] as follows. First the FFT of holograms was performed, then the side band center was identified as the maximum intensity in the side band region. A circular filter with a radius of half the distance between the side band and the FFT center was set in the center of the side band, and the sinc function was set to smooth the filter edges. The filtered FFT pattern was re-centered and an inverse FFT was performed, which yielded a complex wave. Consequently, the amplitude and phase were calculated. For better visualization, cosine (contour) maps were calculated using the equation $C = \cos(n \times \Phi)$, where n is the amplification factor defining the contour spacing $2 \times \Pi / n$ and Φ is the phase. Additionally, the central band filtering was performed to obtain intensity images using a procedure similar to the one described above but with the filter centered at the FFT origin.

5.3. Results and Discussions

5.3.1. TEM visualization of electrical breakdown

As-grown monocrystalline InAs NWs have a sphalerite (or zinc blende with a face-centred cubic symmetry) structure with a very low density of defects. The NWs contain a 2-nm-thick amorphous layer distributed homogeneously over their entire surface.

Figure 5.2 (a) shows a bright-field TEM image of an InAs NW placed on Au electrodes. The distance between Pt-deposited contacts is 3.5 μm and the freestanding length of an InAs NW is 2.1 μm. The diameter of the nanowire is 140 nm. The stripes and curved lines that appear on the NW are due to bending. Figure 5.2 (b) is the area in (a) between the purple lines rotated 52° counterclockwise. The dark spherical shapes in Figures 5.2 (a) and (b) indicated by green arrows are artifacts formed during the FIB cutting of the holes in the SiN membrane, which causes the SiN edges to curl into spheres.

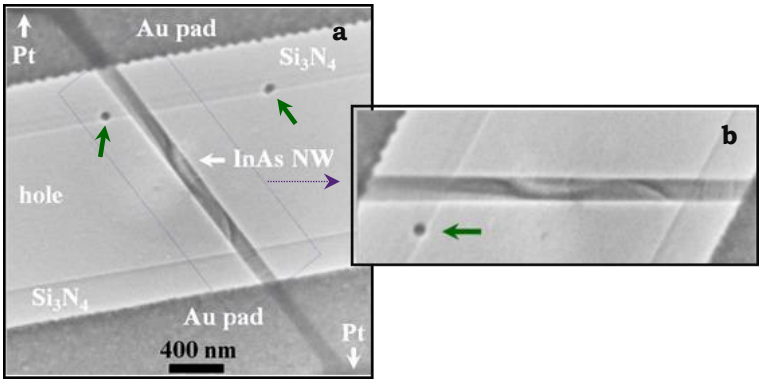

Figure 5.2. (a) Bright-field TEM image of an InAs NW on Au electrodes. (b) The area of (a) between the purple lines rotated 52° counterclockwise. Green arrows indicate the artifacts at the edges of the SiN caused by the FIB cutting of the holes.

In order to find the voltage value at which the NW undergoes structural changes, we applied several voltage loops with increasing voltage until structural changes were observed. The voltage ramp was set to 20 mV/s. Figure 5.3 shows snapshots taken from the real-time TEM movie

recorded as bias voltage was applied. Each image corresponds to a certain segment (or time) of the *I–V* curve. A TEM image of the initial configuration of the InAs NW taken at 0 V and corresponding to the A point on the *I–V* curve is shown in Figure 5.3 (a). When the bias voltage is increased to almost V_{max}=1100 mV in the positive *I–V* quadrant, the InAs NW starts to shrink near the cathode side, forming a neck. At the same time, a small ball starts to grow near the anode side (Figure 5.3 (b); (c) corresponds to points B and C on the *I–V* curve shown in (i)). These changes occurred only near the maximum voltage value. When the polarity is changed at the negative *I–V* quadrant near a maximum negative voltage, the ball that was previously formed near the anode side starts to shrink and finally disappears, while similar sphere-like particles grow on the NW surface near the anode side in the opposite configuration of polarity, see Figures 5.3 (d)–(h) corresponding to points D–H on the *I–V* curve, respectively. No changes in particle shape or size are observed during the subsequent voltage decrease to 0 mV.

We applied the next voltage cycle with the same V_{max}. Figure 5.4 shows images from the TEM movie recorded during the second voltage cycle. Figure 5.4 (a) shows a TEM image of the InAs NW after the first voltage cycle at 0 V. Near the maximum applied voltage, the particles (balls) that formed in the first voltage cycle exhibit the same behavior: they disappear on one side of the NW and grow on the other side, see Figures 5.4 (b)–(f) corresponding to points B–F on the *I–V* curve shown in (g). The spherical particles always grow near the positive electrode in the direction of the electron current. Moreover, the NW becomes significantly thinner where the neck had originally formed in the first cycle and eventually breaks at a voltage of 1080 V, see Figures 5.4 (e) and (f). Although the NW breaks down, the oxide surface layer remains. The current drops first to a value of 0.006 mA in the positive *I–V* quadrant, see Figure 5.4 (g), which we attribute to the final conductance through the oxide skin of the NW. Then, when polarity is switched in the negative *I–V* quadrant, the resistance increases to tens of MOhm.

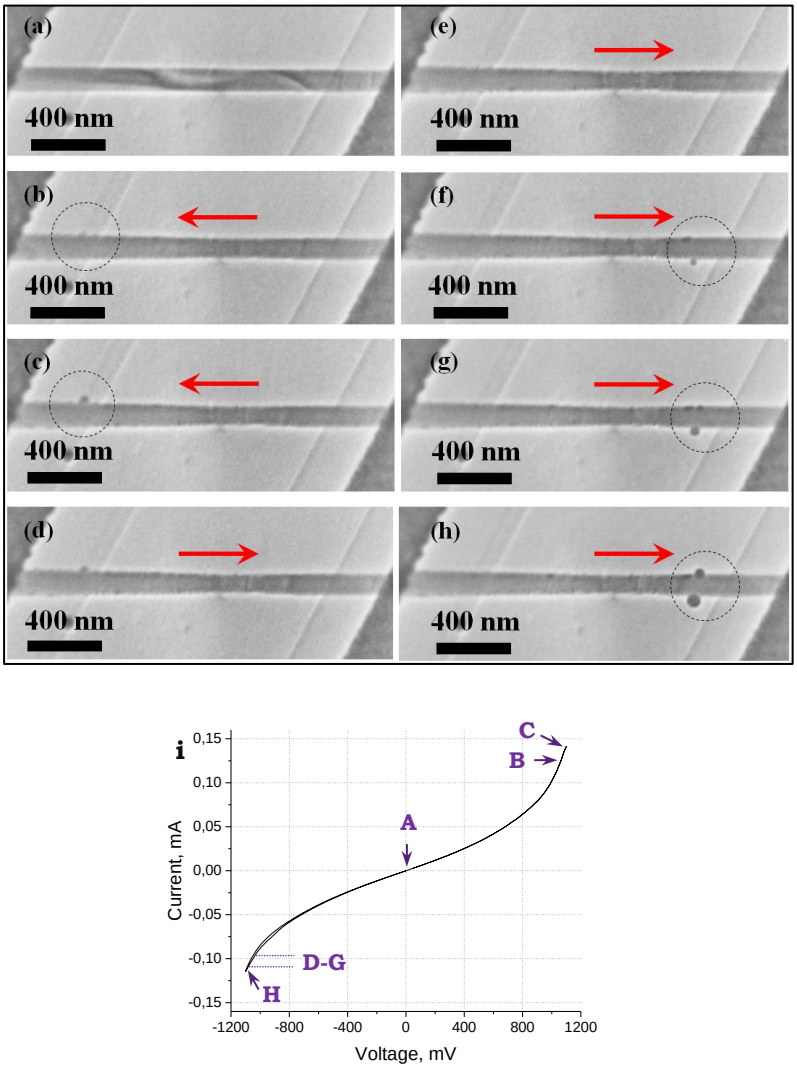

Figure 5.3. Snapshots from the real-time TEM movie recorded as bias voltage was applied. (a) TEM image of the initial configuration of the InAs nanowire taken at 0. (b)–(h) TEM images of the InAs nanowire showing morphological changes as bias voltage is applied. The direction of electrons is shown by red arrows; the location of sphere-like nanoparticles is indicated by dotted circles. (i) *I*–*V* curve with points A–H corresponding to images (a)–(h), respectively.

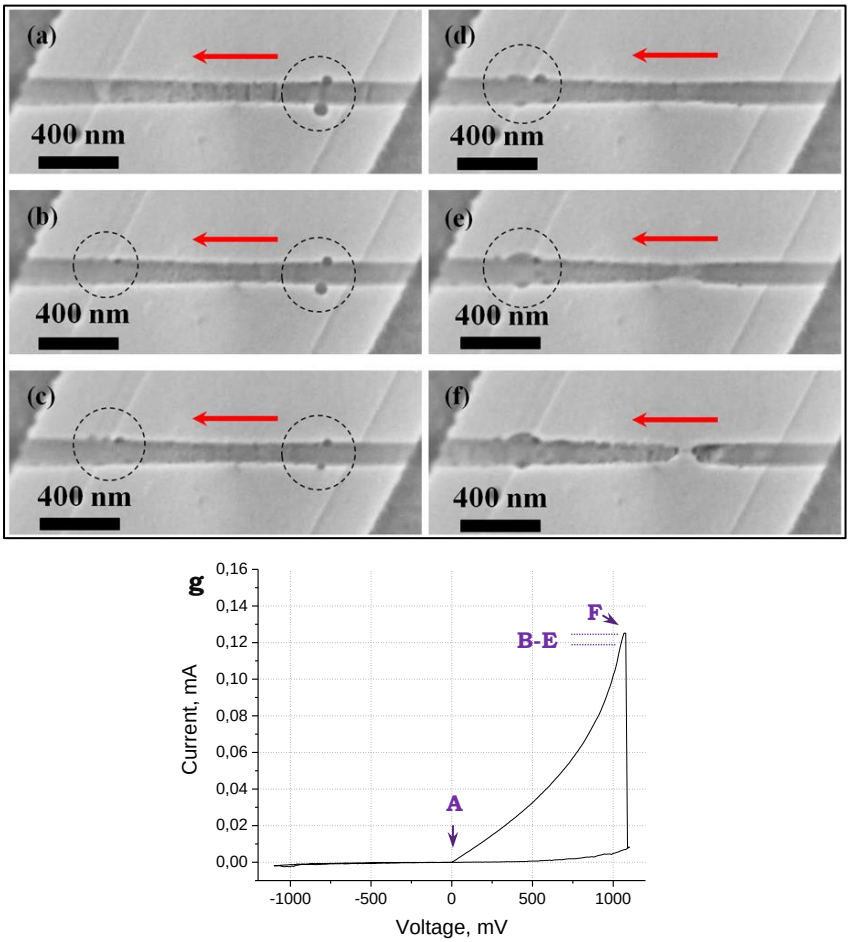

Figure 5.4. Snapshots from the real-time TEM movie presenting the electrical breakdown process in an InAs nanowire occurring after the first cycle shown in Figure 5.3. (a) TEM image of the InAs nanowire after the first cycle, corresponding to point A on the *I*–*V* curve (g). (b)–(f) TEM images of the InAs nanowire corresponding to points B–F on the *I*–*V* curve, respectively. The direction of electrons is indicated by red arrows.

To understand the nature of the sphere-like particles that form near the anode side, we performed an EDX analysis on the InAs NWs after breakdown, see Figure 4.3 in Chapter 3. EDX mapping revealed that these sphere-like particles (balls) are very rich in indium, whereas the nanocrystals in the broken part are rich in arsenic.

In Figure 5.3 we clearly observe that the growth of In particles near the anode side always goes together with the thinning of the NW part near the cathode. When polarity is changed, In forms on the other side (always the anode side) of the nanowire, and the size and number of newly formed In particles is increased. However, we do not observe any changes in the NW's resistance in the linear regions of positive and negative (after the growth of particles) *I–V* quadrants, see Figure 5.5 (a). Moreover the resistance of the NW in the linear regions of *I–V* curves for the first and second cycles (before breakdown) remains the same, see Figure 5.5 (b). To estimate the amount of In increase after the change of polarity in the first cycle, we used ImageJ software to extract the area of In particles from Figures 5.3 (c) and (h). Considering In particles as spheres, we determine their masses to be mass = (density 7.31 g/cm^3)×(volume $(4\pi/3)$(area/π)$^{3/2}$). We find that, after the polarity change, the mass of In becomes approximately three times greater.

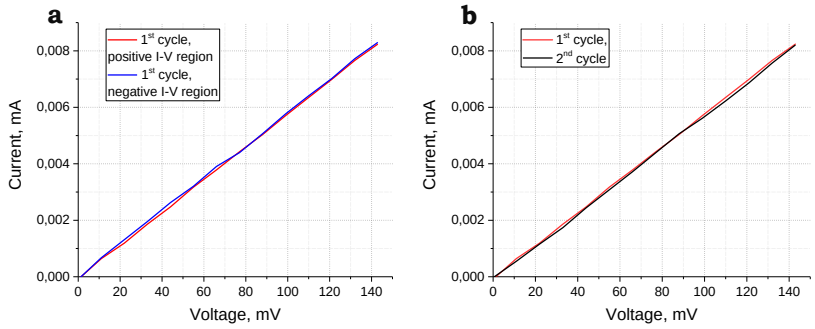

Figure 5.5. (a) Plot of the linear regions of the *I–V* curve (positive and negative) for the first voltage cycle. (b) Overlay of linear *I–V* regions for the first and second cycles.

5.3.2. STEM visualization of electrical breakdown

To observe the influence of the voltage ramp on the behavior of InAs NWs, we recorded *in situ* a STEM movie while applying a voltage with a ramp of 40 mV/s. In order to record images with a minimum of diffraction contrast, the NW was positioned outside of a low zone axis, and the camera

length was set to a small value to allow a contrast change to be attributed to a change in thickness. The frame rate of the STEM movie was set to 4 fps to achieve an acceptable image quality for the chosen camera length and to allow us to record the transport of material in detail.

Figure 5.6 shows snapshots taken from an STEM movie recorded during electrical measurements. The images in Figure 5.6 correspond to three voltage cycles (loops): (a) is the initial view of the NW, (b)–(c) correspond to the first cycle (the *I*–*V* curve is shown in (m)), (d)–(j) are images from the second voltage cycle (the *I*–*V* curve is shown in (n)), (k)–(l) represent the third cycle (positive part of *I*–*V* curve shown in (o)). The maximum applied voltages were 500 mV (b–c), 600 mV (d–j) and 600 mV (k–l), respectively. While increasing the voltage to 500 mV in the first voltage loop, we observed a change in the initially homogeneous contrast of the InAs NW, namely the formation of regions with greater contrast near the cathode side and less contrast near the anode side of the NW. Greater contrast means less material (material depletion) or void formation, whereas brighter areas correspond to material accumulation. Arrows in the images indicate the direction of electron flow from the cathode side (–) to the anode side (+).

Changing the current direction (negative part of the *I*–*V* curve (m)) causes the partially formed mass depletion areas to refill and new areas of mass depletion to grow near the cathode side (for a given configuration of polarity) and new areas of mass accumulation to appear near the anode, Figure 5.6 (c). As no significant changes occurred at this voltage, a new voltage loop is applied with a maximum of 600 mV. Increasing the voltage to 600 mV thins the NW near the cathode side, see Figures 5.6 (d–f), which causes a neck to form near the voltage maximum, see Figure 5.6 (g), the wire to thicken, and hillocks to form at the anode side, see Figures 5.6 (d)–(g). Reversed polarity in the same cycle causes a new thinned area to form near the ex-anode (now the cathode), which transforms into a neck shape. At the same time, the NW becomes thicker at the opposite side (anode), see Figures 5.6 (h)–(j). We applied the third voltage cycle with the same maximum voltage. At 530 mV, a void (material depletion) forms near the cathode side and at 535 mV NW, it breaks at the neck, see Figures 5.6 (k)–(l).

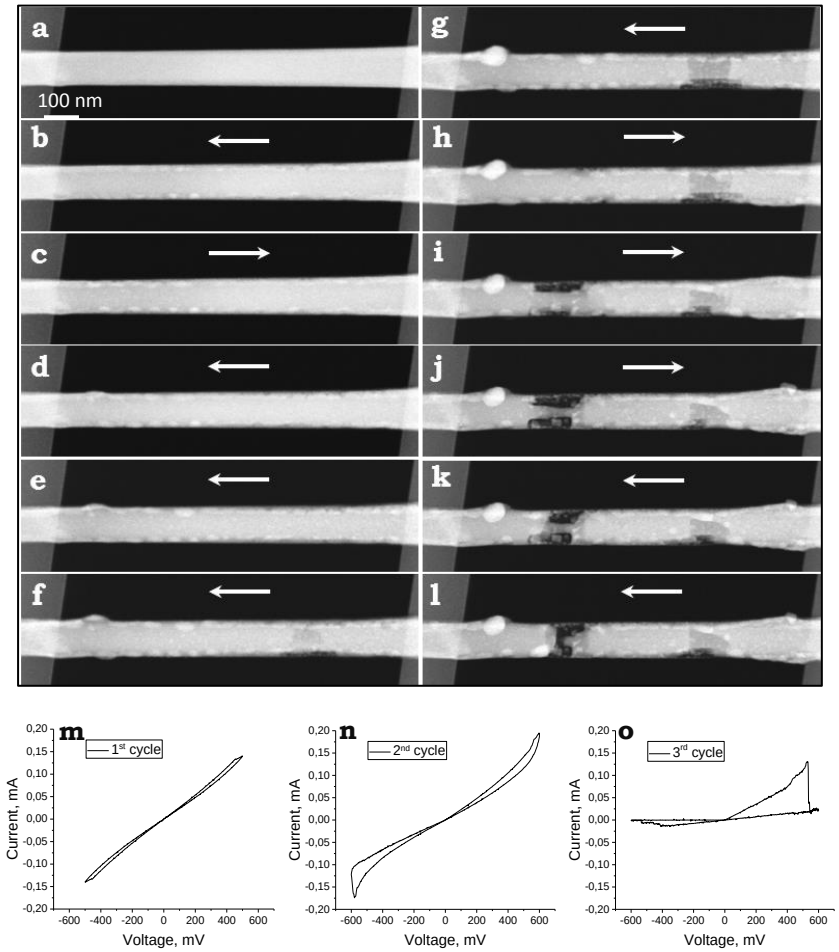

Figure 5.6. Snapshots from an *in situ* STEM movie showing the direction of material transfer under the influence of an applied electric field. (a) Initial configuration of the NW; (b)–(c) correspond to the first voltage cycle and are taken at the voltage maximum in the positive and negative quadrants of the *I*–*V* curve (±500 mV). Images (d)–(g) correspond to the second voltage cycle in the positive *I*–*V* quadrant, showing a thinning of the NW near the cathode, which causes a neck to form and the wire to thicken with hillocks at the anode. Images (h)–(j) correspond to reversed polarity in the second cycle, the formation of a new thinned area that transforms into a neck shape near the cathode, and a thickening of the NW at the anode. Images (k)–(l) correspond to the third cycle, showing a breakdown of the NW. (m)–(o) *I*–*V* curves of the first, second and third cycles, respectively.

We conducted experiments on NWs with different voltage ramps of 20–40 mV/s and observed the process of reversible material transfer in every case. Both TEM and STEM imaging techniques provide useful information. The great advantage of the STEM mode is the ability to observe material transfer due to the mass-thickness contrast.

During these experiments we acquired EDX maps to understand the composition of the areas in STEM images with bright contrast. They showed similar results to those in Figure 4.3 of Chapter 3. The areas with brighter contrast are very In-rich and the particles at the breakdown (grey contrast) are As-rich.

In the first cycle of this experiment we recorded a behavior of the InAs NWs at a voltage that does not result in significant NW damage, but allows the observation of In material migration at the surface between the NW and the InO shell in the direction of electrons. The thinning of the NW always occurred near the cathode together with the accumulation of In mass near the anode. Changing the current direction leads to the opposite situation where partly formed regions of material depletion are refilled near the ex-cathode (now the anode) and new depletion areas appear near the ex-anode (now the cathode). We consider the observed phenomenon to be electromigration because In moves under the influence of an applied electric field in the direction of electrons. Moreover, the areas of material depletion become refilled, depending on voltage polarity. When a higher voltage is applied in the second and third cycles, we observe the thickening of the NW due to intensive In accumulation at the anode near the surface of the NW together with the formation of the neck in the NW at the cathode. Switching the polarity leads to the same situation with respect to new cathode and anode sides.

As can be seen in Figures 5.6 (g), (j) and (k), which correspond to the maximum applied voltages of ±600 mV, In particles are not removed completely from the anode sides by electromigration. We assume that this is due to two reasons. Firstly, when In forms near the anode, the InO shell can be partly broken due to the fast accumulation of material, whereupon some of the In can exit the wire. Changing the polarity results in the electromigration of In located close to the surface of the InAs NW between

the InAs material and the InO shell. The In part that exits the NW at the broken shell and adheres to the surface of the NW is thus less connected, and less force is acting on it because the InO shell is not conducting. This is shown schematically in Figure 5.7.

The second reason is the rate of the voltage ramp itself. As can be seen in "loop" voltage cycles, the applied voltage is not constant like in the experiment described in Chapter 3: the cycle starts at 0 V and the voltage is gradually increased with a curtain ramp. When it reaches the maximum set value, it decreases back to 0 V. As we set a voltage of a cycle such that changes are observed only near its maximum, the rate of the voltage ramp defines the actual time during which the electromigration force is strong enough to cause material displacement. Moreover, in this experiment the voltage ramp is increased to 40 mV/s and the heat rate is also increased, which might explain the difference between these two experiments (described in the Results section of this chapter), where the voltage ramp differs twice.

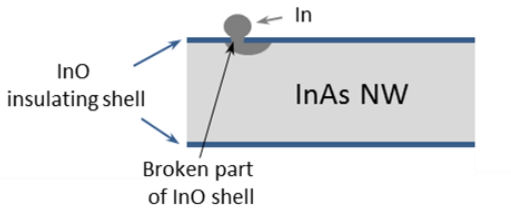

Figure 5.7. Schematic illustration of In material accumulation near the anode side.

We observed significant changes in the NW at the current density of about 7×10^5 A/cm^2. This value is below the observed current density for electromigration in metals [16]. However, in the case of semiconductor, current flowing through it can cause significant Joule heating which, in turn, can lead to a substantially lower critical current density at the start of electromigration. In our experiments we observed both the decomposition and the electromigration phenomenon. We performed *in situ* TEM heating experiments on InAs NWs to find the temperature at which they decompose and observed that this occurs at about 540°C, which is in agreement with

the work of Hertenberger *et al.* [17]. The partial removal of In as well as sublimation of As will result in a chemically less stable compound, which will facilitate electromigration

We found that the NW does not break down at its midpoint as one would expect, given that the Au electrodes and Pt-deposited enhancing contacts between the Au electrodes and the NW are equal. We performed several similar breakdown experiments and observed that the breakdown area is always close to the cathode side. There is a dispersion in the exact location of the breakdown, but the failure behavior remains the same. This might mean that the hottest part of the NW is not in the center, and we assume that the shift from the middle can be due to the Thomson effect [18, 19]. This effect is more significant in semiconductors than in metals because in semiconductors the concentration and the energy of charge carriers depends strongly on temperature. If *n*-type (*p*-type) semiconductors are non-uniformly heated, the electron (hole) concentration will be higher where the temperature is highest. The temperature gradient will lead to an electron (hole) concentration gradient, which in turn will cause a diffusive charge carrier flux. Owing to this electroneutrality imbalance, an internal electric field will be generated. If the voltage is applied to such a semiconductor—depending on the directions of internal and external fields—heat will be released or adsorption will occur in addition to Joule heating.

5.3.3. *In situ* TEM holography visualization of an electrical breakdown

To study the local variations of the resistance of the NW an electron holography was applied by reconstructing the electrical potential from the holograms of the NWs when an electric current is flowing through them. Bright field TEM images (i.e. central band filtered holograms displayed in figure 5.8 (a)-(k)) show the morphological changes in the nanowire that are similar to those observed in previous experiments (see section 5.3.2). First, to acquire a reference hologram, the NW was shifted from the field of view of the electron beam. The hologram of the InAs NW was acquired at 0 V. Then, the hologram of vacuum was subtracted from the hologram of the InAs NW at 0 V in order to obtain information on the mean inner potential of the NW.

Subsequently, the voltage loops were applied with the maximum set voltages of 700–750 mV. During all voltage cycles the voltage ramp was set to 40 mV/s. We acquired holograms of the InAs NW while ramping the voltage to record the *I–V* curves. The images shown in Figure 5.8 represent BF images with corresponding images of the phase, which is amplified to reduce the noise and inserted as a caption in each BF image. Figure 5.8 (a) is the initial configuration of the NW in the absence of an electric field. The rest of the TEM images in Figure 5.8 were acquired during five applied voltage cycles: (b)–(c) correspond to the first cycle where V_{max} = ±750 mV; (d)–(e) correspond to the second cycle where V_{max} = ±700 mV; (f)–(g) correspond to the third cycle where V_{max} = ±720 mV; (h)–(i) correspond to the forth cycle where V_{max} = ±720 mV; and (j)–(k) correspond to the fifth cycle where V_{max} = ±740 mV. Figure 5.8 (l) is a graph of *I–V* curves corresponding to the applied voltage cycles. Black arrows show the direction of the electron flow from the cathode side (–) to the anode side (+). Similar to the experiment described in Section 5.3.2., when voltage is applied to the initial NW, it is gradually thinned near the cathode side as the voltage is ramped near the maximum of the applied value, and the NW represents a wire with a bridge. Under a change of polarity in the same cycle, the bridge gradually moves to the new cathode side near the maximum voltage. Near the new cathode, the shape of the bridge differs from the initial one. The new bridge is smaller in diameter and shorter in length. During the rest of the voltage cycles we observe the same behavior of the bridge location change as well as the change in diameter and length. Comparing images corresponded to different voltage cycles in Figures 5.8, one can observe that the distance which the bridge travels under the polarity change is dependent on the maximum applied voltage of the cycle. In the second cycle at lower value of maximum applied voltage of 700 mV the distance for which the bridge relocates is shorter comparing to that in the first cycle with 750 mV as a maximum value. In the third and the fourth cycles the maximum applied voltage is 720 mV. In both cycles the bridge

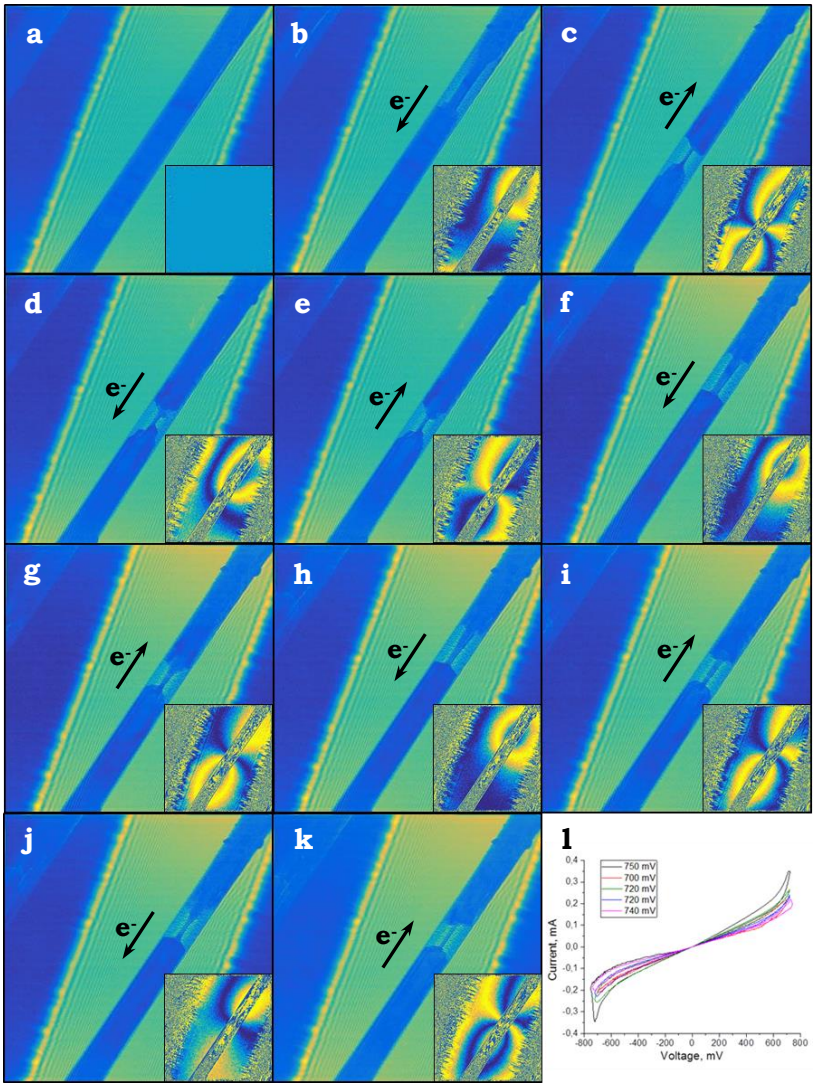

Figure 5.8. TEM holograms: BF images with corresponding images of the phase inserted as a caption in each BF image: (a) initial configuration of the NW in the absence of an electric field; (b)–(c) correspond to the first cycle where V_{max} = ±750 mV; (d)–(e) correspond to the second cycle where V_{max} = ±700 mV; (f)–(g) correspond to the third cycle where V_{max} = ±720 mV; (h)–(i) correspond to the forth cycle where V_{max} = ±720 mV; (j)–(k) correspond to the fifth cycle where V_{max} = ±740 mV; (l) is a graph of *I*–*V* curves corresponding to applied voltage cycles. Black arrows show the direction of the electron flow from the cathode side (–) to the anode side (+).

relocates for a longer distance than that in the second cycle. Remarkable is that the length and the shape of the bridge forming at the same voltage polarity at the positive halves of voltage loops (+720 mV) in the third and the forth cycles are similar. At the same voltage polarity (+720 mV) in these cycles the bridge acquires a tapered shape (see Figures 5.8 (f) and (h)). In the fifth cycle, when applying a voltage ±740 mV, the bridge does not acquire a tapered shape as we observe in Figure 5.8 (j) (+740 mV) as in the previous two cycles at the same voltage polarity (+720 mV) shown in Figures 5.8 (f) and (h). The polarity change at the same cycle (-740 mV) (see Figure 5.8 (k)) results in a formation of the bridge with a symmetrical shape but with a smaller diameter in comparison to Figures 5.8 (g) and (i) which correspond to the same polarity as (k). To follow the changes in the NW in the experiment shown in Figure 5.8, i.e. the bridge location and its shape with respect to the applied voltage value and polarity, the images (a)-(k) in Figure 5.8 are rotated clockwise to bring the NW to a horizontal position and the NW area is cropped as shown in Figure 5.9. The images (a)-(k) in Figure 5.8 correspond to the images (a)-(k) in Figure 5.9, respectively.

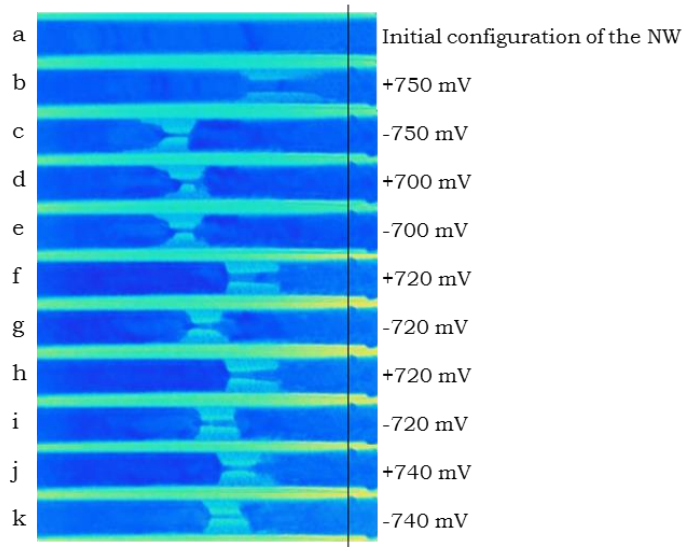

Figure 5.9. (a)-(k) images corresponding to the images (a)-(k) in Figure 5.8, respectively, rotated clockwise to bring the NW to a horizontal position. The In balls occurring on the right are used for exact alignment.

The insets in panels (a)-(k) in Figure 5.8 show phase contour maps with amplification factor (n=8) and taken at lower values of applied voltage (± 150 mV), where the Joule heating is negligible and material does not move because the current density is low. Those represent the difference in electron phase inside and outside the nanowire between 0 V and after each transformation. Although the phase inside the nanowire is not interpretable due to the changes in dynamic diffraction conditions caused by thermal induced bending of the nanowire, the phase outside the nanowire is proportional to projected electrical potential around it. Thus, the contour maps shown in the insets represent the projected equipotential lines. All the maps include the effect of perturbed reference wave meaning that the maps show the result of subtraction of two potential distributions on both sides of the biprism. Since the wire is between two parallel plate electrodes, the field produced by the electrodes will be subtracted and the remaining field will represent the modification introduced by the nanowire itself. Analyzing panels (b)-(k) in figure 5.8 one sees that once the bridge is formed most of potential drop happens in that region, resulting in the equipotential fields localized at the bridge. The closure of the contours in the contact regions that is seen for some of the maps is due to the effect of projection (similar to that described in [20]). Also looking closer at the equipotential maps one may recognize an asymmetry with respect to nanowire axis and an asymmetry with respect to the polarity reversal (see insets pairwise (b)-(c), (c)-(d), (d)-(e) and etc.). The first one comes due to the effect of perturbed reference wave, which results in the asymmetry with respect to the biprism, which is inclined by about 10 degrees to nanowire axis. The second asymmetry (i.e. difference in equipotential contour appearance when the polarity is switched) may be explained if the charge accumulation is not symmetric. That would mean that depending on the direction of the current the size of the dipole corresponding two charges accumulated on different sides of the bridge is different: it is larger for the electron current flowing downwards (Figure 5.8 (b), (d), (f), (h), (j)) and smaller for the electron current flowing upwards (Figure 5.8 (c), (e), (g), (i), (k)). That can happen only in the case if the mobility or concentration of the carriers for one of the regions below the bridge is different from the one above. This may have to do with the polarity during the first voltage sweep when the degradation of

wire takes place. The slight change in chemical composition or defect density may result in change of the carrier concentration or mobility.

From I-V data we find that the resistance of the NW configuration after the first voltage half-loop of the first cycle shown in Figure 5.8(b) is increased for ≈ 21% comparing to the resistance of initial NW configuration. After a second half-loop of the first cycle, the resistance is increased for ≈ 83-84 % compare to the initial resistance of the NW. From the phase images and I-V data we can conclude, that the increase of the resistance is due to the bridge formation in the NW.

The material transport is observed inside the InO shell. It is commonly observed that, after the electrical breakdown of the InAs NW, the InO shell is present and remains unchanged, meaning that it is strong. To observe any changes in a composition along and across the nanowire shown in Figure 5.8 (k), we performed quantitative EDX mapping. Figure 5.10 (a) is a low magnification HAADF image of the NW configuration after five applied voltage cycles shown in Figure 5.8. Figure 5.10 (b) is a quantitative EDX map which corresponds to Figure 5.10 (a) and shows the distribution of both In and As elements in the NW. The indium rich regions are located near the electrodes near the surface of InAs NW. At the bridge location we observe many As-rich material inside the shell. Figures 5.10 (c) and (d) are a HAADF image and the corresponding EDX map image showing the part of the NW with the bridge. Figures 5.10 (e) and (f) are line profile spectra across and along the NW at the bridge location as indicated in Figure 5.10 (c) by blue and purple arrows respectively, showing distribution of In and As elements. From Figure 5.10 (f), we can only conclude that the composition of the bridge is similar to that of the grown (refilled) part of the NW. However, due to the presence of InO shell we cannot give the exact number of atomic concentration of In and As elements.

In the experiment presented in Figure 5.8 we showed that it is possible to modify the geometry of the nanowire by forming a thin bridge under an influence of an applied electric field. Moreover, the position of this bridge can be changed during a voltage cycle under the electrode polarity change. In this experiment we could place the bridge at a specific location by an accurate choice of the voltage for each following cycle. If we observe

visible changes in the NW after first voltage cycle and apply the second cycle with the same or higher voltage value, the NW usually breaks at the constriction (bridge) location. Applying lower voltages after the bridge formation in the NW enables the transport of the bridge along the wire.

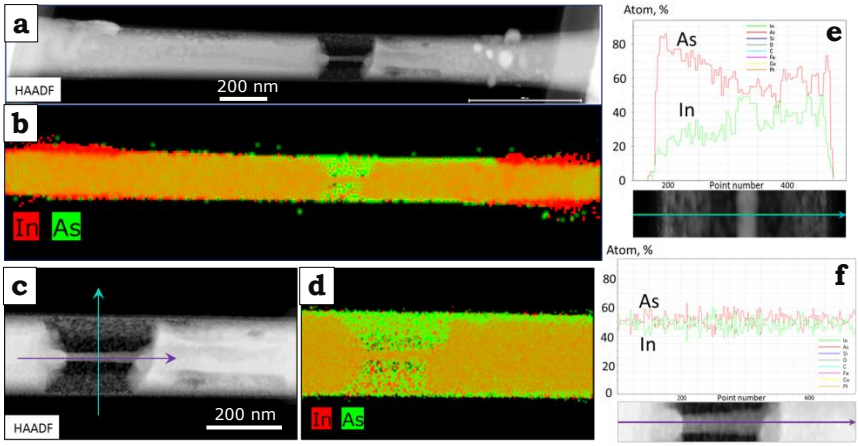

Figure 5.10. (a) Low magnification HAADF image of the InAs NW configuration after five applied voltage cycles shown in figure 5.8. (b) A quantitative EDX map acquired from (a) and shows the distribution of both In and As elements in InAs NW. The In and As elements are shown by red and green colours, respectively. (c)-(d) HAADF image and corresponding EDX map showing the enlarged part of the NW containing the bridge, respectively. (e)-(f) line profile spectra across and along the NW at the bridge location as indicated in (c) by blue and purple arrows, respectively.

It is remarkable that the resistance of the nanowire after the fifth applied voltage cycle has almost the same value as that after the first voltage cycle (0.95 % difference), since one would expect an increase in resistance due to a lot of material migration inside the nanowire (bridge relocation) under an applied electric field, which can lead to a creation of different structural defects. Moreover, from EDX data we find that there is no obvious compositional variation along the NW after several voltage cycles. We observe that there is very less indium near the bridge location, it is accumulated near the electrodes, while As particles remain in the InO shell around the bridge. All this might indicate that there is no diffusion of As or it is insignificant through the InO shell and the As material remains

inside of the shell. Also, the amount of indium near the electrodes is defined mostly by the first cycle, because this voltage cycle has the highest value of applied voltage among all five cycles. It is also in agreement with the fact that the resistance does not change visibly between the first and the last cycles.

We propose that the mechanism of electrical breakdown of InAs NWs is likely the following. First, when a voltage is applied, current induced Joule heating leads to a local decomposition of InAs NW according to reaction:

$$2InAs \rightarrow 2In(s) + As_2(g),$$

which is observed at the current density of about 7×10^5 A/cm^2 and facilitates In atoms movement from the hot area near the surface between the NW and an amorphous skin caused by electromigration, whereby As sublimates. In [21] it is reported on threshold current density for electromigration in pure indium thin films (100 nm thick) on SiO_2-layer which is about 1.40×10^4 A/cm^2 at temperature of 399K. When the bridge is formed, the local current density flowing through it is about $(1.5\text{-}6)\times10^7$ A/cm^2. This value is two order higher than the value needed for the start of decomposition. So, the local Joule heat at the bridge is expected to be bigger. Therefore, one would expect the breakdown to take place, however, we don't observe it. On the contrary, the bridge relocates when polarity is switched and gets a similar tapered shape (see Figure 5.8). We assume that this situation takes place because the InO shell together with the InAs NW can be considered as a closed system, where there is no loss of sublimated As or it is insignificant through the InO shell. It is likely that the mechanism of the bridge migration (relocation under a polarity change) is electromigration phenomenon. Indium atoms driven in the direction of electron current probably electromigrate on the surface of the bridge forming an indium layer (in fact a layer of flowing In atoms) around the bridge. Most of the current is passing through this indium layer and thus the current through the InAs bridge is relatively small. This layer can serve to protect the bridge from As sublimation and the subsequent breakdown. The direction of indium migration is opposite to the direction of bridge

movement. Indium, previously formed near the anode side, moving to the new anode under a polarity change, probably reacts with As according to:

$$2In(s) + As_2(g) \rightarrow 2InAs(s).$$

Thus, the In atoms moving to the anode side react with As atomic gas and this results in the formation of InAs material at the adjoined part of the NW in the direction of electron flow and, consequently, removal of the material from the adjoined NW part in the direction opposite to an electron flow, which results in the bridge movement to the cathode side. The tapered shape of the bridge (Figure 5.8 (b), (f), (h)) can be a result of a temperature gradient along the wire. Indeed, the shape of the bridge is tapered towards the contact pad, which is a heatsink in this case.

5.4. Conclusions

In this chapter we presented *in situ* TEM/STEM and TEM holography experiments on electrical breakdowns of InAs NWs while simultaneously recording the *I–V* properties. We showed that, by selecting the voltage and the rate of voltage ramp in a "loop"-type of applied voltage, it is possible to modify the geometry of the nanowire by forming a thin bridge under an influence of an applied electric field. Moreover, the location of this bridge in the nanowire can be changed during a voltage cycle under the electrode polarity change. We showed that it is possible to place the bridge at a specific location by an accurate choice of the voltage for each following cycle. From EDX data we found that the composition of the bridge and the adjoined parts of the NW are similar. From holography data we have deduced that the local variations of the resistance in the nanowire are at the bridge location, which is the most resistive part of the NW. We proposed the possible mechanism of electrical breakdown in InAs NWs, which is a combination of electromigration, decomposition due to Joule heating and presence of InO shell.

References

1. C. M. Lieber. *Semiconductor nanowires: A platform for nanoscience and nanotechnology*. MRS Bulletin, 2011, 36, 1052-1063.

2. W. Lu and C. M. Lieber. *Semiconductor nanowires*. J. Phys. D: Appl. Phys., 2006, 39, R387–R406.

3. A. Nie, J. Liu, C. Dong and H. Wang. *Electrical failure behaviours of semiconductor oxide nanowires*. Nanotechnology, 2011, 22, 405703, 1-7.

4. J. Zhao, H. Sun, S. Dai, Y. Wang, J. Zhu. *Electrical breakdown of Nanowires*. Nano Lett., 2011, 11 (11), 4647–4651.

5. T. Westover, R. Jones, J. Y. Huang, G. Wang, E. Lai and A. A. Talin. *Photoluminescence, Thermal Transport, and Breakdown in Joule-Heated GaN Nanowires*. Nano Lett., 2009, 9 (1), 257–263.

6. Q. Zhang, J. Qi, Y. Yang, Y. Huang, X. Li and Y. Zhang. *Electrical breakdown of ZnO nanowires in metal-semiconductor-metal structure*. Appl. Phys. Lett., 2010, 96, 253112.

7. C.-X. Zou, J. Xu, X.-Z. Zhang, X.-F. Song and D.-P. Yu. *Failure mechanism analysis of electromigration dominated damage in TiSi2 nanowires*. J. of Appl. Phys., 2009, 105, 126102.

8. T. T. Xu, X. L. Wei, J. P. Shu and Q. Chen. *Transmission electron microscopy assisted in-situ joule heat dissipation study of individual InAs nanowires*. Appl. Phys. Lett., 2013, 103, 193112 .

9. M. Scheffler, S. Nadj-Perge, L. P. Kouwenhoven, M. T. Borgstrom, E. P. Bakkers. *Diameter-dependent conductance of InAs nanowires*. J. Appl. Phys., 2009, 106, 124303.

10. D. Gabor. *A New Microscopic Principle*. Nature, 1948, 161, 4098, 777–778.

11. M. R. McCartney, D. J. Smith. *Electron Holography: Phase Imaging with Nanometre Resolution*. Annual Review of Materials Research, 2007, 37(1), 729–767.

12. C. Boothroyd, A. Kovács, and K. Tillmann. *FEI Titan G2 60-300 HOLO*. Journal of Large-Scale Research Facilities JLSRF, 2016, 2(0), 44.

13. G. Möllenstedt and H. Düker. *Beobachtungen und Messungen an Biprisma-Interferenzen mit Elektronenwellen*. Zeitschrift für Physik, 1956, 145(3), 377–397.

14. D. C. Joy, Y.-S. Zhang, X. Zhang, T. Hashimoto, R. D. Bunn, L. Allard, and T. A. Nolan. *Practical Aspects of Electron Holography*. Ultramicroscopy, 1993, 51(1), 1–14.

15. G. Matteucci, G. F. Missiroli, E. Nichelatti, A. Migliori, M. Vanzi, and G. Pozzi. *Electron Holography of Long-range Electric and Magnetic Fields*. Journal of Applied Physics, 1991, 69(4), 1835–1842.

16. C. M. Tan, A. Roy. *Electromigration in ULSI interconnects*. Materials Science and Engineering, 2007, 58, 1-75.

17. S. Hertenberger, D. Rudolph, J. Becker, M. Bichler, J. J. Finley, G. Abstreiter, G. Koblmüller. *Rate-limiting mechanisms in high-temperature growth of catalyst-free InAs nanowires with large thermal stability*. Nanotechnology, 2012, 23, 235602.

18. T. D. Sands. *Designing Nanocomposite Thermoelectric Materials*. 2005. Available at https://nanohub.org/resources/383

19. P. J. Price. *Theory of Transport Effects in Semiconductors: Thermoelectricity*. Phys. Rev., 1956, 104, 1223.

20. G. Matteucci, G. F. Missiroli, M. Muccini, and G. Pozzi. *Electron Holography in the Study of the Electrostatic Fields: The Case of Charged Microtips*. Ultramicroscopy, 1992, 45(1), 77–83.

21. K. V. Reddy, J. J. B. Prasad. *Electromigration in indium thin films*. J. Appl. Phys., 1984, 55, 1546-1550.

CHAPTER 6

In situ TEM visualization of electromigration-induced nanogap formation in AuPd nanowires

6.1. Introduction

Electromigration is a phenomenon of material transport caused by momentum transfer from conducting electrons, moving in the applied electric field, to the lattice ions [1]. Electromigration is known to be a serious reliability issue in micro- and nanoelectronics since it can cause significant degradation of thin metallic nanowires (NWs) when an electrical current of high density (exceeding curtain threshold value) is passed through the wires [2,3]. However, despite the destroying influence of electromigration on nanoelectronics, which results in irreversible changes of wire's geometry and microstructure and subsequently can lead to a breakdown, electromigration can be applied for controlled nanoscale modification of the wires. In a research field of nanofabrication, electromigration is well utilized technique to produce nanogap electrodes – a pair of metallic electrodes with several nanometers (1-10nm) of separation [4-8]. These nanogap electrodes can be used for single molecule electronic experiments [9], to measure separate nanocrystals [5, 10, 11], as sensors for biomedical applications [12].

When producing nanogap electrodes to study the properties of trapped nano-objects, the main issue is the control of the size and shape of nanogaps. The use of conventional electromigration (bias-ramping electromigration (BRE)) technique with a standard voltage ramp for nanogap formation often results in instantaneous and unpredictable changes in the NW geometry leading to its random failure and shape of the electrodes caused by rapid changes in current density and temperature of the NW at the last stage of breakdown. In order to obtain reproducible and stable nanogaps a good control of the currents causing electromigration should be performed. One of the possibility is to apply a feedback-controlled electromigration (FCE) technique based on feedback algorithm which monitors the resistance of the NW and as soon as a sudden change is occurred the applied current is reduced or switched off. The feedback mechanism allows to obtain a good repeatability of the nanogap dimension and its shape [13,14].

Possibility to fabricate NWs on freestanding silicon nitride (SiN) membranes which are transparent to high-energy electrons allows

transmission electron microscopy (TEM) observation of dynamics of nanogap formation (*in situ* TEM), direct relation of nanogap purity with no metal particles left in the junction which can cause parasitic conductance, reproducibility and stability of the nanogaps over time. There is a number of reports on *in situ* TEM visualization of nanogaps produced by FCE technique in gold (Au) NWs since this material is well utilized in molecular electronics [14-16]. The average nanogap size in Au NWs is about 5-6 nm and it slightly increases with the time due to the surface tension of Au tending to smooth out the features. Also, there are several reports on fabrication of platinum (Pt) nanogaps which seem to be more stable over time than the Au type and their average size is about 2-4 nm [17,18]. Also, the fabrication of small and stable nanogaps by FCE using AuPd NWs is reported including resistance measurements and scanning electron microscope (SEM) imaging to give an indication of the separation between the electrodes [7]. However, a resistance measurement does not provide a reliable method of characterizing nanogaps as well as SEM-imaging due to the resolution is low to characterize the shape and the size of the gaps. Currently, it has not been reported yet

In this Chapter we present *in situ* (S)TEM investigation of gap formation in AuPd NWs using BRE and FCE techniques. Moreover, the time stability of electromigrated nanogaps obtained by both techniques is analyzed.

6.2. Experimental

Polycrystalline metallic AuPd NWs (or nanobridges) with the thickness of 15 nm were produced by e-beam evaporation on 100-nm-thick silicon nitride membrane substrates. The AuPd NWs were 500-800 nm long with a width of 200-250 nm. The contacts to the NW were prepared by e-beam evaporation from gold source on top of contact pads of AuPd NWs. The contacts were made with a 97 nm-thick Au-layer and a 3 nm-thick Cr. The patterns for AuPd nanobridges and Au contacts were written using e-beam lithography. The detailed description of chip fabrication process is

given in section 2.2 of Chapter 2. Each 3x3 mm^2 chip contains 20 AuPd NWs with electrical contacts.

For *in situ* electrical measurements, the chip is fixed and wire-bonded to Al_2O_3 chip carrier which is placed into TEM holder for electrical measurements connected to an electrical setup. The image of the holder tip is shown in figure 2.12 of Chapter 2. The description of electrical setup is given in section 2.3.2 of Chapter 2. We performed electromigration experiments on AuPd nanobridges using two different modes: bias-ramping electromigration (BRE) mode with an uniform increase of voltage and feedback-controlled electromigration (FCE) mode. In the bias-ramping mode the bias voltage applied to the AuPd NW increases linearly with the ramp of 15-20 mV/s up to the maximum set voltage value V_{max} or to $V<V_{max}$ where NW is broken. If the NW is not broken at $V=V_{max}$, the voltage is decreased with the same ramp to 0 V and then, increased to negative voltage range to $V= -V_{max}$, followed by a decrease back to the starting point of 0 V. Thus, the corresponding I-V curve of one electrical measurement in the bias-ramping mode represents a "voltage loop" (or "voltage cycle"). If the NW is not broken after one voltage cycle, next voltage cycles are applied with slight increase of the maximum set voltage value until the NW breaks. In FCE mode the conductance of the wire is constantly monitored while the voltage increases. If there is a sudden decrease in conductance (the measured conductance value is less than the curtain predefined value), the feedback control mechanism reduces the voltage to a small value. When a new reference conductance is set, this process starts again. The feedback control algorithm stops when a set conductance value is reached.

The electromigration process of AuPd NWs was investigated by *in situ* (S)TEM techniques using a FEI Titan microscope operating at 300 keV. Camtasia Studio software [19] was used to record the movies corresponding to *in situ* TEM electrical measurements directly from the computer screen with the frame rate of 10-15 fps. TEM Imaging & Analysis (TIA) software was used to record STEM movie with a frame rate of 2 fps.

6.3. Results and Discussions

Figure 6.1 presents snapshots taken from *in situ* STEM movie showing a typical nanogap formation in AuPd NWs using a BRE technique. Figure 6.1 (a) represent an initial image of the AuPd NW in the shape of the bridge between contact pads. As-fabricated AuPd bridge (length 750 nm, width 250 nm, thickness 15 nm) is polycrystalline and consists of small grains with an average size of 3 - 5 nm. To describe the changes in the bridge with respect to its geometry, the black arrows are drawn to indicate the axis: x and y are along the bridge length and width respectively, z is perpendicular to (x,y)-plane. The rest of the images in figure 6.1 corresponds to seven voltage loops. Figure 6.1 (b) corresponds to image acquired after first voltage cycle with the applied voltage value of 400 mV. The grain size in the bridge is visibly increased due to Joule heating. When the voltage is increased to 430 mV in the second voltage cycle, the bridge narrows near the cathode side in y-direction and small hillocks can be observed near the anode side (figure 6.1 (c)). To indicate the direction of electrons and, thus, the electrode polarity, the white arrows are drawn in the images (cathode side (–) and anode side (+)) (along x-direction). At the moment when electromigration starts the current density is about 4.7×10^7 A/cm^2. When the voltage is increased to 450, 470 and 480 mV in the third, fourth and fifth voltage cycles respectively, the shape of the bridge represents a distorted structure with thinner and thicker regions (along y-direction) which are changed depending on direction of electron flow (figure 6.1 (d)-(g)). The bridge always constricts near the cathode side and when polarity is changed the narrowed areas being formed near ex-cathode are refilled (now it is the anode side) and a new narrowing (thinner region or constriction in y-direction) forms near new cathode side. Images shown in figures 6.1 (h)-(j) correspond to the sixth voltage cycle and (k)-(l) to the seventh cycle. Despite the presence of the constriction (along y-direction) in figure 6.1 (h) near the cathode, under opposite configuration of electrode polarity it is refilled and a new constriction is formed in a shifted position – close to the centre of the bridge and not near the cathode side (see figure 6.1 (j)). One would expect that the breakdown will occur in the narrowest part of the bridge since the current density is the highest there as well as

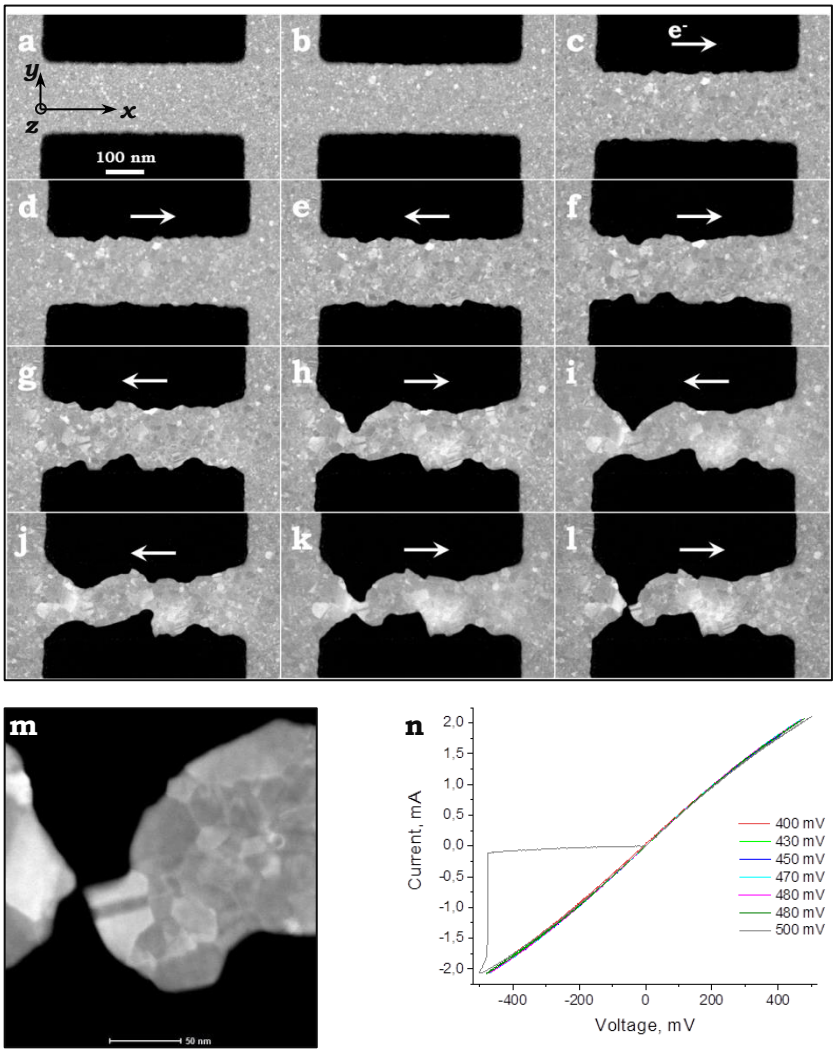

Figure 6.1. Snapshots taken from in situ STEM movie showing a typical nanogap formation in AuPd NWs using a BRE technique. (a) An initial image of AuPd NW in the shape of the bridge between contact pads. (b) Image of the bridge after 1st voltage cycle (± 400 mV). (c)-(g) Images showing evolution of the bridge during 3rd, 4th and 5th electromigration cycles with the set voltages of 450, 470 and 480 mV. (h)-(j) Images acquired during 6th electromigration cycle and (k)-(l) correspond to 7th cycle. (m) Image of the nanogap and (n) is a typical I–V curve showing several voltage cycles. White arrows indicate the direction of electrons (from cathode (–) to anode side (+)).

temperature is expected to be the highest, however, the change in the direction of electrons leads to a reverse of atomic flow in the direction of electrons and filling of the constriction near the ex-cathode. The position of the constriction which is close to the centre of the bridge in figure 6.1 (j) might be explained by the fact that when bridge is deformed, the distribution of mechanical and thermal stresses is not uniform as for the initial configuration of the bridge. When the voltage is increased to 500 mV in the last voltage cycle, the bridge breaks near the negative electrode. A magnified image of the nanogap with the size of 4.12 nm is shown in figure 6.1 (m). The electrodes on both sides of the nanogap have an asymmetric shape. The tips of the electrodes have the same crystal orientation and originates from a single grain. The results on nanogap formation using a BRE technique shown in figure 6.1 are similar for all studied AuPd nanobridges (18 nanobridges). A typical I–V curve of voltage cycles is shown in figure 6.1(n).

Figure 6.2 shows TEM images acquired during electromigration process in AuPd NW using FCE technique. The initial view of the bridge before the electrical measurements is shown in figure 6.2 (a). In figure 6.2 (b) a slight grain growth is observed to start prior to electromigration. The grain growth is occurred due to the temperature rise in AuPd NW which is current-induced Joule-heating. The nanowire starts to thin down close to the cathode side and the grain growth progresses. When the electromigration starts, the current density is about 4.9×10^{7} A/cm^{2}. As can be seen from figure 6.2 (c)-(f), the continuously narrowing neck has an asymmetrical shape. In the last stage of electromigration a tiny neck is formed as shown in figure 6.2 (g)-(h). As a result, a nanogap is formed (figure 6.2 (i)). The size of the nanogap is about 1.72 nm. A typical I–V curve of FCE process in AuPd NWs is shown in figure 6.2 (j). The nanogap formation presented in figure 6.2 is similar to all studied AuPd nanobridges using FCE technique (22 nanobridges).

The presented two electromigration modes used for fabrication of nanogap electrodes show that the nanogap with the size less than 5 nm can be obtained by both techniques. When FCE mode is applied, the nanogap is always created near the cathode side. However, in case of BRE mode the nanogap can be formed near the cathode or close to the centre of the bridge.

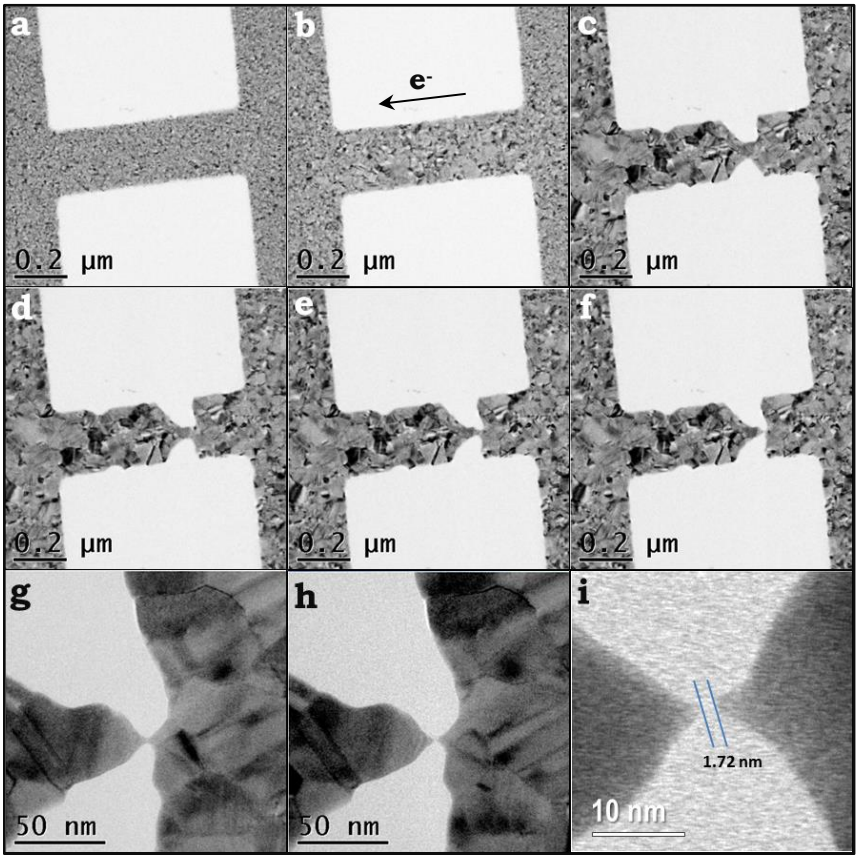

Figure 6.2. TEM images showing FCE process in AuPd NW. (a) Initial view of the bridge, (b) grain growth in the bridge, (c)-(f) process of nanowire narrowing, (g)-(h) the last stage of electromigration in the neck, (i) a typical nanogap, (j) a typical I–V curve of FCE process in AuPd NWs.

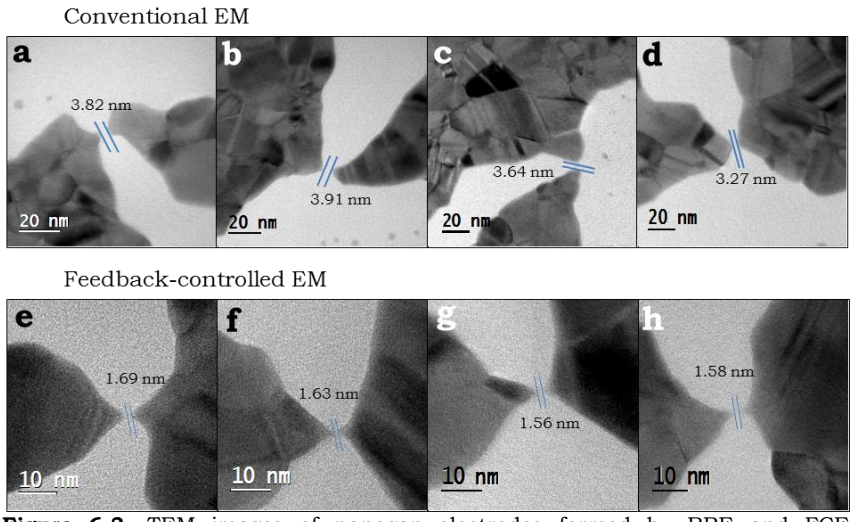

Figure 6.3. TEM images of nanogap electrodes formed by BRE and FCE techniques showing the shape of the electrodes and the sizes of nanogaps; (a)-(d) nanogaps formed by BRE and (e)-(h) nanogaps created by FCE techniques.

The exact location of nanogap is difficult to predict since at the moment of bottle-neck shape formation at the bridge since it is significantly deformed and has an asymmetric shape. The nanogap electrodes created by both electromigration techniques show an asymmetry in their shape. However, the tips of the electrodes obtained by BRE and FCE techniques show a symmetry in a small scale approach (10-15 nm). In BRE mode both electrode (cathode and anode) tips have an approximately point-like shape, sometimes the cathode electrode tip has more flat or rounded shape. In FCE both electrode tips have always point-like shape (in several nanometers approach). In figure 6.3 several nanogap electrodes formed by both electromigration techniques are shown where the shape of the electrodes as well as nanogap sizes can be seen. In [15] Heersche *et al* studied the nanogap formation *in situ* TEM in a gold nanowire by FCE technique. They showed that in case of gold material, the electrodes have a sharp tip at the cathode side and a blunt tip at the anode (at the scale of several nanometers). They mention that this shape of the electrode tips might be due to that the direct force of electric field become dominant and very high near the gap at the instant the Au NW breaks, which can result in a quick deformation of the electrodes and in a backflow of material. Their data are

also in agreement with report on the shape of electrode tips of Strachan *et al* [16]. Also, in [16] the influence of the shape of electrode tips on the stability of nanogap is analysed by investigating their time evolution with TEM. It is found that the nanogaps are expanded over time and the locations of greatest curvature are smoothed out, which is attributed to the surface tension of the Au tending to smooth out the abrupt features. Their report on nanogap evolution after electromigration is found to be also consistent with the report of Zandbergen *et al* [20] on continued relaxation of Au nanogaps made by electron beam bombardment even after an intense e-beam irradiation is completed.

To determine the time stability of AuPd nanogaps created by both electromigration techniques, we acquired TEM images directly after nanogap formation and after one week. The size distribution functions of just created nanogaps by BRE and FCE techniques are shown in figure 6.4 (a) (18 nanobridges) and (b) (22 nanobridges) respectively. The average nanogap size for nanogaps created by BRE mode is 3.5-4 nm and for nanogaps fabricated by FCE is1.5-2 nm. After experiments the chips with nanogap electrodes were left at room temperature and after one week we carried out TEM inspection of all fabricated nanogaps using two electromigration techniques to investigate their stability. No changes in the shapes of electrodes and the sizes of the nanogaps were detectable for all fabricated structures.

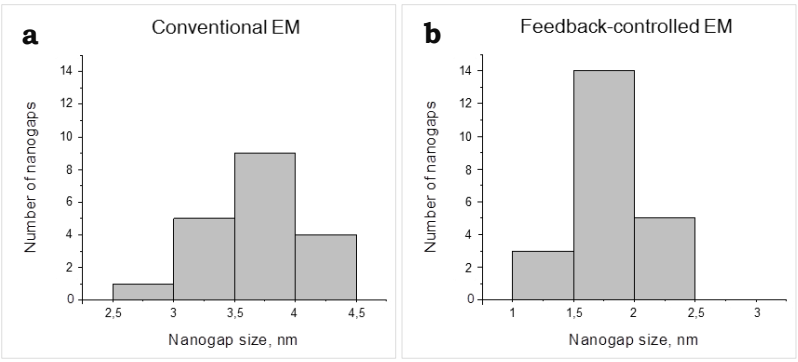

Figure 6.4. The size distribution functions of just created nanogaps by (a) BRE and (b) FCE techniques.

As one can see from figures 6.1 and 6.2, when current is passed through the bridge, the void formation starts always near the cathode side and not in the centre of the bridge, as one can expect considering that the maximum temperature is in the centre, given that the contact pads are equal, have much larger dimensions than the bridge and can be considered as two heatsinks. In [21] to determine the local increase of Pt-bridge temperature due to Joule heating during current passage, a thin layer of bismuth (15 nm) was deposited (material with low melting temperature (≈270 °C)) on the backside of SiN membrane under the Pt-bridge. It was shown that the melting of Bi starts at the centre of the structure and not near the cathode side where the breakdown is usually occurred. The electrical breakdown near the cathode side is usual observation in metal NWs (nanobridges) with uniform cross section and, thus, current density. In our experiments the nanobridge is always connected to large contact pads, which means that if the current density of ≈ 5×10^7 A/cm^2 (approximately at this value we observe electromigration in AuPd) is flowing through the bridge, for contact pads this value is ≈ 4×10^6 A/cm^2. Due to this, the current density follows a step function profile at the entrance to the bridge and the temperature along the bridge will be higher than at contact pads. Consequently, the material which is pushed away by the momentum transfer between the conducting electrons and lattice ions from the cathode side cannot be refilled by the atomic flow coming from the contact pad. Along the straight bridge the current density is constant (until the shape of the bridge is close to initial configuration) and the atoms pushed away along the bridge will be replaced by the atoms coming from the cathode. Near the anode side the material will be accumulated due to connection to the contact with larger area, so the electron wind force becomes significantly less. Moreover, since electromigration is thermally activated process, near the positive large contact electrode the temperature is supposed to be small. Also, in [22] it is reported on experiment in which Au bridge with the constriction was fabricated between two large contact pads in order to enhance the current density and create a hot spot at a predefined position (constriction position). It was expected that electromigration would result in a break position at this constriction,

however, it was not observed – the breakdown was occurred near the cathode side.

The shape of the electrodes (not electrode tips) after the nanogap formation is different for the cathode and anode sides in both electromigration modes. In case of BRE mode the electrode shape is hard to predict, its appearance is always different due to the way of voltage applying – "loop" way, which means that material is transferred from one side to another during one experiment due to polarity change. Moreover, since for each cycle we set a maximum voltage value, the program does not stop if any change in resistance is detected and it provides less control during bias-ramping mode. In FCE mode the electrodes have always a blunt cathode electrode and a pointed-like anode side. Figure 6.5 shows several typical images of electrode shapes in FCE mode. As well as in BRE mode, the location of constriction formation is close to the cathode side.

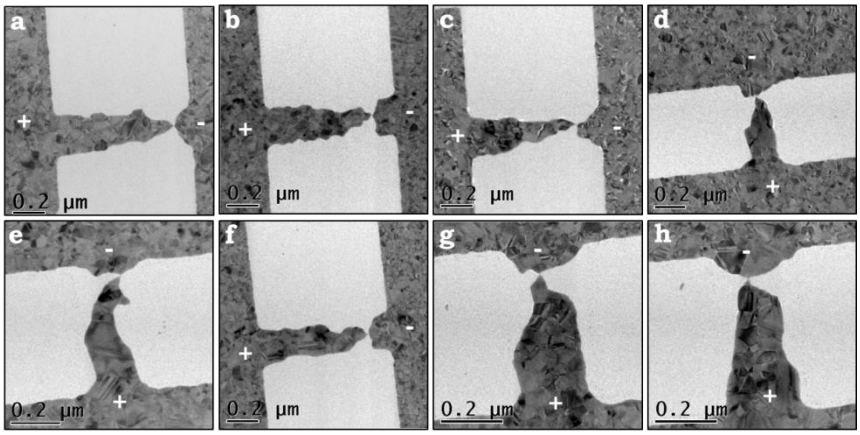

Figure 6.5. TEM images of typical electrode shapes formed by FCE technique in AuPd NWs.

When material is partly removed from the cathode side by electromigration, the temperature distribution is expected to change. We assume that the maximum of temperature should be shifted to the cathode side due to expected higher resistance value at this area. Figure 6.6 shows a schematic illustration of expected temperature and current density profile for initial configuration of the bridge and after some material removal from the negative electrode. Being a thermally assisted directional mass

transport, electromigration will move the atoms with higher kinetic energy (hotter place) easier to the anode side. Near the cathode side the temperature will drop faster due to the cathode heatsink proximity, while for the anode side the temperature will drop slower. Once a constriction is formed, the temperature distribution will have an additional peak due to

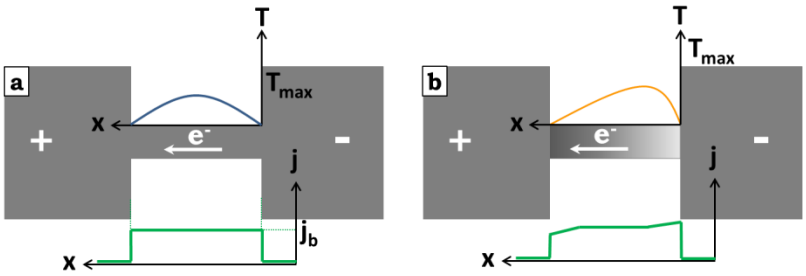

Figure 6.6. A schematic illustration of expected temperature and current density profile for initial configuration of the bridge (a) and after some material removal from the negative electrode (b), where T and j is the temperature and current density, respectively.

local resistance increase at the constriction. It is likely, that the further narrowing should be occurred at the constriction and this is what we observe in our experiment (see figure 6.2 (d)-(f)).

TEM images showing the detailed process of the constriction formation in FCE mode are presented in figure 6.7. Figure 6.7 (a) is TEM image of the initial configuration of the bridge before the electrical measurements. Figure 6.7 (b) is TEM image showing the grain growth under an applied voltage due to Joule-heating prior to electromigration. TEM images with higher magnification taken from the area indicated by black square in figure 6.7 (b) and showing the electromigration process in FCE mode are presented in figure 6.7 (c)-(j). We have found that during the constriction formation, TEM image showed in figure 6.7 (f) is typical for the studied nanobridges, when a single grain surrounded by several grain boundaries is present in the narrowest area. It was expected that continued narrowing of the bridge due to electromigration would occur along the grain boundary which is typical for observed phenomenon in gold [15] or platinum [18] nanobridges during FCE process. However, as one can see in figure 6.7 (g)-(j), further narrowing occurs inside the grain and not at grain

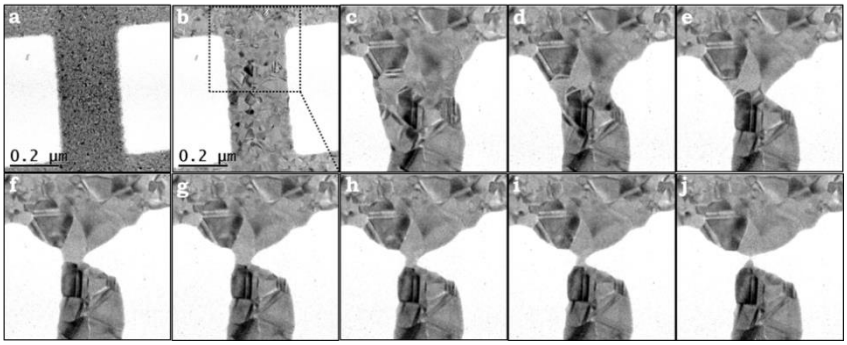

Figure 6.7. TEM images showing the detailed process of the constriction formation in FCE mode: (a) initial configuration of AuPd nanobridge before electrical measurements; (b) image showing grain growth during voltage applying; (c)-(j) images of the area indicated by black square in (b) and showing the electromigration process in FCE mode.

boundary, which might indicate that the surface diffusion prevails in AuPd NWs. Under an applied electric field mass transport in polycrystalline metal NWs can occur through different diffusion paths of which the important ones are lattice diffusion, grain boundary diffusion and surface diffusion. The total material transport is determined by the sum of the mass transport taking place along each of these paths [23, 24]. Typically, the material transport through these paths is considered by setting an effective diffusion coefficient. The effective diffusion coefficient is determined by the dominant diffusion mechanism (by the fastest diffusion path). The dominant diffusion mechanism depends on several factors, like the temperature, the microstructure and the quality of the interface between the metal and adjacent layers. It is known that the lattice diffusion has the highest activation energy, being the slowest path for mass transport, while the activation energy for diffusion along grain boundaries and interfaces is lower. In general, surfaces have the lowest values of activation energy for electromigration, being the fastest diffusivity paths. It was reported that in polycrystalline Al wires the electromigration takes place along the grain boundaries, even the surface activation energy for diffusion is smaller than for grain boundaries, due to Al has a tendency to protect its surfaces by the formation of aluminium oxide. However, in Cu lines, it is not so evident, because diffusion along interfaces appears as the dominant mechanism [1].

In figure 6.7 (g)-(j) the observed narrowing inside a single grain can be explained by a surface diffusion. The choice of silicon nitride as a substrate material might play a role in enhancement of surface diffusion. In [15, 16] it is reported that nanogaps produced in gold nanobridges with silicon nitride substrates have a size of 5-6 nm, while in [25] it is reported on smaller nanogap sizes in gold structures fabricated on top of silicon oxide substrates. In [15] it is also mentioned that the explanation of difference in nanogap sizes might be due to difference in interaction of gold atoms with the silicon nitride surface compared to silicon oxide or aluminium oxide substrates.

In the experiment shown in figure 6.2 when a tiny constriction with a length of several nanometers is formed (see figure 6.2 (g)), the electric field force on atomic lattice is also significant. The constriction will be the most resistive part of the bridge, so the voltage drop is expected to be at the constriction. Since at the last stage of breakdown the applied voltage is around 200 mV and the length of the constricted part is about 5 nm, the electric field is expected to be around 4×10^5 V/cm. The current density at the constriction is estimated to be 2×10^8 A/cm^2. Comparing to initial configuration of the bridge at the moment when electromigration is observed, the electric field and the current density are around 10^4 V/cm and 5×10^7 A/cm^2, respectively. It is obvious that the Joule heat per unit of volume ($Q=E\cdot j$, E is the electric field and j is the current density) will be higher in case of constriction. Due to this the temperature rise in the constriction area can be also significant, which in turn can create an atomic flow from high temperature regions to low temperature regions. However, we don't observe any melting of material in the constriction during the experiment or material backflow at the moment of breakdown, the electrode tips have a point-like shape in FCE experiments. It indicates that there is a good heat dissipation due to surrounding massive AuPd material around the constriction. To describe the process of material migration at the scale of constriction dimensions in details more investigations are needed.

6.4. Conclusions

We have performed *in situ* (S)TEM investigation of nanogap formation in AuPd NWs (in total 40 nanobridges). We have shown that the mechanism of nanogap formation differs between conventional and feedback-controlled electromigration modes. The average size of the nanogaps made by BRE and FCE technique is 3.5-4 nm and 1.5-2 nm respectively. We have analyzed the time stability of electromigrated nanogaps obtained by both techniques and the changes in the shapes of electrodes and the sizes of the nanogaps were not detected for all fabricated structures after one week.

References

1. C. M. Tan, A. Roy. *Electromigration in ULSI interconnects*. Materials Science and Engineering, 2007, 58, 1-75.

2. J. Lienig. *Electromigration and Its Impact on Physical Design in Future Technologies*. Proc. of the Int. Symposium on Physical Design (ISPD) 2013, 33–44.

3. A. Christou. *Electromigration and Electronic Device Degradation*. John Wiley & Sons Ltd, 1994.

4. A. K. Mahapatro, S. Ghosh, D. B. Janes. *Nanometer Scale Electrode Separation (Nanogap) Using Electromigration at Room Temperature*. IEEE Transactions om nanotechnology, 2006, 5.

5. H. Park, A. K. L. Lim, A. P. Alivisatos, J. Park, P. L. McEuen. *Fabrication of metallic electrodes with nanometer separation by electromigration*. Appl. Phys. Lett., 1999, 75, 301- 303.

6. D. R. Strachan, D. E. Smith, D. E. Johnston, T.-H. Park, M. J. Therien, D. A. Bonnell, A. T. Johnson. *Controlled fabrication of nanogaps in ambient environment for molecular electronics.* Appl. Phys. Lett., 2005, 86, 043109.

7. F. O. Hadeed and C. Durkan. *Controlled fabrication of 1–2nm nanogaps by electromigration in gold and gold-palladium nanowires.* Appl. Phys. Lett., 2007, 91, 123120.

8. B. Gao, E. A. Osorio, K. Babaei Gaven and H. S. J. van der Zant. *Three-terminal electric transport measurements on gold nano-particles combined with ex situ TEM inspection*. Nanotechnology, 2009, 20, 415207.

9. K. Moth-Poulsen and T. Bjørnholm. *Molecular electronics with single molecules in solid-state devices*. Nature Nanotechnology, 2009, 4, 551 – 556.

10. D. L. Klein, P. L. McEuen, J. E. Bowen Katari, R. Roth and A. P. Alivisatos. *An approach to electrical studies of single nanocrystals.* Appl. Phys. Lett., 1996, 68, 2574.

11. D. L. Klein, R. Roth, A. K. L. Lim, A. P. Alivisatos, P. L. McEuen. *A single-electron transistor made from a cadmium selenide nanocrystal*. Nature, 1997, 389, 699.

12. A. Dimonte, D. Perrone, A. Chiodoni, D. Demarchi, P. Civera, G. Piccinini. *NanoLab system for nanoelectronics and sensors*. Nanotechnology, 2010, 2, 372-375.

13. K. O'Neill, E. A. Osorio, and H. S. J. van der Zant. *Self-breaking in planar few-atom Au constrictions for nanometre-spaced electrodes*. Applied Physics Letters, 2007, 90, 13.

14. Z. M. Wu, M. Steinacher, R. Huber, M. Calame, S. J. van der Molen, C. Schönenberger. *Feedback controlled electromigration in four-terminal nanojunctions.* Applied Physics Letters, 2007, 91, 5.

14. Y. Murakami, M. Arita, K. Hamada, Y. Takahashi. *In-Situ Transmission Electron Microscopy Observation of Electromigration in Au Thin Wires*. Journal of Nanoscience and Nanotechnology, 2012, 12, 8741–8745.

15. H. B. Heersche, G. Lientschnig, K. O'Neill, H. S. J. van der Zant, H. W. Zandbergen. *In situ imaging of electromigration-induced nanogap formation by transmission electron microscopy*. Applied Physics Letters, 2007, 91, 072107.

16. D. R. Strachan, D. E. Smith, M. D. Fischbein, et al. *Clean electromigrated nanogaps imaged by transmission electron microscopy*. Nano Letters, 2006, 6, 441-444.

17. F. Prins, T. Hayashi, B. J. A. de Vos van Steenwijk, B. Gao, E. A. Osorio, K. Muraki, H. S. J. van der Zant. *Room-temperature stability of Pt nanogaps formed by self-breaking*. Applied Physics Letters, 2009, 94, 123108.

18. M. Rudneva, B. Gao, F. Prins, Q. Xu, H. S. J. van der Zant, H. W. Zandbergen. *In situ TEM imaging of electromigration in platinum nanowires*. Microscopy and Microanalysis, 2013, 19, 43-48.

19. Camtasia studio. Available from: http://www.techsmith.com/index.html

20. H. W. Zandbergen, R. J. H. A. van Duuren, P. F. A. Alkemade, G. Lientschnig, O. Vasquez, C. Dekker, F. D. Tichelaar. *Sculpting nanoelectrodes with a transmission electron beam for electrical and geometrical characterization of nanoparticles*. Nano Lett. 2005, 5, 549.

21. T. Kozlova, H. W. Zandbergen. *In situ visualization of electromigration in Pt nanobridges at elevated temperatures*. Ultramicroscopy, 2015, 158, 74-80.

22. B. Kießig, R. Schäfer and H. von Löhneysen. *Two-dimensional simulations of temperature and current-density distribution in electromigrated structures.* New J. Phys., 2014, 16, 013017.

23. J. J. Clement. *Electromigration Modeling for Integrated Circuit Interconnect Reliability Analysis*. IEEE Trans. Dev. Mat. Rel., 2001, 1, 33-42.

24. A. S. Budiman, C. S. Hau-Riege, P. R. Besser, A. Marathe, Y.-C. Joo, N. Tamura, J. R. Patel, and W. D. Nix. *Plasticity-Amplified Diffusivity: Dislocation Cores as Fast Diffusion Paths in Cu Interconnects*. Proc. Intl. Reliability Physics Symp., 2007, 122-127.

25. G. Esen and M. S. Fuhrer. *Temperature control of electromigration to form gold nanogap junctions.* Appl. Phys. Lett., 2005, 87, 263101.

CHAPTER 7

In situ TEM formation of a single-crystalline bismuth film on an amorphous substrate

7.1. Introduction

In the past decade, interest in thin bismuth films has increased due to their unique properties in 2D geometry, such as finite-size effects, the quantum confinement effect [1-3] and the high-magnetoresistance effect [4-7]. It has been shown that low-dimensional bismuth can improve thermoelectric efficiency [8-15]. Moreover, recent theoretical [16-18] and experimental [19, 20] studies indicate that a Bi(111) bilayer is a topological insulator having intriguing electronic properties which, in turn, attract even more interest to thin bismuth films.

The physical properties of thin metal films are highly affected by crystalline film imperfections such as grain boundaries (GBs) and grain sizes. Particularly in the case of bismuth, this effect is even stronger because the grain sizes are much smaller than the mean free path of the electrons. Therefore, much attention has been paid to fabricating bismuth thin films on different substrates by various growth techniques, such as molecular beam epitaxy [21-29], pulsed laser deposition [30], thermal evaporation [31-33], electrodeposition [34] and dc sputtering [35, 36] in order to enhance the quality of thin films and produce high-quality monocrystalline bismuth films. Electrodeposition, thermal evaporation and sputter deposition produce polycrystalline Bi films, the grain sizes of which depend on the deposition technique and substrate temperature, and the film quality can be improved by selecting optimal post-annealing conditions. An epitaxial growth of excellent quality can be obtained by molecular beam epitaxy. However, to grow a single-crystalline Bi film with a low density of defects, this fabrication technique requires that single-crystalline substrates of high quality and small lattice mismatch be selected.

In this Chapter we show that it is possible to transform a polycrystalline thin film of Bi into a [111]-oriented single-crystalline area, whereby the unique feature is that the original thickness of the film is maintained and the substrate used in our experiments is amorphous. The single-crystalline area is created by heating the film close to the melting temperature and using an electron beam to melt and, subsequently, cool the film to create a “sandwiched” single-crystalline area. We provide details about grain growth and the process of forming the liquid.

7.2. Experimental

Polycrystalline thin Bi films with thicknesses of 22–25 nm were deposited by electron beam evaporation at room temperature (RT) using a Leybold Heraeus L560 machine. High-purity bismuth (99.99%) was evaporated under vacuum conditions at 10^{-6} mbar with a slow deposition rate of 0.5 Å/s onto the back of the heating chips developed for *in situ* TEM heating experiments. Figure 7.1 (a) is a schematic illustration of a heating chip containing a Pt-heating coil embedded in a 400-nm-thick SiN_x membrane. An optical microphotograph of the heating coil is shown in Figure 7.1 (b), and Figure 7.1 (c) shows the enlarged part of the heater. TEM imaging was performed on 20-nm-thick SiN_x windows, see Figure 7.1 (c). The details of heating chip fabrication for *in situ* TEM studies are described in [37]. Before deposition of bismuth films, all the heating chips for the *in situ* TEM experiments were calibrated by means of a pyrometer. During the deposition process the thickness of the Bi film was controlled *in situ* by a standard gold-coated quartz crystal monitor. After deposition of the bismuth film, the heating chip was placed into an in-house-built TEM heating holder for *in situ* heating experiments. To prevent deep Bi oxidation upon exposure to air, the chip was transferred into the TEM within 1–2 hours.

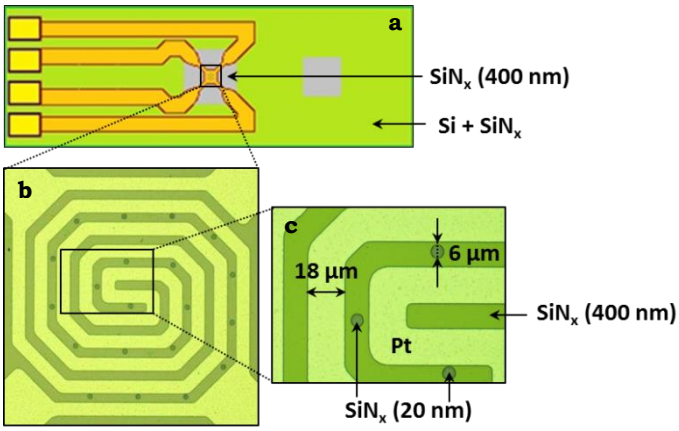

Figure 7.1. (a) A schematic illustration of a heating chip used in *in situ* TEM experiments. The grey areas show the 400-nm-thick SiN membranes. (b) Optical microphotograph of the heating coil. (c) Enlarged area of the heating coil shown in (b).

The *in situ* TEM heating experiments were performed with an FEI Titan microscope operated at 300 keV. Real-time TEM and diffraction pattern (DP) movies showing the polycrystalline film transformation under *in situ* heating and electron beam bombardment were recorded with Camtasia screen recorder software from a FluCam screen and a Gatan camera. TEM images were acquired using a Gatan camera.

7.3. Results

7.3.1. Experiment 1. Modification of a polycrystalline to a monocrystalline Bi film by in situ TEM heating with a focused electron beam

A bright-field TEM micrograph of the as-deposited bismuth film is shown in Figure 7.2 (a). One can see that the bismuth film is initially polycrystalline and consists of grains with well-defined grain boundaries (GBs). At RT the grain sizes of the as-deposited 22-nm-thick film are observed to vary from 30 to 170 nm. A DP (Figure 7.2 (b)) taken from the area presented in Figure 7.2 (a) shows that the initial as-deposited polycrystalline bismuth film consists of [111]-oriented grains rotated with respect to each other. Note that the [111] orientation of the grains is not imposed by the substrate because it is amorphous.

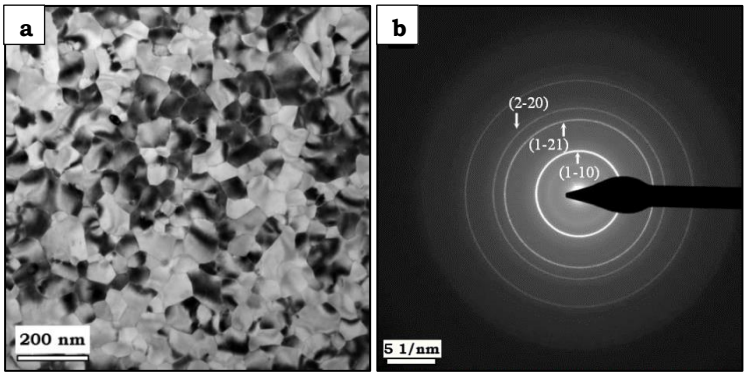

Figure 7.2. (a) Bright-field TEM micrograph of as-deposited bismuth film. (b) Diffraction pattern of as-deposited bismuth film.

We performed *in situ* TEM experiments to investigate polycrystalline Bi film behavior subjected to heating. The temperature of the heating chip was gradually increased until morphological changes were observed in the polycrystalline Bi films. In addition, some of the Bi film was exposed to the electron beam to allow *in situ* observation of the changes. Figure 7.3 shows TEM images of the same Bi-film area acquired at different temperatures during this heating experiment. A TEM image of an as-deposited Bi film taken at RT is shown in Figure 7.3 (a). Figure 7.3 (b) shows a TEM image acquired at 160°C, and no changes can be observed. At 243°C (Figure 7.3 (c)) the polycrystalline film shows small changes: the shapes of some grains and GBs have changed. For example, grains G1 and G2 in Figure 7.3 (a) have become smaller at 243°C, and the grain boundary (GB1) related to G1 has become shorter, see Figure 7.3 (c). At 244.5°C, see Figure 7.3 (d), a contrast change near the triple junctions can be observed: these areas become darker. Increasing the temperature further to 246 and 247.3°C (Figures 7.3 (e) and (f), respectively) leads to similar contrast changes along the GBs, and the widths of the dark contrast areas at the triple junctions increase. Also, nearly each GB band has a dark contrast except low-angle GBs (LAGBs), see Figures 7.3 (e)–(f), where LAGB is a GB between two adjoining grains with a small misorientation angle ($\theta < 11°$). As this misorientation is provided by an array of dislocations in a periodic row, LAGBs have a different contrast in TEM and can be easily distinguished [38]. At 248.6°C (Figure 7.3 (g)) the grains are smaller and roundish in shape, and the dark GB bands have grown wider. With increasing temperature, grain sizes decrease rapidly and most of them disappear, whereas the GB bands expand considerably. When the temperature was increased to 249.7°C, grains and GBs were no longer observable, and the contrast of the entire field of view was nearly homogeneous. At that moment, the temperature was immediately decreased to RT, and a TEM image and a DP (Figures 7.3 (h) and (i)) were taken of this area. Both show that the area is monocrystalline [111]-oriented Bi.

We attribute the changes in the shapes of the grains and GBs to GB melting [39–41]. The melting starts at triple junctions and, as the temperature rises, extends along the GBs, thus forming a molten phase

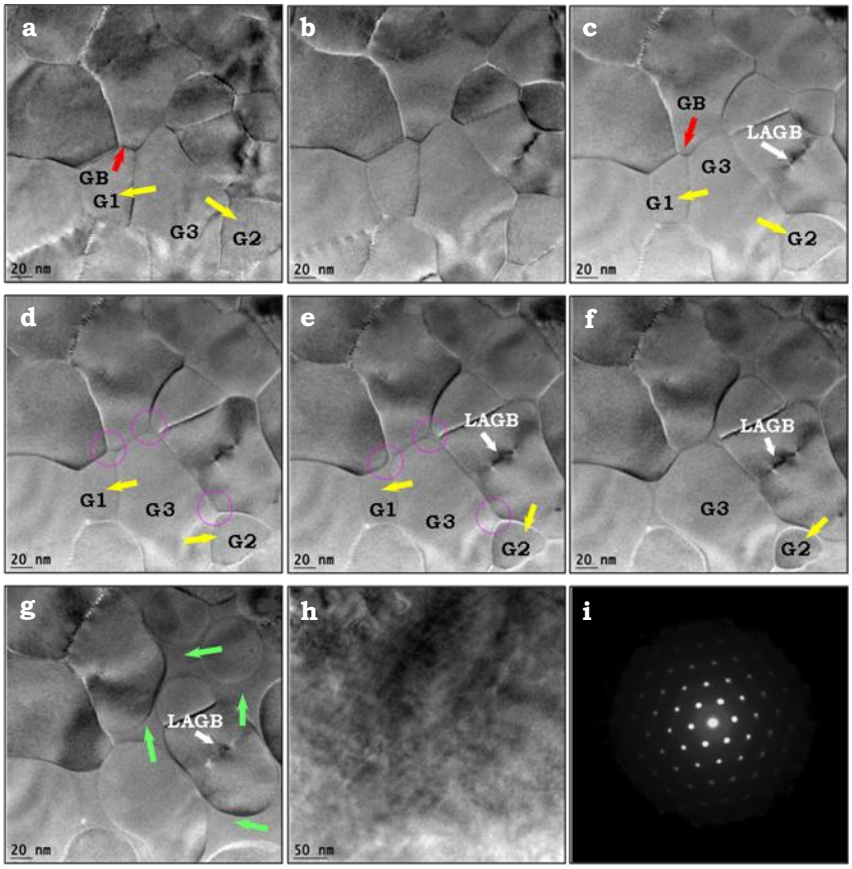

Figure 7.3. TEM images showing the transformation of the bismuth-film area occurring at different temperatures during the heating experiment. (a) TEM image of as-deposited Bi film taken at RT. (b)–(g) Images of the same bismuth film area as in (a) acquired at 160, 243, 244.5, 246, 247.3 and 248.6°C, respectively. (h) TEM image acquired at RT and showing changes in the same field of view that occurred at 249.7°C. (i) DP obtained from (h). Red arrows in (a) and (c) indicate the GBs that undergo changes under heating. Yellow arrows in (a) and (c)–(f) indicate the changes in the grains of interest. Purple circles indicate GB melting, and green arrows indicate the molten phase of Bi.

(Figures 7.3 (e) and (f)). As we increase the temperature, the width of this molten phase along the GBs increases, and the molten phase forms a connected network surrounding almost all the original grains except the ones that have disappeared, see Figure 7.3 (g). The contrast of the molten

phase indicated by green arrows in Figure 7.3 (g) originally indicates a higher-density phase, which agrees well with the fact that liquid Bi has a higher density than solid Bi. Remarkable — and in contrast to the common behavior in grain boundary melting — is that the thickness of the Bi film does not change significantly. This observed phenomenon is relatively unique because thin films are generally metastable in the as-deposited configuration and tend to dewet or agglomerate to form islands when heated even below a film's melting point [42].

To observe the changes in the entire film after the heating experiment, we acquired a TEM image at low magnification, Figure 7.4 (a). The area marked by the yellow circle was exposed to the electron beam. The segment of the film indicated in purple corresponds to the monocrystalline Bi film. Outside this segment, the film remained polycrystalline. Thus, the electron beam obviously affects the microstructure of the Bi film. Figure 7.4 (b) is a HRTEM image of a bismuth film taken from the area indicated by blue square in figure 7.4 (a) and shows that Bi is single crystalline and [111]-orientated.

In Figure 7.4, no Bi film can be observed at the bottom right of the picture (only SiN_x) because there is a slight temperature gradient along the heating chip. As bismuth is very sensitive near its melting temperature, even temperature variations for 0.1–0.3°C can lead to melting and droplet formation.

To determine the melting temperature of a 22-nm-thick Bi film, we performed a heating experiment with and without minor effects of an electron beam by spreading it over an area of 5 µm in diameter. Heating chips were calibrated in order to determine the melting temperature accurately prior to depositing the Bi film. GB melting occurred at 242–244°C and the Bi film collapsed completely at 250.5-251°C, which is approximately 20°C lower than for the bulk Bi and can be attributed to the melting-point depression effect, i.e. the phenomenon of reduction of the melting point of a material with reduction of its size [43]. The decrease in melting temperature can be on the order of tens to hundreds of degrees for metals with nanoscale dimensions [44–47].

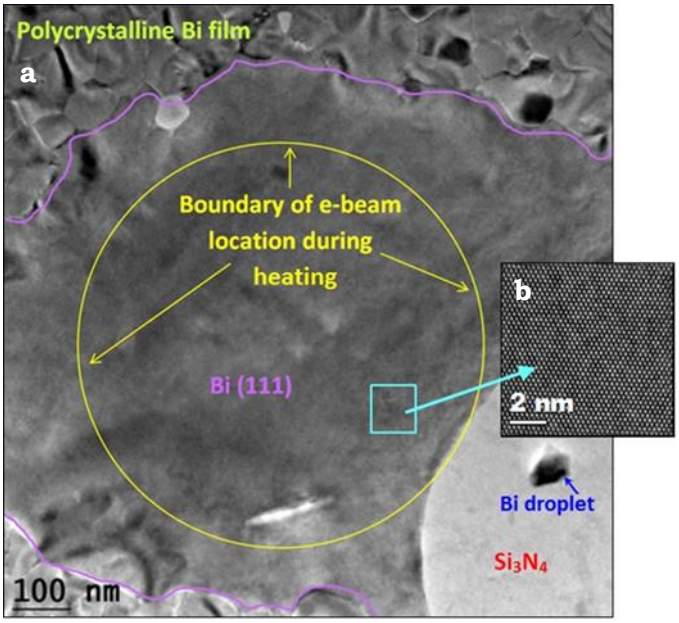

Figure 7.4. (a) TEM image presenting an overview of the area transformed into a [111]-oriented Bi film under heating and electron-beam irradiation. The e-beam position is indicated by the yellow circle. The border between the monocrystalline and the polycrystalline regions of the Bi film is shown in purple. (b) HRTEM image of the Bi film taken of the area indicated by the blue square in (a) and corresponding to [111] orientation.

7.3.2. Experiment 2. Modification of small areas (60–200 nm in diameter) of a polycrystalline to a monocrystalline Bi film by in situ TEM heating and electron beam heating

In this experiment we show that by *in situ* heating and, additionally, focusing the electron beam to smaller diameters, it is possible to change small areas (several grains) of a polycrystalline Bi film into a [111]-oriented monocrystalline film where the electron beam is applied. As in the experiment described in Section 7.3.1, the thickness of the Bi film deposited on the back of the heating chips was 22 nm. The temperature of the heating chip was gradually increased, the electron beam was focused to 200 nm in diameter, and a randomly chosen area of the Bi film was exposed to the electron beam during the heating experiment.

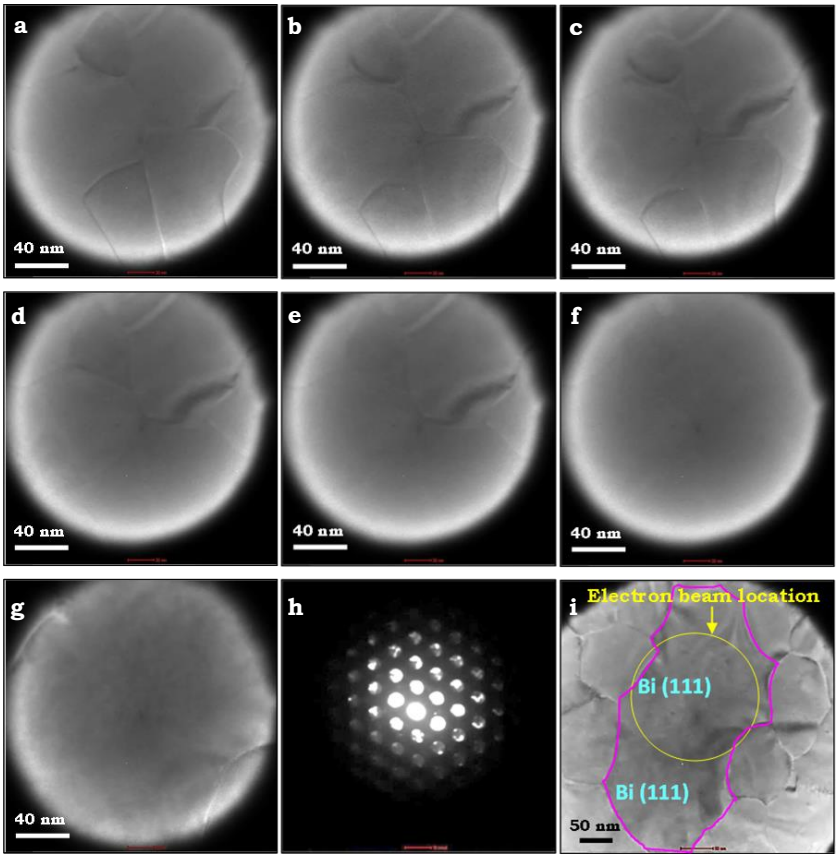

Figure 7.5. TEM images showing the structural changes that occur under *in situ* heating and beam heating conditions. (a) TEM image of the as-deposited Bi film area acquired at RT. (b)–(f) TEM images acquired at 247, 247.5, 248.5, 249.1 and 249.5°C, respectively. (g) Image acquired at RT after Bi-film recrystallization. (h) DP taken from the area shown in (g) corresponding to the [111]-oriented Bi film. (i) TEM image acquired at low magnification to give an overview of the changes in the film. The position of the electron beam during the heating experiment is indicated by a yellow circle.

Figure 7.5 shows TEM images acquired during this experiment. Figure 7.5 (a) is a TEM image of an as-deposited Bi film area at RT. At 247 and 247.5°C we observe the melting of GBs starting at triple junctions, see Figures 7.5 (b) and (c), respectively. A further increase in temperature to 248.5–249.1°C causes some grains to melt and the molten phase surface square to increase, see Figures 7.5 (d) and (e). At 249.5°C we observe no

grains but only a molten phase in the field of view, see Figure 7.5 (f). At this moment the temperature was decreased to RT and the TEM image was acquired (Figure 7.5 (g)). The DP (Figure 7.5 (h)) obtained in the area shown in Figure 7.5 (g) shows that this area is a [111]-oriented Bi film. The TEM image acquired at low magnification (Figure 7.5 (i)) presents an overview of the changes in the film. The position of the electron beam for Figures 7.5 (a)–(g) is indicated by the yellow circle. The area outlined by a purple line is the area of the [111]-oriented film. One can find that outside of this area the film is remained polycrystalline.

In this experiment the temperature of the film is slightly lower (0.1–0.2°C) than in experiment described in Section 7.3.1. This difference might occur for two reasons. First, in this area the grain orientations might accidentally tend to form a single crystal faster. Second, the e-beam current density was approximately 10 times higher in *Experiment 7.3.2* than in *Experiment 7.3.1*. To exclude the fact that we could choose an area with grains that tend to form single crystals rapidly, we performed several similar heating experiments and observed that the transformation occurred every time at the same temperature. Thus, the origin of the temperature difference between these two experiments can be explained by slightly greater e-beam heating due to an increase in the e-beam current density described in Section 7.3.2.

The two experiments shown in Figures 7.3 and 7.5 show that the e-beam causes a local temperature increase. Specimen heating by electron beam is difficult to measure experimentally because of many variables, such as thermal conductivity, thickness, surface condition of the specimen as well as the energy, current and size of the electron beam. In [48] it was shown that the temperature rise in TEM specimens can be very high due to the influence of the electron beam. Particularly in the case of materials with low thermal conductivity, the temperature increase might be significant because the heat dissipation is slow. Owing to this, there is a colder film environment outside the heated area of the film with low thermal conductivity.

In [49] Hobbs calculated the effect of the temperature rise in the specimen depending on thermal conductivity and the electron beam current. From these calculations one can see that, for metals and other good thermal conductors, i.e. for Au k=314 $W \cdot m^{-1} \cdot K^{-1}$, for Cu k=385 $W \cdot m^{-1} \cdot K^{-1}$, and for diamond k=1000 $W \cdot m^{-1} \cdot K^{-1}$, the temperature rise due to the electron beam is very small (≤0.1°C). In the case of bismuth, which has a thermal conductivity of k=7.97 $W \cdot m^{-1} \cdot K^{-1}$ for an electron beam current of 10^{-9}-10^{-10} A, the temperature rise should be approximately 0.2–0.3°C. In addition, Egerton *et al.* [50] estimate that the temperature rise in a carbon film (k≈1.6 $W \cdot m^{-1} \cdot K^{-1}$) with a 5-nA stationary probe when the beam diameter decreases from 1 μm to 1 nm. For these diameters the current density in the probe (1 nm) increases by a factor of 10^6, but the temperature increases only from 0.5 to 1.4 K.

7.3.3. Experiment 3. Diffraction pattern changes during in situ heating and electron-beam bombardment

Several movies of the changes upon heating of the Bi film were recorded in diffraction mode, allowing us to see unambiguously the change from polycrystalline to amorphous/liquid and then into a single-crystalline film. As in the experiments described above, additionally to the MEMS-based heating we focused a beam onto an area 200 nm in diameter of the bismuth film. While increasing the temperature of the heating chip, we recorded the DP movies. Snapshots taken from a DP movie are shown in Figure 7.6. The DP taken at RT is shown in Figure 7.6 (a) and corresponds to an as-deposited polycrystalline Bi film. Figure 7.6 (b) shows a DP image recorded at 246.5°C. Here we observe the presence of a diffusive ring inside the inner ring of DP corresponding to a liquid or amorphous phase due to the start of the GB melting process. Then, temperature increases to 247.2, 247.8, 248.3 and 248.9°C (see Figure 7.6 (c)–(f)) increase the amorphous rings, indicating an increase of the liquid phase areas between the grains. The contrast of diffusive ring diffraction becomes more apparent and some of diffraction spots disappear, which means that some of the grains are transformed into the liquid phase, consistent with the TEM movies. When the temperature was increased to 249.6°C (Figure 7.6 (g)), we observed only

a thick diffusive ring and no crystalline reflections, indicating that only a liquid phase is present. When this was observed, the temperature was immediately (within 1 second) lowered to RT. The DP taken at RT is shown in Figure 7.6 (h), showing that the area is a single-crystalline film. Figure 7.6 (i) represents the overlay result of two DP images taken at RT of an as-deposited Bi film (Figure 7.6 (a)) and after heating (Figure 7.6 (h)). It is clear that this as-grown polycrystalline Bi film is highly textured and consists of [111]-oriented grains rotated with respect to each other.

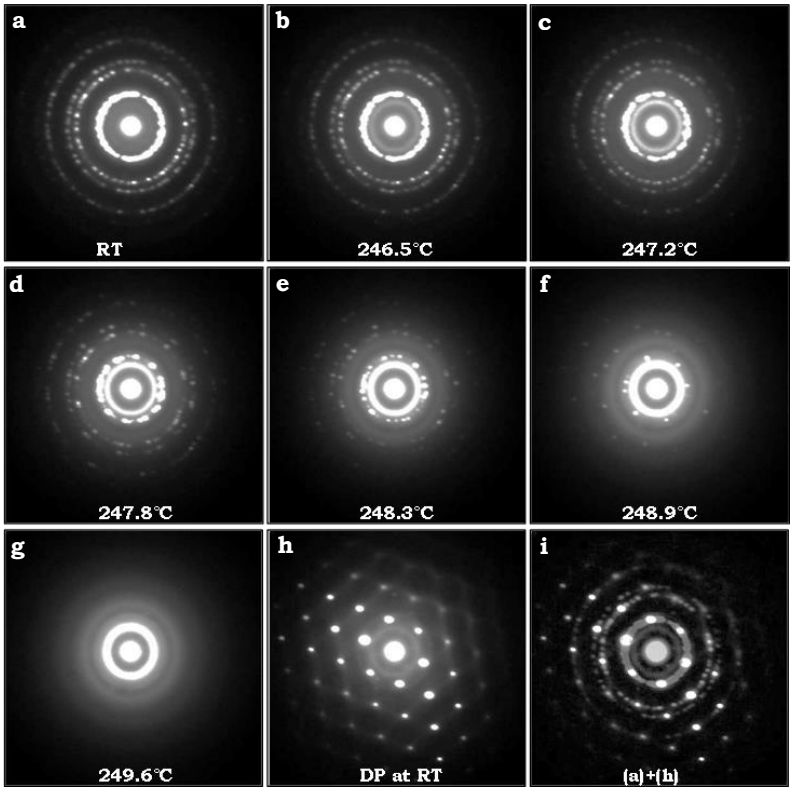

Figure 7.6. DP images taken from a DP movie recorded during a heating experiment with a 200-nm-diameter e-beam focused over the Bi film. (a) DP image acquired at RT corresponding to an as-deposited polycrystalline Bi film. (b)–(g) DP images corresponding to 246.5, 247.2, 247.8, 248.3, 248.9 and 249.6°C, respectively. (g) DP image obtained after immediate temperature decrease from 249.6°C to RT, corresponding to a monocrystalline Bi film with [111] orientation. (i) Result of overlaying two DP images taken at RT of (a) an as-deposited Bi film and (h) after heating.

7.3.4. Experiment 4. Dependence on film orientation with respect to the electron beam

To determine whether the recrystallization process might depend on the orientation of the electron beam with respect to the bismuth film, we repeated the heating experiments with the sample tilted 25°. Figure 7.7(a) shows a TEM image of Bi film area after the recrystallization process during a heating experiment performed at a tilt of 25° with respect to the electron beam. The area indicated by blue line shows the recrystallized area. The yellow circle shows the position of the electron beam during the heating experiment and the DP image taken from that area is shown as the inset in Figure 7.7(b). The 25°-tilt DP shows that the orientation is not [111]. Then, the sample was tilted to 0°, see Figure 7.7 (c). The DP is shown in the inset in Figure 7.7 (d). DP corresponds to the [111]-oriented Bi film, showing that the recrystallization process does not depend on the orientation of the beam with respect to the film.

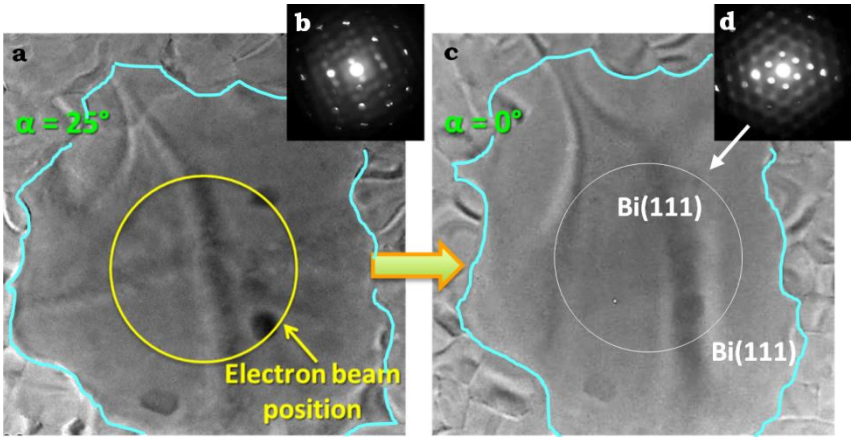

Figure 7.7. (a) TEM image of Bi film area after recrystallization process occurred during the heating experiment performed tilted 25° with respect to the electron beam. The blue lines mark the recrystallized area and the yellow circle marks the position of the electron beam during the heating experiment. (b) The DP image taken from the area of the electron beam position is indicated in (a). (c) TEM image of the same area as (a) acquired after tilting the sample to 0°. (d) DP image obtained from the area indicated by the white circle in (c) corresponds to the [111]-oriented Bi film.

7.3.5. Experiment 5. "Shape memory" effect

- ***Bismuth film***

We performed another heating experiment in which the temperature of the heating chip was increased to the GB melting point, but before the film transforms completely into a homogeneous state and reverses back to lower temperature values — to the point where no GB melting occurs. In this experiment the electron beam was spread over an area of 1 μm in diameter, so the effect of e-beam heating can be neglected. Figure 7.8 shows TEM images obtained during this experiment. Figure 7.8 (a) corresponds to the TEM image showing an as-deposited polycrystalline Bi film heated to 200°C. At this temperature, no GB melting was observed. We gradually increased the temperature to 247.7°C and acquired the TEM image presented in Figure 7.8 (b) showing the GB melting process as the liquid phase network forms around the grains. Small grains transformed into the liquid phase. After we decreased the temperature to 200°C where the molten phase at the GBs has not yet occurred, see Figure 7.8 (c), some of the grains became bigger due to the grain growth process triggered by a temperature change from $T \leq T_{melting}$ to $T \ll T_{melting}$ and back. A second increase in temperature to 248–248.6°C (Figures 7.8 (d) and (e)) caused the molten GBs to return to almost the same positions as in Figure 7.8 (b). The TEM image acquired after the second decrease in temperature to 200°C is presented in Figure 7.8 (f). The grain size is increased compared to Figure 7.8 (c) obtained after the first drop in temperature; most of the GBs had retracted almost to their previous positions after the temperature drop. A further increase in temperature to 249.1–249.5°C, see Figures 7.8 (g) and (h), led to a liquid phase increment and subsequently all grains transformed into the liquid phase. A temperature drop to 200°C resulted in significant grain growth, which can be observed in Figure 7.8 (i). A reiterated increase in temperature to 250.4°C caused the bismuth to melt completely and form droplets.

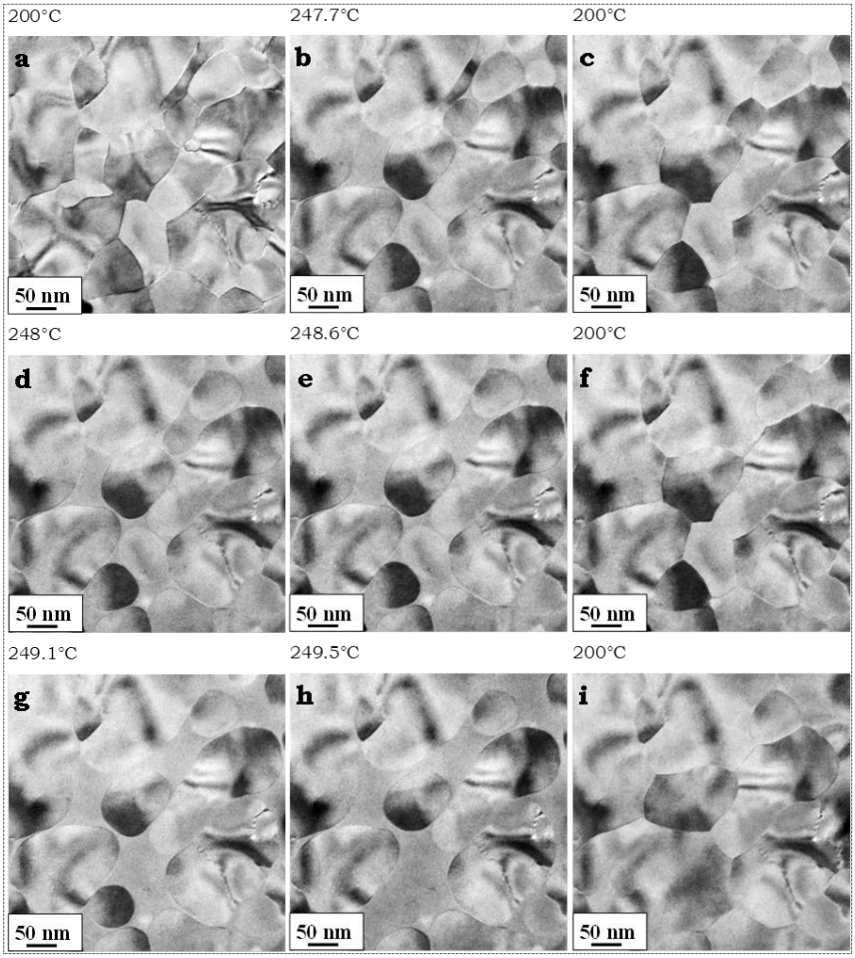

Figure 7.8. TEM images obtained during an *in situ* heating experiment. (a) TEM image shows the as-deposited polycrystalline Bi film acquired at 200°C. (b) TEM image of the Bi film showing the GB melting process and the formation of a liquid phase network surrounding the grains starting at 247.7°C. (c) TEM image of the same Bi film area acquired after decreasing the temperature to 200°C. (d)–(e) Images of the Bi film obtained at 248 and 248.6°C, respectively, and showing a return of molten GBs to almost the same positions as in (b) as well as grains, except those that disappeared due to the slight temperature increase. (f) TEM image acquired during the second decrease in temperature to 200°C. (g)–(h) TEM images acquired during the subsequent increase in temperature to 249.1 and 249.5°C, respectively, and showing the increment of the Bi liquid phase. (i) TEM image obtained after the temperature decrease to 200°C.

To show graphically the evolution of GBs after reiterated temperature increases from $T \ll T_{melting}$ to $T \leq T_{melting}$, we have drawn the position of GBs on TEM images presented in Figures 7.8 (a), (c) and (f). These TEM images with indicated GBs positions are shown in Figures 7.9 (a)–(c), respectively. Figure 7.9 (d) is a result of overlaying the GBs drawn from the three images in Figures 7.9 (a)–(c) without the background; the positions of the GBs are shown in purple, blue and green, respectively.

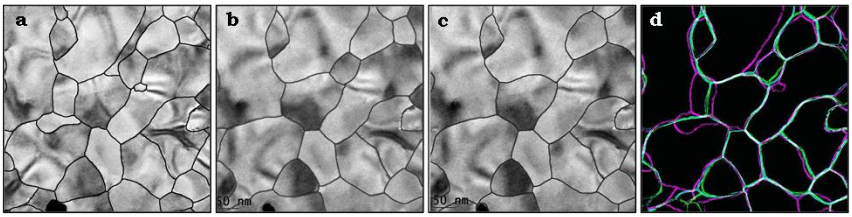

Figure 7.9. (a)–(c) TEM images with the indicated GBs positions corresponding to the TEM images in Figure 7.8 (a), (c) and (f), respectively. (d) Result of overlaying images (a)–(c) without the background; the positions of the GBs are shown in purple, blue and green, respectively.

When the temperature is decreased to lower values, the GBs (which are still present) return almost to their previous positions. This effect might take place due to the presence of a thin bismuth oxide layer formed during exposure to air after deposition. As the GB has an extremely disordered structure, the oxidation process in such regions is faster. During heating, some of the GBs move intensively and small crystals disappear, which means that oxidation of GBs is not complete because GBs can continue to move. This is illustrated schematically in Figure 7.10.

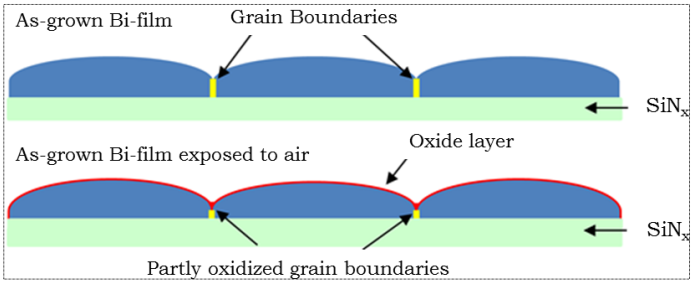

Figure 7.10. Schematic illustration of GBs and Bi film oxidation after exposure to air.

The melting point of bismuth oxide is much higher than for pure bismuth, which might cause a very thin liquid layer to reach several hundred nanometers in diameter when approaching the melting point of pure bismuth by *in situ* heating and electron beam exposure.

- ***Bismuth film covered with Al_2O_3***

We performed the following experiment to confirm the assumption that an oxide layer forming on top of the Bi film exposed to air can be the main factor for achieving a homogeneous and monocrystalline film area under the heating and electron-beam effect. During the e-beam evaporation process we can load more than one target and thus deposit more than one material during the same cycle. Therefore, we deposited a 23-nm-thick Bi film and covered it with a 20-nm-thick layer of Al_2O_3 instead of forming a bismuth oxide layer. We performed the same heating experiment with the electron beam spread over an area of 1 μm in diameter.

TEM images obtained during this experiment are presented in Figure 7.11. Figure 7.11 (a) shows a TEM image of the as-deposited Bi film with an Al_2O_3 layer heated to 200°C. As in the experiment discussed above, no GB melting was observed at this temperature. We gradually increased the temperature to the point where we observed the GB melting process and the formation of a liquid phase network surrounding the grains, see Figures 7.11 (b) and (c). After some of the grains transformed into the liquid phase, we decreased the temperature to 200°C (Figure 7.11 (d)) in order to observe the behavior of the GBs where no melting occurred. Some of the grains became larger by being transferred into the liquid phase of bismuth at $T \approx T_{melting}$ and, upon cooling, this liquid phase was recrystallized. A reiterated increase in temperature from 248.7 to 249.8°C (Figures 7.11 (e)–(g)) resulted in a further increment of the liquid phase and a complete melting of the GBs. When the area of observation became homogeneous with no GBs remaining at 250°C, the temperature was immediately decreased to 200°C, see Figure 7.11 (h).

The DP taken from this area is shown in Figure 7.11 (i) and corresponds to the [111]-oriented Bi film. The slight misorientation from the perfect [111] zone in DP is probably due to the stress caused by the thermal

treatment. It should also be noted that the contrast inhomogeneity in Figure 7.11 (i) can be due to the difference in thermal expansions of bismuth and silicon nitride. Heating or cooling causes stress in the film, which can be compressive or tensile. Upon heating it is compressive.

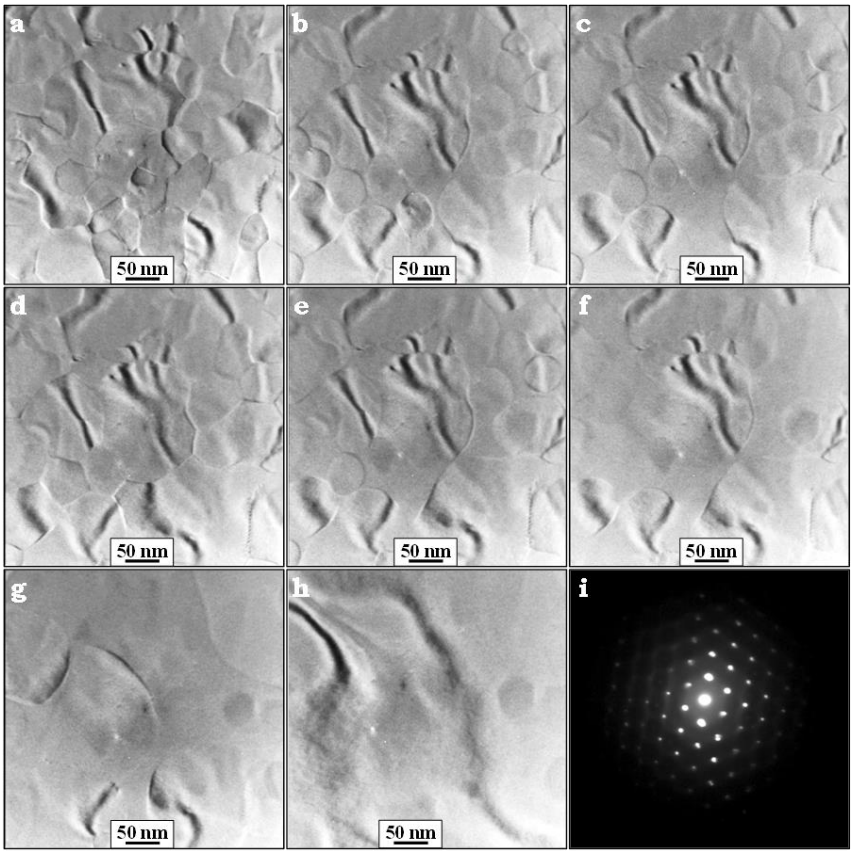

Figure 7.11. TEM images obtained during *in situ* heating of a 23-nm-thick Bi film covered with a 10-nm-thick layer of Al_2O_3. (a) TEM image of as-deposited layers heated to 200°C. (b), (c) TEM images acquired at 248 and 248.5°C, respectively. (d) TEM image of a Bi film acquired after decreasing the temperature to 200°C. (e)–(g) TEM images showing changes in the Bi film during the second increase in temperature to 248.7, 249.3 and 249.8°C, respectively. (h) TEM image of a homogeneous monocrystalline Bi layer. (h) DP obtained from the area in (h) corresponding to the [111]-oriented Bi film.

In this experiment we also observed grain growth in the Bi film when the temperature was decreased from $T \leq T_{melting}$ to $T \ll T_{melting}$ in intermediate steps of heating. Both experiments described in this section confirm the assumption that the oxide layer on the Bi film plays the key role in achieving a homogeneous and monocrystalline pancake-shaped film area in these *in situ* TEM heating experiments.

7.3.6. Experiment 6. Bismuth oxide reduction treatment

To observe the behavior of a Bi film without a thin oxide layer, we deposited a 22-nm-thick Bi film onto the back of the heating chip designed for vacuum transfer to the TEM holder. The vacuum transfer holder enables us to conduct gas treatment experiments at elevated temperatures in a gas supply system outside the TEM and, therefore, allows us to deliver a sample directly to the TEM column under vacuum or controlled gas conditions, thus preventing any interaction with the outside environment. After Bi deposition, the heating chip was placed into the vacuum transfer TEM holder and the bismuth oxide reduction treatment was performed in a H_2 atmosphere with 1 bar of gas pressure at 60-80°C for 1 hour in a homemade gas supply system outside the TEM. Next, the reaction chamber was pumped to vacuum and, after 10 minutes of pumping, the transfer holder was sealed to place the sample in vacuum. Then, the holder was transferred to the TEM within 5-7 minutes without exposure to ambient air.

TEM images acquired during this heating experiment are shown in Figure 7.12. In this experiment the e-beam was spread over an area of 1 μm in diameter. Figure 7.12 (a) is a TEM image obtained at RT. Figure 7.12 (b) shows a TEM image obtained at 245.6°C from the same area as in Figure 7.12 (a). In Figure 7.12 (b) we observe both a partial melting of GBs and hole formation (white spots in the TEM image) in the film starting at triple junctions. At 246.7°C (Figure 7.12 (c)) and 248.4°C (Fgure 7.12 (d)) the formed holes expanded and new holes formed; all GBs became molten. At 249.3°C we observed that the molten (liquid) phase prevailed in the field of view and that the number of holes had increased, see Figure 7.12 (e). An increase in temperature to 249.5°C caused the Bi film to collapse, see Figure 7.12 (f).

This experiment showed that, after the bismuth oxide reduction treatment, the bismuth film behaves completely differently than in the previous experiments. Thus we assume there is no layer of bismuth oxide left on the Bi film. In previous experiments, no holes were present in the Bi films, even when some of the films were kept in the molten state for several seconds, whereas in this experiment the holes formed at the triple points even at a temperature insufficiently high for all GBs to become molten.

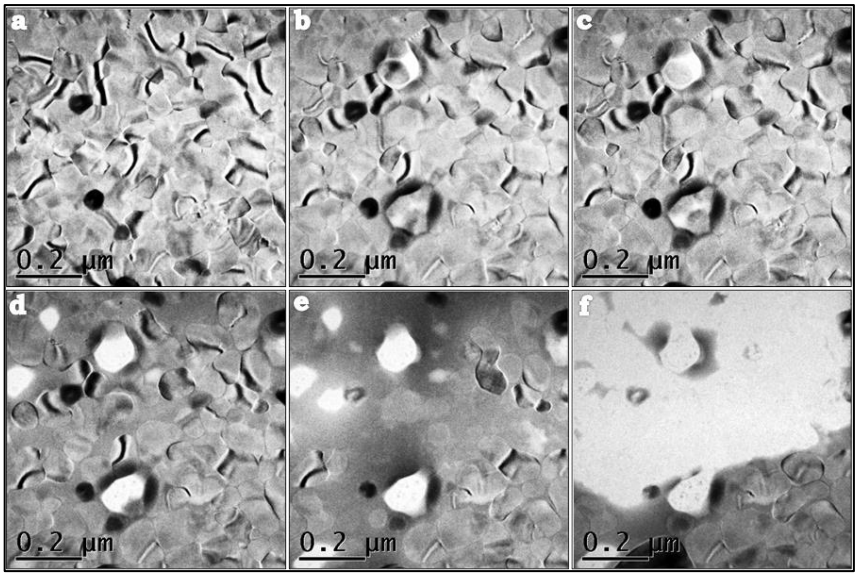

Figure 7.12. TEM images acquired during experiment 6. (a)–(f) TEM images taken from the same area of the Bi film and acquired at RT, 245.6, 246.7, 248.4, 249.3 and 249.5°C, respectively.

7.4. Discussion

We have performed a range of heating experiments with additional local electron-beam heating of polycrystalline Bi films. We estimate that, for the experiments described in Sections 7.3.1 and 7.3.2, the local temperature increase due to the electron beam effect is in the range of 0.1–0.2°C when the electron beam diameter is changed from 600 to 200 nm (for a 5-nA e-beam current and 200 and 600-nm e-beam diameters, the dose is 10^6 and $1{,}1 \cdot 10^5$ electrons/nm^2·sec, respectively). All as-prepared Bi films

show only [111]-oriented grains with a grain size ranging from 30 to 170 nm. We studied the behavior of thin Bi films under *in situ* heating in TEM with some additional local heating by an e-beam but without irradiation. During e-beam heating, the nanostructural changes were always compared with changes in nearby areas not irradiated by the e-beams. Upon being heated above 242°C, the shapes of the grains and GBs change due to GB melting, which starts at triple junctions and, as the temperature increases, the liquid phase extends and widens along the GBs, forming a connected network surrounding almost all the original grains except those that had transformed completely to the molten phase. Electron diffraction confirms the molten (or amorphous) phase at the grain boundaries. When we next increase the temperature accurately with steps of 0.1°C every 1–2 seconds and when no grains or GBs are observed in the field of view, which is nearly homogeneous in contrast, we immediately decrease the temperature to RT. The electron diffraction patterns showed that the area quenched from the molten phase is always monocrystalline and [111]-oriented, whereas the surrounding non-e-beam-irradiated film is polycrystalline. This clearly shows that the e-beam causes a local increase in temperature in the material. This local melting can be controlled very well by the e-beam, which must be related to the relatively low thermal conductivity of Bi because such behavior is not observed for metals with normal or high thermal conductivity. When the e-beam is spread over an area of 1 μm in diameter as described in Section 7.3.5, the behavior of the Bi film within the e-beam-irradiated area is similar to that outside it. For this condition, gradually increasing the temperature with a minor influence of the electron beam shows that all regions of the Bi film behave similarly: several increases in temperature lead to significant GB melting and decreases in temperature show no GB melting, but in both cases grain growth has occurred (see Figures 7.8 (f) and (i)) and is comparable to that observed in the polycrystalline part of the Bi film outside the e-beam location in the experiments described in Secitons 7.3.1 and 7.3.2.

The behavior of thin Bi films is quite different from that of other metal films on amorphous substrates at higher temperatures [51–53]: for Bi films there is no dewetting and no significant change in thickness. Normally, thin solid films are instable in as-deposited configurations and,

when heated, tend to dewet and agglomerate to form islands. This process can take place even far below the melting temperature of the metal where the film remains in its solid state. The driving force for solid-state dewetting is surface-energy minimization, and surface self-diffusion and GB diffusion are considered to be the main transport mechanisms [42, 52].

In the case of a thin polycrystalline Bi film, we assume there are several crucial factors that prevent the grain growth normally observed in metal thin films: (a) the as-prepared film is already [111]-textured, (b) the surface of Bi is covered with a thin bismuth oxide layer and (c) surface diffusion of Bi on the [111] surface and in Bi [111]-bismuth oxide interface is probably very small. Concerning (a), the [111] surface is very stable, which is also evident from the fact that Bi cleaves very easily along the (111) planes. Thus the driving force for further grain coarsening is relatively small. Concerning (b), with either a Bi oxide layer or an Al_2O_3 layer on the Bi film, we see that the Bi film remains confined between the oxide layer on top and the SiN membrane beneath the Bi film. A thin bismuth oxide layer was formed on top of bismuth by exposing the film to air after deposition. The Al_2O_3 layer was deposited with the same equipment as for the Bi layer, so there was no Bi oxide layer present in this case. If we remove the native Bi oxide layer by heating it in hydrogen, the Bi film does show changes in its thickness and dewetting, similar to other metals but to a lesser extent. Concerning (c), we suggest that the surface diffusion of Bi atoms on a (111) surface is slow. In particular, we think that confining the top and bottom layers prevents surface (interface) diffusion in these films.

In the absence of a coating on the Bi surface (see Figure 7.12 in Section 7.3.6) the film's behavior is quite different. For temperatures that were insufficient for all GBs to become molten (Figure 7.12 (b)) we observed the formation of several holes in the film, and these holes started to form in triple junctions. This can be due to a high surface-to-volume ratio. A thin solid film, when heated, may develop holes and eventually transform into shapes having lower surface-to-volume ratios, and this process can occur well below the melting point of the material [54]. In addition, the formation of holes occurs together with a strong increase in mass-thickness contrast around the holes, which might be due to surface diffusion not limited by the

bismuth oxide layer. On the other hand, an increase in mass-thickness contrast is clearly observed only around formed holes.

Another explanation of the different behaviors of polycrystalline Bi films with and without (after oxygen reduction in H_2 gas) the presence of native oxide might be the following. In [55] Copel *et al.* describe their work on the growth of epitaxial layers of Si/Ge/Si(001). A fundamental obstacle to growing an A/B/A heterostructure is the fact that, because the growth mode of epitaxial layers is determined by the balance between surface, interface and film free energies, if A wets B, B will not wet A. Copel *et al.* proposed the use of a segregating surfactant to reduce the surface free energies of A and B to suppress island formation. Normally Ge does not wet Si so that it exhibits island-type growth, but the surface energy was lowered by applying an atomically thin layer of As. Arsenic does not alloy with Ge or Si and stays at the surface, thus inducing wetting of Ge and epitaxial growth. Copel *et al.* demonstrated this by growing Si/Ge/Si(001) with a monolayer of As. In our case it is likely that oxygen serves the same purpose of lowering the surface energy of the Bi film. If the surface energy of SiN is greater than the sum of the surface energy of Bi plus the interface energy Bi/SiN, we should expect non-wetting. This is indeed what we observe when we reduce Bi in hydrogen. If oxygen reduces the Bi surface energy sufficiently that the sum of this plus the interface energy becomes less than the surface energy of SiN, then we should observe wetting.

The electron-beam-induced heating can be estimated fairly well because the melting of the illuminated area can be compared to that of the areas not exposed to the electron beam, or when a low beam intensity is used. According to our experiments, the estimation of e-beam-induced heating is about 0.8–1.5°C. Note that the effect of electron-beam heating is strong for Bi compared to other metals because its thermal conductivity is low.

In addition, the thermal stress induced by the different thermal expansion properties of bismuth and silicon nitride should be considered. The coefficient of thermal expansion for bismuth is about 4 times higher than that of silicon nitride. This implies that upon heating, the expansion of Bi is restricted by the SiN substrate and thus will be under compression.

The Bi film can release this compressive stress by forming hillocks. However, we did not observe any hillocks during heating to almost the melting point. The reason might lie in the fact that the higher density of liquid Bi can reduce the compressive stress. On the other hand, the difference in the densities of solid (9.78 g/cm^3) and liquid (10.05 g/cm^3) bismuth is not significant. This means that the higher contrast observed at the molten GBs might also be due to the bulging of the liquid bismuth between the adjacent grains that are also expanded at the melting temperature of the GBs.

7.5. Conclusions

In this chapter we showed that thin polycrystalline Bi films can be modified into [111]-oriented monocrystalline films by *in situ* TEM heating and electron-beam bombardment with the energy of electrons 300 keV, whereby a unique feature is that the original thickness of the film is maintained. The single-crystalline area is created by heating the film close to the melting temperature and using an electron beam to achieve local melting. The film thickness is maintained by confining it with SiN on one side and with Bi oxide or Al_2O_3 on the other side. In addition, we showed that bismuth films behave differently if no capping Bi-oxide layer is present, a configuration in which dewetting takes place and the film collapses when heated under similar conditions.

References

1. D. Gekhtamn, Z. B. Zhang, D. Adderton, M. S. Dresselhaus and G. Dressehaus. *Electrostatic force spectroscopy and imaging of Bi wires: Spatially resolved quantum confinement*. Phys. Rev. Lett., 1999, 82, 3887.

2. Z. Zhang, X. Sun, M. S. Dresselhaus, J. I. Ying, J. Heremans. *Electronic transport properties of single-crystal bismuth nanowire arrays*. Phys. Rev. B, 2000, 61, 4850.

3. T. Hirahara, T. Nagao, I. Matsuda, G. Bihlmayer, E. V. Chulkov, Yu. M. Koroteev, S. Hasegawa. *Quantum well states in ultrathin Bi films: Angle-*

resolved photoemission spectroscopy and first-principles calculations study. Phys. Rev. B, 2007, 75, 035422.

4. K. Liu, C. L. Chien, P. C. Searson and K. Y. Zhang. *Structural and magneto-transport properties of electrodeposited bismuth nanowires*. Appl. Phys. Lett., 1998, 73, 1436.

5. S. Cho, Y. Kim, A. Freeman, G. Wong, J. Ketterson, L. Olafsen, I. Vurgaftman, J. Meyer, C. Hoffman. *Large magnetoresistance in postannealed Bi thin films*. Appl. Phys. Lett., 2001, 79, 3651.

6. C. L. Chien, F. Y. Yang, Kai Liu, D. H. Reich and P. C. Searson. *Very large magnetoresistance in electrodeposited single-crystal Bi thin films*. J. Appl. Phys., 2000, 87, 4659.

7. F. Y. Yang, K. Liu, K. Hong, D. H. Reich, P. C. Searson, C. L. Chien. *Large magnetoresistance of electrodeposited single-crystal bismuth thin films*. Science, 1999, 284, 1335.

8. L. D. Hicks, T. C. Harman, M. S. Dresselhaus. *Use of quantum-well superlattices to obtain a high figure of merit from nonconventional thermoelectric materials*. Appl. Phys. Lett., 1993, 63, 3230.

9. L. D. Hicks, M. S. Dresselhaus. *Thermoelectric figure of merit of a one-dimensional conductor*. Phys. Rev. B, 1993, 47, 16631.

10. Y. M. Lin, O. Rabin, S. B. Cronin, J. Y. Ying. *Semimetal–semiconductor transition in $Bi_{1-x}Sb_x$ alloy nanowires and their thermoelectric properties*. Appl. Phys. Lett., 2002, 81, 2403.

11. L. D. Hicks, M. S. Dresselhaus. *Effect of quantum-well structures on the thermoelectric figure of merit*. Phys. Rev. B, 1993, 47, 12727.

12. J. P. Heremans, C. M. Thrush, D. T. Morelli, M. C. Wu. *Thermoelectric Power of Bismuth Nanocomposites*. Phys. Rev. Lett., 2002, 88, 216801.

13. Y. M. Lin, X. Z. Sun, M. S. Dresselhaus. *Theoretical investigation of thermoelectric transport properties of cylindrical Bi nanowires*. Phys. Rev. B, 2000, 62, 4610.

14. A. L. Prieto, M. M. Gonzalez, J. Keyani, R. Gronsky, T. Sands, A. M. Stacy. *The Electrodeposition of High-Density, Ordered Arrays of $Bi_{1-x}Sb_x$ Nanowires*. J. Am. Chem. Soc., 2003, 125, 2388.

15. M. S. Dresselhaus, Z. Zhang, X. Sun, J. Ying, J. P. Heremans, G. Dresselhaus, et al. *Prospects for Bismuth Nanowires as Thermoelectrics*. Material Research Society Symposium Proceedings, 1999, 545, 215.

16. Z. Liu, C. X. Liu, Y. S. Wu, W. H. Duan, F. Liu, J. Wu. *Stable Nontrivial Z2 Topology in Ultrathin Bi (111) Films: A First-Principles Study.* Phys. Rev. Lett., 2011, 107, 136805.

17. S. Murakami. *Quantum Spin Hall Effect and Enhanced Magnetic Response by Spin-Orbit Coupling*. Phys. Rev. Lett., 2006, 97, 236805.

18. M. Wada, S. Murakami, F. Freimuth and G. Bihlmayer. *Localized edge states in two-dimensional topological insulators: Ultrathin Bi films*. Phys. Rev. B: Condens. Matter Mater. Phys., 2011, 83, 121310.

19. C. Sabater, D. Gosa´lbez-Martı´nez, J. Ferna´ndez-Rossier, J. G. Rodrigo, C. Untiedt, J. J. Palacios. *Topologically Protected Quantum Transport in Locally Exfoliated Bismuth at Room Temperature*. Phys. Rev. Lett., 2013, 110, 176802.

20. T. Hirahara, G. Bihlmayer, Y. Sakamoto, M. Yamada, H. Miyazaki, S. Kimura, S. Blugel, S. Hasegawa. *Interfacing 2D and 3D Topological Insulators: Bi(111) Bilayer on Bi_2Te_3*. Phys. Rev. Lett., 2011, 107, 166801.

21. D. L. Partin, J. Heremans, D. T. Morelli, C. M. Thrush, C. H. Olk, and T. A. Perry. *Growth and characterization of epitaxial bismuth films*. Phys. Rev. B, 1988, 38, 3818.

22. C. A. Hoffman, J. R. Meyer, F. J. Bartoli, A. Di Venere, X. J. Yi, C. L. Hou, H. C. Wang, J. B. Ketterson, G.K. Wo. *Semimetal-to-semiconductor transition in bismuth thin films*. Phys. Rev. B, 1993, 48, 11431.

23. T. Hirahara, G. Bihlmayer, Y. Sakamoto, M. Yamada, H. Miyazaki, S.-I. Kimura, S. Blugel, and S. Hasegawa. *Interfacing 2D and 3D Topological Insulators: Bi(111) Bilayer on Bi_2Te_3*. Phys. Rev. Lett., 2011, 107, 166801.

24. M. Chen, J.-P. Peng, H.-M. Zhang, L.-L. Wang, K. He, X.-C. Ma, and Q.-K. Xue. *Molecular beam epitaxy of bilayer Bi(111) films on topological insulator Bi_2Te_3: A scanning tunneling microscopy study*. Appl. Phys. Lett., 2012, 101, 081603.

25. F. Yang, L. Miao, Z. F. Wang, M.-Y. Yao, F. Zhu, Y. R. Song, M.-X. Wang, J.-P. Xu, A. V. Fedorov, Z. Sun, G. B. Zhang, C. Liu, F. Liu, D. Qian,

C. L. Gao, and J.-F. Jia. *Spatial and Energy Distribution of Topological Edge States in Single Bi(111) Bilayer*. Phys. Rev. Lett., 2012, 109, 016801.

26. S. H. Kim, K.-H. Jin, J. Park, J. S. Kim, S.-H. Jhi, T.-H. Kim, and H. W. Yeom. *Edge and interfacial states in a two-dimensional topological insulator: Bi(111) bilayer on Bi_2Te_2Se*. Phys. Rev. B, 2014, 89, 155436.

27. K. Zhu, L. Wu, X. Gong, S. Xiao, S. Li, X. Jin, M. Yao, D. Qian, M. Wu, J. Feng, Q. Niu, F. de Juan, D.-H. Lee. *The emergence of topologically protected surface states in epitaxial Bi(111) thin films.* arXiv.org, e-Print Arch., Condens. Matter, 2014, arXiv:1403.0066.

28. K. Ishioka, M. Kitajima. *Ultrafast phonon dynamics of epitaxial atomic layers of Bi on Si(111)*. Phys. Rev. B, 2015, 91, 125431.

29. S. Xiao, D. Wei, X. Jin. *Bi(111) Thin Film with Insulating Interior but Metallic Surfaces*. Phys. Rev. Lett., 2012, 109, 166805.

30. M. O. Boffoue´, B. Lenoir, H. Scherrer, A. Dauscher. *Pulsed laser deposition of bismuth in the presence of different ambient atmospheres*. Thin Solid Films, 1988, 322, 132.

31. X. Du, A. F. Hebard. *Large magnetoresistance of bismuth/gold films thermally deposited onto glass substrates*. Appl. Phys. Lett., 2003, 82, 2293.

32. N. Z. El-Sayed. *Physical characteristics of thermally evaporated Bismuth thin films*. Vacuum, 2006, 80, 860.

33. L. Kumari, S.-J. Lin, J.-H. Lin, Y.-R. Ma, P.-C. Lee, Y. Liou. *Effects of deposition temperature and thickness on the structural properties of thermal evaporated bismuth thin films*. Applied Surface Science, 2007, 253, 5931.

34. F. Y. Yang, K. Liu, C. L. Chien, P. C. Searson. *Large Magnetoresistance and Finite-Size Effects in Electrodeposited Single-Crystal Bi Thin Films*. Phys. Rev. Lett., 1999, 82, 3328.

35. J. C. G. de Sande, T. Missana, C. N. Afonso. *Optical properties of pulsed laser deposited bismuth films*. J. Appl. Phys., 1996, 80, 7023.

36. J.-H. Hsu, Y.-S. Sun, H.-X. Wang, P.C. Kuo, T.-H. Hsieh, C.-T. Liang. *Substrate dependence of large ordinary magnetoresistance in sputtered Bi films*. J. Magn. Mater., 2004, 272, 1769.

37. M. A. van Huis, N. P. Young, G. Pandraud, J. F. Creemer, D. Vanmaekelbergh, A, I. Kirkland, H. W. Zandbergen. *Atomic Imaging of Phase*

Transitions and Morphology Transformations in Nanocrystals. Advanced materials, 2009, 21, 4992.

38. P. Lejček. *Grain Boundaries: Description, Structure and Thermodynamics*. Springer Series in Materials Science, 2010, 136, 5-24.

39. Q. S. Mei, K. Lu. *Melting and superheating of crystalline solids: From bulk to nanocrystals.* Pr. in Mat. Science, 2007, 52, 1175.

40. A. M. Alsayed, M. F. Islam, J. Zhang, P. J. Collings, A. G. Yodh. *Premelting at Defects Within Bulk Colloidal Crystals*. Science, 2005, 309, 1207.

41. P. N. Pursey. *Freezing and Melting: Action at Grain Boundaries*. Science, 2005, 309, 1198.

42. C. V. Thompson. *Solid-State Dewetting of Thin Films*. Annu. Rev. Mater. Res., 2012, 42, 399.

43. N. T. Gladkikh, S. I. Bogatyrenko, A. P. Kryshtal, R. Anton. *Melting point lowering of thin metal films (Me = In, Sn, Bi, Pb) in Al/Me/Al film system.* Applied Surface Science, 2003, 219, 338.

44. J. Sun, S. L. Simon. *The melting behavior of aluminum nanoparticles. Thermochimica* Acta, 2007, 463, 32.

45. A. F. Lopeandia, J. Rodriguez-Viejo. *Size-dependent melting and supercooling of Ge nanoparticles embedded in a SiO2 thin film*. Thermochimica Acta, 2007, 461, 82.

46. M. Takagi. *Electron-Diffraction Study of Liquid-Solid Transition of Thin Metal Films*. J. Phys. Soc. Jpn., 1954, 9, 359.

47. S. L. Lai, J. Y. Guo, V. Petrova, G. Rammath and L. H. Allen. *Size-Dependent Melting Properties of Small Tin Particles: Nanocalorimetric Measurements*. Phys. Rev. Lett., 1996, 77, 99.

48. B. Gale and K. F. Hale. *Heating of metallic in an electron microscope*. Brit. J. Appl. Phys., 1961, 12, 115.

49. L. W. Hobbs, J. I. Goldstein, D. C. Joy, J. J. Hren. *Introduction to Analytical Electron Microscopy*. Plenum Press New York, 1979, 437.

50. R. F. Egerton, P. Li, M. Malac. *Radiation damage in the TEM and SEM*. Micron, 2004, 35, 399.

51. C. M. Muller, R. Spolenak. *Microstructure evolution during dewetting in thin Au films*. Acta Materialia, 2010, 58, 6035.

52. O. Kovalenko, J. R. Greer, E. Rabkin. *Solid-state dewetting of thin iron films on sapphire substrates controlled by grain boundary diffusion*. Acta Materialia, 2013, 61, 3148-3456.

53. F. Niekiel, P. Spiecker, S. M. Kraschewski, B. Butz, E. Spiecker. *The process of solid-state dewetting of Au thin films studied by in situ scanning transmission electron microscopy*. Acta Materialia, 2015, 90, 118.

54. E. Jiran, C. V. Thompson. *Capillary instabilities in thin, continuous films*. Thin Solid Films, 1992, 208, 23.

55. M. Copel, M. C. Reuter, E. Kaxiras, R. M. Tromp. *Surfactants in Epitaxial Growth*. Phys. Rev. Lett., 1989, 63, 632-635.

Summary

In situ TEM electrical measurements of metal and semiconductor nanowires

Mariya Neklyudova

In situ transmission electron microscopy (TEM) is a powerful tool for the field of material science which allows a direct observation of the dynamic response of a material to applied external conditions (electrical bias, heating, reactive environment interaction, etc.) in the real time. *In situ* TEM experiments provide new knowledge and deep understanding of physic-chemical mechanisms occurring in material at the nanoscale. Unique capabilities of *in situ* TEM experiments are the result of the recent advancements in the development of TEMs, microelectronics and TEM-holders developed for various external stimulus.

In this thesis we have performed experiments on *in situ* electrical measurements in order to investigate the behavior of InAs semiconductor nanowires under an influence of applied electric field and study an electromigration phenomenon in thin metallic Au-Pd and Au polycrystalline nanowires in order to produce nanogap electrodes with small nanogap sizes for possible applications in molecular electronics. Also, we have performed *in situ* heating experiments in TEM to study the behaviour of polycrystalline thin bismuth films with low thermal conductivity under *in situ* heating and electron-beam bombardment. Also, we have developed a clean room fabrication technique, called back side lithography technique. This technique allows to obtain smooth and uniform electron viewing transparent windows with a thickness of several nanometers at certain locations of a thick SiN membrane which is usually used in MEMS-based chips for *in situ* TEM experiments.

Samenvatting

In situ TEM elektrische metingen op metaal en halfgeleider nanodraden

Mariya Neklyudova

In situ transmissie elektronen microscopie (TEM) is een krachtig instrument voor materiaalkundig onderzoek, omdat het een directe observatie mogelijk maakt van de dynamische respons van een materiaal op aangebrachte externe condities (elektrische stimulus, verhitting, reactieve omgeving zoals gas, etc.) in real-time. *In situ* TEM experimenten leveren nieuwe kennis en dieper begrip van physisch-chemische mechanismen die op nanoschaal in materialen voorkomen. De unieke capaciteiten van *in situ* TEM experimenten zijn het gevolg van recente vooruitgangen in de ontwikkeling van TEMs, micro-elektronica en TEM-houders, ontworpen om diverse externe stimuli aan te brengen.

In dit proefschrift hebben we *in situ* elektrische metingen uitgevoerd, om het gedrag van InAs halfgeleider nanodraden onder invloed van een opgelegd elektrisch veld te onderzoeken, en om elektromigratie in dunne, metallische Au-Pd en Au polykristallijne nanodraden te bestuderen. Dit wordt gebruikt om nano-elektrodes op zeer kleine afstand te produceren, die mogelijke toepassingen hebben in moleculaire elektronica. Ook hebben we *in situ* verhittings-experimenten in de TEM uitgevoerd, om het gedrag van polykristallijne, dunne bismut laagjes met lage thermische geleiding te bestuderen, onder invloed van verhitting en de elektronenbundel. Daarnaast hebben we een cleanroom fabricatie techniek ontwikkeld, de zogenaamde 'back side lithography' techniek. Deze techniek maakt het mogelijk om gladde en uniforme, elektron-transparante ramen te verkrijgen, met een dikte van enkele nanometers, op enkele specifieke locaties in een dik SiN membraan, welke vaak gebruikt worden in MEMS-gebaseerde chips voor *in situ* TEM experimenten.

Curriculum vitae

16 Sep 1988	Born in Petropavlovsk-Kamchatsky, USSR
2005-2009	**Bachelor of Science** in Physics, Novosibirsk State University, Russia
2009-2011	**Master of Science** in Physics (Cum Laude), Novosibirsk State University Thesis: "TEM studies of crystalline structure peculiarities of $Cd_{1-x}Hg_xTe$ heterostructures grown by MBE on Si(310) and GaAs(301) " Promotor: Dr. ir. A. K. Gutakovsky
2012-2016	**Doctor of Philosophy** in Applied Physics, Kavli Institute of Nanoscience, Delft Technische Universiteit Delft, The Netherlands Thesis: "*In situ* TEM electrical measurements of semiconductor and metal nanowires" Promotor: Prof. dr. H. W. Zandbergen
2016- Present	**Postdoctoral Research Fellow**, Kavli Institute of Nanoscience, Delft Technische Universiteit Delft, The Netherlands Group of Prof. dr. H. W. Zandbergen

Publications

1. **M. Neklyudova**, C. Sabater, J. M. van Ruitenbeek, A. K. Erdamar, H. W. Zandbergen. *In situ TEM formation of a single-crystalline bismuth film on an amorphous substrate,* to be submitted.

2. **M. Neklyudova**, V. Migunov, R. E. Dunin-Borkowski, H. W. Zandbergen. *In situ TEM investigations of controlled electrical breakdowns in InAs nanowires,* to be submitted.

3. A. K. Erdamar, L. Vicarelli, **M. Neklyudova**, S. J. Heerema, G. Pandraud, C. Dekker and H.W. Zandbergen. *Back side lithography technique for transmission electron microscopy research*, to be submitted.

4. C. Zhang, **M. Neklyudova**, L. Fang, Q. Xu, H. Wang, F. D. Tichelaar, H. W. Zandbergen. *In situ electrical characterization of tapered InAs nanowires in a transmission electron microscope with ohmic contacts*. Nanotechnology, 2015, 26(15), 155703.

5. **M. Neklyudova**, B. J. Thijsse, H. W. Zandbergen. *In situ TEM visualization of electromigration-induced nanogap formation in AuPd nanowires,* to be submitted.

6. I. M. Dildar, **M. Neklyudova**, Q. Xu, H. W. Zandbergen, S. Harkema, D. Boltje, and J. Aarts. *Growing LaAlO3/SrTiO3 interfaces by sputter deposition.* AIP Asvances, 2015, 5, 067156.

Acknowledgements

This thesis is the result of my research work at the National Centre for High Resolution Electron Microscopy, Kavli Institute of Nanoscience, TU Delft. And the last but not least of this thesis, I would like to express my sincere gratitude to all the people who contributed and provided me support and help.

First of all, I heartily thank my supervisor, Prof. dr. Henny Zandbergen, for the great opportunity to do a PhD research in his group. Henny, thank you very much for the interesting research ideas you came up with during all this time, for the continuous motivation, inspiration and encouragement, for your time. I thank you very much for the discussions which we had and which contributed to my experience and knowledge. I am very impressed with your broad scientific knowledge and ability to solve "unsolvable" problems.

Special thanks to Dr. ir. Frans Tichelaar, highly skilled expert in TEM, for his significant help with the microscopes and the excellent ability to recognize any TEM problem with his highly professional "X-ray" eyes and bring the machines to an operating regime in a very short time.

I would like to thank Tom de Kruijff for all technical support he provides our group every day. Tom, you have "golden" hands – whatever you touch amazingly starts to work in the best way.

Sincere thanks to a wonderful person, wise woman, Marijke van der Veen, for the instant administrative support in any kind of questions and situations. Marijke, thank you so much for being very kind, responsive and helpful.

I am particularly thankful to Prof. dr. Jan van Ruitenbeek for his constant support, very useful and interesting discussions and questions. He never hesitated to spend extra time discussing details of the experiments and helping us with theoretical interpretations. His vision made this work possible

as well as enjoyable. I also thank him for serving on my dissertation committee.

Special thanks to Prof. dr. Barend Thijsse for productive discussions, interesting ideas and his instant willingness to help on possible interpretations of material transport at the nanoscale. I also thank him for serving on my dissertation committee.

I would like to thank Dr. Qiang Xu, very positive person and talented TEM scientist, who provided support and guidance when I came to HREM group. Qiang, thanks a lot for teaching some TEM and explaining how the things do work. I'm very thankful to you for motivating me when nothing did work.

My special thanks go to the people who are experts in the field of cleanroom sample fabrication for providing all the technical support and a very smooth fabrication flow of various chips for all PhD and PostDoc researchers in the cleanroom. I heartily thank Mark Zuiddam, Marco van der Krogt, Roel Mattern, Charles de Boer, Hozan Miro, Anja van Langen-Suurling, Arnold van Run and Ewan Hendriks.

I would like to thank HREM group: Dr. Jouk Jansen, IT expert, for his instant technical support with hardware and software; Ganesh, Hui and Marien for being very great officemates and friends; Anil, Sairam, Shiv, Leonardo, Tanya, Chao, Meng Yue, Chunhui, Chenggang and Yoones for being wonderful colleagues. I also thank my Leiden colleagues for interesting and useful discussions and collaborations: Carlos, Johannes, Thomas and Takahiro.

I am particularly thankful to my paranymphs, Ahmet and Masha, for being great friends, for being wonderful, positive, kind, honest, reliable, interesting and heartful people.

I sincerely thank my collaborators from Ernst Ruska-Centre for Microscopy and Spectroscopy with Electrons, Research Centre Julich, Dr. Vadim Migunov and Prof. Rafal Dunin-Borkowski, for their significant help with holography experiments, huge amount of holography data analysis and discussions.

Каждому человеку очень важно встретить настоящего учителя не только в жизни, но и в профессии. Мне очень посчастливилось встретить таких людей на своем пути. В первую очередь, я от всего сердца и души благодарю Антона Константиновича Гутаковского, моего первого Учителя в просвечивающей электронной микроскопии, неимоверно талантливого, умного, доброго, отзывчивого человека и потрясающего ученого. Спасибо Вам за то, что Вы появились в моей жизни! Без Вас я бы не стала тем, кто я есть. Я от всего своего сердца благодарю Людмилу Ивановну Федину, профессионала, эксперта в электронной микроскопии и восхитительную женщину, за веру в меня, за всестороннюю поддержку, за интересные беседы. Я очень рада, что мне повезло в этой жизни работать с Вами. Я искренне благодарна профессору и директору института физики полупроводников (ИФП СО РАН) Александру Васильевичу Латышеву, за уникальную возможность работать с высококлассными специалистами и просто отличными людьми, за теплую и дружественную атмосферу. Спасибо Вам за интересные, захватывающие семинары и лекции, за Вашу доброту и помощь. Я благодарна моим коллегам в ИФП СО РАН за то, что вы были моей второй семьей.

Огромное спасибо всем моим друзьям за хорошее настроение, за душевные разговоры, интересные беседы, за теплую атмосферу и поддержку☺ Женя, тебе огромное персональное спасибо за критический ум, за твое желание разобраться в любом вопросе или проблеме, выслушать и помочь советом.

Петя, спасибо за дружбу, тепло и любовь☺ Спасибо, что показал мне Альпы, за наши путешествия, беседы и за спасение со мною животных☺ Мне очень классно с тобой☺

Моя дорогая мамочка, мой самый драгоценный и светлый человечек на этом свете! Пожалуй, нет таких слов, чтобы выразить мою глубокую благодавность тебе за все, что ты сделала и делаешь в этой жизни для меня. Спасибо за твою безграничную поддержку, за твою бесконечную любовь, за все тепло, за наши беседы, у тебя самое доброе, мудрое и любящее сердце... Я постоянно благодарю Бога за то, что ты есть, за то, что ты – моя МАМА. Спасибо Тебе, что дала мне столько

возможностей, за то, что сделала жизнь интересной, увлекательной и доброй!!!

Mariya Neklyudova
Delft, July 2016